

**Static and dynamic magnetic properties of
soft/hard ferromagnetic and
ferromagnetic/antiferromagnetic bilayers.**

By
Sagarika Nayak

Enrolment No. PHYS11201404008

**National Institute of Science Education and Research,
Bhubaneswar**

A thesis submitted to the

Board of Studies in Physical Sciences

In partial fulfillment of requirements

for the Degree of

DOCTOR OF PHILOSOPHY

of

HOMI BHABHA NATIONAL INSTITUTE



February, 2020

STATEMENT BY AUTHOR

This dissertation has been submitted in partial fulfillment of requirements for an advanced degree at Homi Bhabha National Institute (HBNI) and is deposited in the Library to be made available to borrowers under rules of the HBNI.

Brief quotations from this dissertation are allowable without special permission, provided that accurate acknowledgement of source is made. Requests for permission for extended quotation from or reproduction of this manuscript in whole or in part may be granted by the Competent Authority of HBNI when in his or her judgment the proposed use of the material is in the interests of scholarship. In all other instances, however, permission must be obtained from the author.

Sagarika Nayak
(Sagarika Nayak)

DECLARATION

I, hereby declare that the investigation presented in the thesis has been carried out by me. The work is original and has not been submitted earlier as a whole or in part for a degree / diploma at this or any other Institution / University.

Sagarika Nayak
(Sagarika Nayak)

List of Publications arising from the thesis

Journal

1. Nayak S., Mallick S., Singh B. B., and Bedanta S. Effect of sputtered flux direction on damping properties in magnetic bilayers, *J. Phys. D: Appl. Phys.* **51**, 055008 (2018).
2. Nayak S., Singh B. B., Mallick S., and Bedanta S. Tuning of magnetic properties by alternating the order of hard/soft bilayers with various thicknesses, *J. Phys. D: Appl. Phys.* **52**, 305301 (2019).
3. Nayak S., Manna P. K., V. Thiruvengadam, Singh B. B., Chelvane J. A., and Bedanta S. Exchange bias in Fe/ Ir₂₀Mn₈₀ bilayers: Role of spin-glass like interface and bulk' antiferromagnet spins, *J. Magn. Magn. Mater.* **499**, 166267 (2020).

Manuscript under review

1. S. Nayak, S. S. Das, B. B. Singh, T. Charlton, C. Kinane and S. Bedanta, Study of magnetic interface and its effect in Fe/NiFe bilayers of alternating order, RSC Advances.

Manuscript in preparation

1. Nayak S., Singh B. B., Mohanty S. and Bedanta S. Effect of interfacial exchange coupling on static and dynamic magnetic properties.
2. Nayak S., Manna P. K. and Bedanta S. Exchange bias in Ni₅₀Mn₅₀/Co₄₀Fe₄₀B₂₀ system.

Sagarika Nayak
(Sagarika Nayak)

Dedicated to my mother

ACKNOWLEDGEMENTS

At first, I would like to express my sincere gratitude to my supervisor Dr. Subhankar Bedanta for his continuous support and valuable advice during my Ph.D tenure. I am also thankful to him for his guidance. He helped me a lot for improving my leading capability and to be trained properly. His suggestions for expressing the concept of Physics made my fundamentals stronger and patience during paper discussion was amazing. The work efforts from him made me learn a lot of thing. I could not have finished my thesis work without his support and guidance.

I am also obliged to the chairman of my doctoral committee Prof. Bedangadas Mohanty for the sincere evaluation of my annual evaluation talks and valuable advices. I am also grateful to the members of my doctoral committee Dr. Anamitra Mukherjee and Dr. Kartikeswar Senapati for their suggestions during the annual evaluation talks.

I am thankful to Dr. Braj Bhusan Singh, INSPIRE Faculty, NISER for training me at different instruments and his suggestions for my Ph.D. work. I am very much blessed because to be surrounded by my seniors Dr. Niru Chowdhury, Dr. Sougata Mallick and Dr. Srijani Mallik. They helped me a lot in instrument training and I enjoyed having discussions with them. I am also thankful to Mr. Sukanta Kumar Jena, Dr. Sudhansu Sekhar Das, Dr. V Thiruvengadam , Dr. Palash Kumar Manna, Dr. Minaxi Sharma for giving me advices and spending time for my work. I thank my juniors Purbasha, Puspendra, Esita, Brindaban, Koustuv, Shaktiranjan, Abhishek and Azharudheen for spending their valuable time with me during discussion.

I acknowledge NISER and department of atomic energy (DAE) for funding my scholarship and infrastructure support of our laboratory. I also acknowledge DST SERB, DST nanomission for financial support for establishing some of the experimental facilities in our laboratory.

(Sagarika Nayak)

Chapter 8: Summary and outlook:

The motivation in this thesis was to study the static and dynamic magnetic properties of ferromagnetic hard/soft and ferromagnetic/antiferromagnetic bilayers. Various fabrication methodologies have been utilized to tune the magnetic properties of hard/soft ferromagnetic layers. The exchange coupling at the interface of ferromagnetic layers has the important role tuning the magnetic properties. In the later part of this study of exchange bias in FM/AFM bilayers, we found that disorder and frustration plays a very important role in tuning the magnetic properties.

The dc magnetron sputtering method is used to fabricate Co (soft), CoFeB (hard) ferromagnetic single layers and Co/CoFeB bilayers. MOKE based microscopy, and FMR spectroscopy are the mostly used characterization techniques to study the soft and hard ferromagnetic bilayers. The magnetic bilayers are deposited in parallel (\parallel) and perpendicular (\perp) configuration. The Co/CoFeB bilayers have the magnetic domains which is the combined effect of single layers due to the exchange coupling between them. The H_C of the magnetic bilayers is higher than single Co layer whereas lesser than single CoFeB layer. Thus, the magnetic hardness of CoFeB is responsible for the enhancement of coercivity in the magnetic bilayers. The tuning of coercivity is achieved by using different deposition methodologies such as \parallel and \perp configuration. It is also found that α of the magnetic bilayer is higher than the single layers. Thus, the exchange coupling between the magnetic layers and the high magnetic anisotropy of hard magnetic layer are responsible for the enhancement of damping constant α . Magnetic bilayer deposited in \parallel configuration has lower value of α than the magnetic bilayer deposited in \perp configuration due to its higher interface roughness.

Co/CoFeB magnetic bilayers are fabricated with various thicknesses and alternate the order of magnetic layers to investigate the static and dynamic magnetic properties. The magnetic anisotropy energy (K_U) is relatively high for the magnetic bilayers with higher thickness of

Co. The interfacial exchange coupling is responsible for the tuning of the magnetic anisotropy energy (K_U). The saturation magnetization (M_S) is also higher by increasing the thickness of soft Co magnetic layer. It is found that the magnetic domains type and size have been modified by increasing the thickness of Co and also in the magnetic bilayers where CoFeB is at the bottom. Different values of coercivity are found by using this deposition methodologies. Due to the increase in interfacial exchange coupling, the coercivity is higher in magnetic bilayer with larger thickness of Co and for the bilayer in which CoFeB is at the bottom. Uniaxial anisotropy is found in some samples and combination of uniaxial and six-fold anisotropies in some samples due to the oblique angle of deposition in our sputtering system. The increased interfacial exchange coupling is also responsible for the enhancement in the value of damping constant. The correlation between the inhomogeneous linewidth broadening ΔH_0 and damping constant α is also found. Perpendicular surface anisotropy constant K_S values have been calculated using the magnetization values obtained from SQUID and FMR for all the samples and different values of K_S have been found for all the samples.

The static and dynamic magnetic properties of Co, CoFeB single magnetic layers and bilayers have been studied which are deposited without seed layer, at 20 rpm speed of substrate and in different deposition pressures. With these above deposition conditions, it is found that Co is relatively harder than CoFeB layer due to change in microstructure. Labyrinth and ripple types of magnetic domains have been found in the bilayers due to the interfacial exchange coupling between the single layers. The magnetic bilayers have H_C , M_S and K_U values higher than CoFeB but lesser than Co single layer due to exchange coupling between them and magnetic hardness of Co is also responsible for the enhancement of H_C in the bilayers. Decrease in M_S has been found with increase in deposition pressure. The increase in deposition pressure results inner (compressive or tensile) stress in the magnetic thin films that tunes the magnetic dynamic properties. The tuning of α , H_{Keff} , g-factor and $4\pi M_{eff}$ values is found with the deposition

pressure. The tuning of α , $H_{K\text{eff}}$ and $4\pi M_{\text{eff}}$ values is also found by direct exchange coupling between the magnetic Co and CoFeB single layers. Thus, we found that the interfacial exchange coupling and deposition pressure have the effect on static and dynamic magnetic properties.

The soft (NiFe) and hard (Fe) magnetic bilayers are also fabricated by dc magnetron sputtering method. The Kerr magnetometry revealed the large change of coercivity and H_K values by alternating the order of magnetic layers. Smaller magnetic domains away from easy axis is found in the bilayer with higher uniaxial magnetic anisotropy. FMR angle dependent measurement revealed the presence of uniaxial magnetic anisotropy in all the samples. It has been previously reported that high exchange coupling leads to an increase in damping constant α but in the present study of these Fe/NiFe samples, the damping constant α is similar to the single layers. From PNR measurement, the high value of inter-diffusion layer thickness and magnetic moment are found at the Fe-NiFe interface of the magnetic bilayer with high value of H_C . The high exchange coupling between the magnetic layers might be a reason for the enhancement of coercivity and anisotropy field H_K .

In the last two chapters, the static and dynamic magnetic properties of FM/AFM bilayers were studied. The exchange coupling between the FM and AFM develops unidirectional anisotropy at the interface which gives exchange bias effect. Temperature and cooling field dependence of exchange bias have been performed to investigate the magnetic nature of the interface. The exponential decay of H_{EB} and H_C with temperature indicates the presence of spin glass state at the interface. Sharp rise of H_{EB} is found below 50 K in the temperature dependent study due to contribution of frozen spin glass. Further, H_{EB} decreases with the increase in cooling field similar to a FM/SG system. The training effect data are fitted using spin configurational relaxation model and frozen and rotatable spin relaxation model to confirm the presence of spin glass like interface. The variation of exchange bias field is found to increase in IrMn

thickness indicating the contribution of ‘bulk’ part of AFM to exchange bias.

Exchange bias in NiMn/CoFeB systems have also been studied. In these systems, Ta/Pt is deposited as buffer layer to induce AFM order without doing post deposition annealing. The sign change of exchange bias is observed, in some of the bilayers, near to the compensation temperature T_0 due to the indirect exchange coupling between the ‘bulk’ NiMn and interface spins. The exponential decay of coercivity is found in all the samples. The decrease of exchange bias field H_{EB} is found with increase in cooling field H_{FC} whereas coercivity remains constant which is generally observed in FM/SG system. The training effect data have been fitted with spin configurational relaxation model and frozen and rotatable spin relaxation model confirming the presence of spin glass like interface. For further confirmation of the presence of spin glass phase, ac susceptibility measurements have been performed. The peak temperature T_f (obtained from ac susceptibility measurements) vs frequency f data are fitted using Neel-Arrhenius (N-A) model and Vogel-Fulcher (V-F) law to know if the system is non-interacting like superparamagnets or interacting like spin glass system.

One can also study the magnetic properties of the discussed soft/hard bilayers by placing very thin Cu layer of various thicknesses at the interface such that the interfacial exchange coupling gets modified. One can do post deposition annealing at various temperatures in the Co/CoFeB bilayers to tune the interfacial exchange coupling and hence the energy product $(BH)_{max}$ value. Also, one can systematically increase the thickness of soft and hard magnetic layers in the above soft/hard bilayers to investigate the effect of it on the magnetic properties. It would be interesting to systematically increase the deposition pressure from ultra-low pressure to high pressure to study the effect on static and dynamic properties.

In this thesis work, the Fe/IrMn samples are prepared with 0 rpm rotation speed of substrate which gives growth induced uniaxial magnetic anisotropy in all the bilayers. One can compare the exchange bias results obtained using 0 and 20 rpm speed of the substrate. Also, one can

insert an interface layer such as Cu of different thicknesses in between the FM and AFM layers to study the effect of the modification of interfacial exchange coupling on the EB.

Understanding of these aspects will have significant impact for future spintronic based application.

CONTENTS

STATEMENT BY AUTHOR	iii
DECLARATION.....	iv
List of Publications.....	v
DEDICATIONS.....	vi
ACKNOWLEDGEMENTS.....	vii
SUMMARY.....	ix
CONTENTS.....	xi
LIST OF FIGURES.....	xvi
LIST OF TABLES.....	xxv
List of Abbreviations.....	xxvii
Chapter 1: Introduction and fundamentals.....	1
1.1 Introduction.....	1
1.2 Fundamentals.....	5
1.2.1 Exchange energy.....	5
1.2.2 Anisotropy energy.....	7
1.2.3 Exchange anisotropy.....	10
1.2.4 Surface anisotropy.....	10
1.2.5 Shape anisotropy.....	11
1.2.6 Magnetostatic Energy.....	13
1.2.7 Magnetoelastic energy.....	14
1.3 Weiss Domain theory.....	15
1.4 Magnetic hysteresis.....	18
1.4.1 Domain Wall Motion.....	19

1.4.2	Magnetization reversal by rotation (Stoner-Wohlfarth Model).....	20
1.5	Soft and hard magnetic materials.....	22
1.6	Hard/soft magnetic bilayers.....	24
1.7	Introduction to exchange bias.....	26
1.7.1	Discovery of the exchange bias effect.....	26
1.7.2	Ideal model of exchange bias: Phenomenology.....	28
1.7.3	Meiklejohn-Bean model: Quantitative analysis.....	29
1.7.4	Modified Meiklejohn-Bean model.....	31
1.7.5	Domain state model.....	33
1.7.6	Spin-Glass model.....	35
	Chapter 2: Experimental details.....	38
2.1	Thin film deposition techniques.....	38
2.1.1	E-beam evaporation.....	38
2.1.2	Sputtering.....	38
2.1.2.1	Magnetron sputtering.....	39
2.1.2.2	Unbalanced magnetron sputtering.....	40
2.1.2.3	DC and RF sputtering.....	41
2.1.3	Multi-deposition system at NISER	41
2.2	X-ray diffraction and grazing incidence x-ray diffraction (GIXRD).....	44
2.3	X-ray reflectivity (XRR).....	46
2.4	Ferromagnetic resonance (FMR) setup.....	49
2.5	Superconducting quantum interference device (SQUID) Magnetometer.....	53
2.6	Magneto optic Kerr effect (MOKE) related phenomena.....	56
2.6.1	Theory of magneto-optic phenomena.....	56

2.6.2 Magneto-Optic Kerr effect	58
2.6.3 Kerr microscopy.....	61
2.6.4 Polarized neutron reflectivity (PNR).....	63
Chapter 3: Section 3.1: Effect of sputtered flux direction of Co and CoFeB on magnetization reversal and damping properties in Co/CoFeB bilayers.....	69
3.1.1 Introduction.....	70
3.1.2 Experimental details.....	70
3.1.3 Magnetization reversal and magnetic domains.....	72
3.1.4 Damping properties.....	75
3.1.5 Anisotropy energy.....	79
3.1.6 Conclusions.....	79
Section 3.2: Effect of order and thickness of Co and CoFeB layers on magnetic anisotropy and damping properties in Co/CoFeB bilayers.....	80
3.2.1 Introduction.....	80
3.2.2 Experimental details.....	81
3.2.3 Magnetization reversal, anisotropy, and domain imaging study.....	81
3.2.4 Damping properties study.....	85
3.2.5 Conclusions.....	88
Chapter 4: Effect of interfacial exchange coupling on static and dynamic magnetic properties	89
4.1 Introduction.....	89
4.2 Experimental details.....	91
4.3 Magnetization reversal, domain imaging and anisotropy.....	92
4.4 Damping properties study.....	97

4.5 Conclusions.....	101
Chapter 5: Effect of interfaces on magnetic properties in Fe/NiFe bilayers of alternating order.....	102
5.1 Introduction.....	102
5.2 Experimental details.....	103
5.3 Structural properties.....	105
5.4 Hysteresis loops and domain images.....	106
5.5 Dynamic magnetic properties.....	108
5.6 Polarized neutron reflectivity (PNR) study.....	112
5.7 Conclusions.....	115
Chapter 6: A study of exchange bias and spin glass behaviour in Fe/IrMn system.....	116
6.1 Introduction.....	116
6.2 Experimental details.....	118
6.3 Structural characterization.....	118
6.4 Magnetic characterization: Temperature and cooling field dependence study.....	119
6.5 Magnetic characterization: Training effect.....	121
6.6 Conclusions.....	124
Chapter 7: Exchange bias in NiMn/Co₄₀Fe₄₀B₂₀ system.....	126
7.1 Introduction.....	126
7.2 Experimental details.....	127
7.3 Study of static magnetic properties.....	128
7.4 Training effect.....	131

7.5 Study of dynamic magnetic properties.....	134
7.6 Conclusions.....	137
Chapter 8: Summary and outlook.....	139
References.....	144

SUMMARY

Soft/hard magnetic bilayers provide high energy product $(BH)_{\max}$ value compared to its constituent layers which have the application in permanent magnets, thermally assisted magnetic recording etc. Various methodology has been utilized to tune the $(BH)_{\max}$ value. Similarly, research has been going on to find materials with lower Gilbert damping constant α value due to its application in spin transfer torque-based memory and having less critical switching current density etc. Deposition of magnetic Co/CoFeB bilayers have been performed in different preparation configuration, and deposition pressure to tune the magnetic properties. Uniaxial magnetic anisotropy is found in all the samples irrespective of the preparation configuration due to oblique angle of deposition. Due to direct exchange coupling between the magnetic layers, high value of α is found. Similarly, Co/CoFeB bilayers have been studied by alternating the order of these layers with different thicknesses. CoFeB/Co magnetic bilayers and the reference single layers deposited without seed layer where the substrate is rotated at 20 rpm speed during fabrication have also been studied. Further, Fe/NiFe bilayers have been studied by alternating the order of magnetic layers in order to tune the static and dynamic magnetic properties. In these systems, our interest is to tune the magnetic properties such as domain structure, coercivity, saturation magnetization (M_s) and α value etc.

In the second half of my thesis, the study on exchange bias in Ferromagnetic (FM)/antiferromagnetic (AFM) bilayers has been performed. In recent years FM/AFM systems have been studied widely due to its technological application in spintronic based devices such as spin valves, magnetic random-access memories (MRAMs), ultrahigh-density magnetic recording, giant magnetoresistance (GMR) etc. The

interface of the ferromagnet (FM)/antiferromagnet (AFM) system can be spin glass like due to interface roughness, structural disorder, chemical intermixing etc. Two types of exchange bias systems IrMn/Fe, and NiMn/CoFeB bilayers have been studied in this thesis. In this study, the presence of spin glass like interface and also the spin glass phase are found from the temperature T , cooling field H_{FC} dependence of exchange bias and training effect. The training effect data have been fitted well using frozen and rotatable spin relaxation model and spin configurational relaxation model. It has been reported that although the interface plays the major role, however, the 'bulk' AFM spins also have an important role in exchange bias. From this study, the 'bulk' AFM spins contribution to exchange bias is confirmed from the variation of exchange bias field with the thickness of AFM layer. . AC susceptibility measurements have been performed in NiMn/CoFeB exchange bias systems. In NiMn/CoFeB system, spin glass nature of NiMn is found from ac susceptibility measurements. Fitting of the peak temperature T_f (obtained from ac susceptibility measurements) vs frequency data using Vogel-Fulcher (V-F) law is performed to confirm the presence of spin glass phase.

Chapter 2: Experimental Techniques

In this chapter, various experimental techniques for structural and magnetic characterizations are described along with the techniques for sample preparation. The ferromagnetic, antiferromagnetic, seed and capping layers such as Cu, Ta and Pt are deposited using dc magnetron sputtering whereas Au as capping layer has been deposited by using e-beam evaporation methods. The magnetic characterizations have been performed using Magneto-Optic Kerr effect (MOKE) based magnetometry and microscopy, ferromagnetic resonance (FMR), superconducting quantum interference device (SQUID) magnetometry and polarized neutron reflectivity (PNR) methods. The structural characterizations have been performed using grazing incidence X-ray diffraction (GIXRD) and X-ray reflectivity (XRR) techniques.

2.1 Thin film deposition techniques:

Thin film deposition, performed in vacuum, can be called physical vapour deposition method. Among them (i) thermal evaporation is a method where, by heating the target, the vapour pressure is larger than the ambient pressure, (ii) ionic sputtering is a method where atoms are ejected from the target by hitting the target with the ions³⁹. Different types of ionic sputtering are diode, ion beam and magnetron sputtering³⁹.

In thermal evaporation technique, different methods can be used to heat the target material. Resistance heating technique and electron beam heating technique are the methods⁴⁰. We will describe the e-beam evaporation method in the following.

2.1.1 E-beam evaporation: In this process, emitted electrons from the filament hit on the target material. As a result of the bombardment, heat is generated in the target material and change of phase occurs to gaseous. So, the desired materials evaporates and then condense on the wafer⁴¹.

2.1.2 Sputtering:

In sputtering, atoms or molecules are emitted from the target by high energy positive charge particles. By applying negative potential to the target, electrons are emitted from the target and reacts with Ar gas to produce Ar^+ ions. In this technique, momentum transfer takes place between the high-powered atomic size particles and the atoms of the target. Elastic and inelastic collision occurs during momentum transfer. Ions of target and the gas are generated in elastic collision. Secondary electrons, UV/visible photons, X-ray and implanted particles are produced in inelastic collision. Deposition by sputtering is a vacuum process. Pressure should be low in this process because (1) for maintenance of high ion energies (2) for less collisions between atom and gas³⁹. Collision between the atom and gas is depended on the mean free path (MFP) in the gas. Change in the MFP occurs with pressure in the gas. 1 Pascal or better pressure should be required for maintaining less collision of atom and gas. In the sputtering system most of the applied voltage appears across the cathode dark space. Cathode dark space is the region where the electrons have too much energy⁴². For the reduction of dark space effect, the anode and target should be closer³⁹. If not then the plasma extinguishes. The dark space grows as the pressure is lowered in the presence of glow discharge. Due to increase in MFP the dark space increases and production of ions takes place away from the target which disappears in the chamber wall³⁹. Also, the electrons arrive at the anode without formation of ions. Therefore, one usually finds low ionization efficiency.

2.1.2.1 Magnetron sputtering:

The limitation of sputtering are low deposition rates, low ionization efficiency and high substrate heating efficiency. To overcome this, magnetron sputtering and unbalanced magnetron sputtering have been developed⁴³.

Magnetic field parallel to the target surface is generated by the magnetrons. The magnetrons are arranged in the form of a ring by placing one pole at the central axis of the target and other two poles at the outer ends of the target⁴³. Magnetron results dense ion plasma near the target

by its increased ionization efficiency. As a result, deposition rate is high due to incidence of more ion on the target surface. Discharge is maintained at lower operating pressure and operating voltages compared to the general sputtering due to its increased ionization efficiency⁴³.

2.1.2.2 Unbalanced magnetron sputtering:

In unbalanced magnetron sputtering system, the outer poles have higher strength than the central pole. For this, the flux lines are headed towards the substrate without closing flux lines from the central pole to outer poles⁴³. Some secondary electrons also accompany this path creating the ion current. Thus, without biasing the substrate one can get high ion current. One order of greater magnitude of ion current can be generated in unbalanced magnetron sputtering than the conventional sputtering. In addition to high flux of coating, the unbalanced magnetron provides high ion current source⁴³. Ion current going to the target is directly dependent to the target current. Deposition rate depends on the target current directly. The above description is

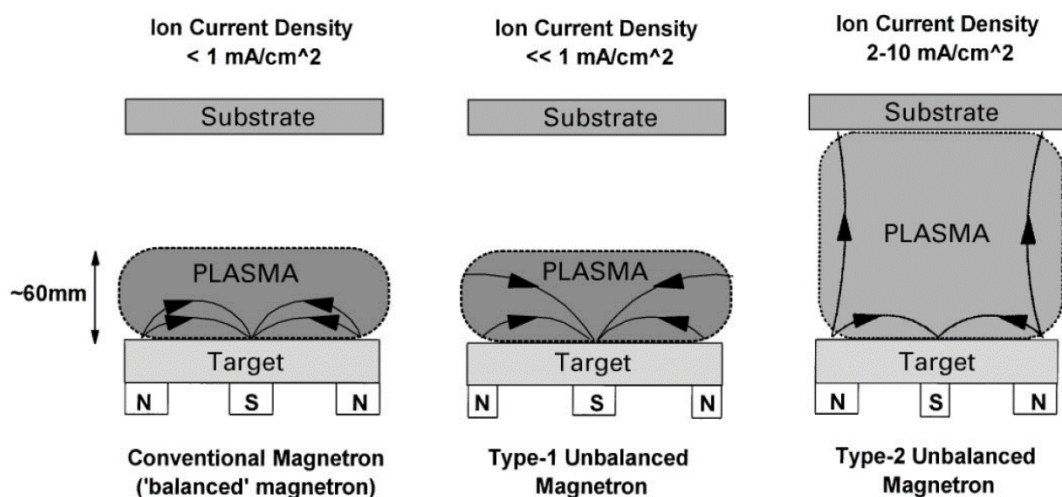


Figure 2.1:

Schematic of plasma formation region along with ion current density magnitude in conventional, type 1, and type 2 unbalanced magnetron sputtering. This figure is taken from the reference 43.

for type 2 unbalanced magnetron sputtering. However, in type 1 unbalanced magnetron

sputtering the strength of the central pole is high in comparison to the outer poles. In this case, lower plasma density exists near to the target and the flux lines move to the chamber wall instead of going to the target⁴³.

Figure 2.1 shows the region of plasma formation between the substrate and target. The region is very less in conventional and type 1 unbalanced magnetron sputtering system whereas the region extends to the substrate from the target in case of type 2 unbalanced magnetron sputtering system. Type 2 unbalanced magnetron is used in the MANTIS deposition system (of our lab).

2.1.2.3 DC and RF sputtering:

The various types of sputtering are (i) DC (diode or triode) sputtering (ii) AC (radiofrequency) sputtering which work on different systems namely magnetron dc (balanced or unbalanced), magnetron ac (balanced or unbalanced)⁴⁴ etc.

DC sputtering: In dc sputtering, conductive target material should be used because surface charge will be developed in insulating materials that stops ion bombardment on the target surface. Uniform plasma formation over large area is the advantage dc sputtering⁴⁴. One of the disadvantage of this sputtering is that the plasma confines near to the target and is not available close to the reactive gases for reactive sputtering⁴⁴. Unbalanced magnetron sputtering removes this difficulty.

RF sputtering: An alternating potential will be developed on the target surface when a rf potential with large peak to peak voltage is inductively coupled to target⁴⁴. During positive half cycle, acceleration of ions towards the target surface takes place to sputter the target material. During negative half cycle of the potential, acceleration of ions towards the target surface takes place to remove the charge build up.

2.1.3 Multi-deposition system at NISER:

We have a multi-deposition ultra-high vacuum (UHV) sputtering system in our lab manufactured by Mantis deposition Ltd., UK⁴⁵ which is shown in figure 2.3. UHV pressure of 5×10^{-10} mbar can be reached in the main chamber of the sputtering system using two turbo molecular pumps (TMP) and a backing pump. One TMP is directly connected to the main chamber through the throttle valve and another TMP is connected in nanogen. By using the load lock, the sample can be placed in the main chamber without breaking its vacuum as it is separated from load lock by a gate valve. We have the following methods for thin film deposition namely;

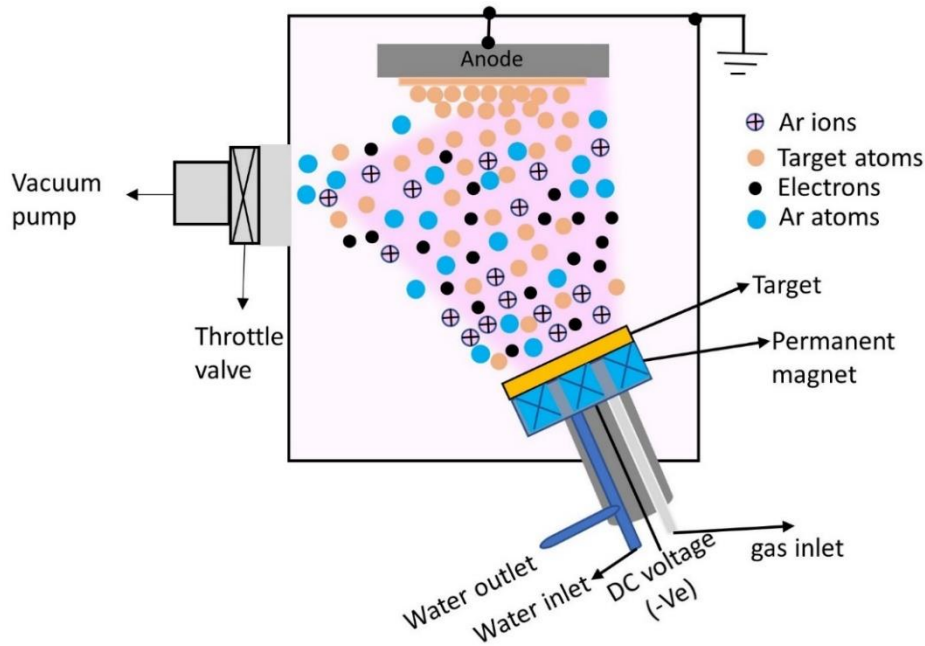


Figure 2.2: Schematic of dc magnetron sputtering system with various components. The light purple colour cone represents the plasma present in the system.

1. 3 dc sputtering sources
2. 2 rf sputtering sources
3. One e-beam evaporation source with 4 crucibles to place the deposition material in the form of rod, pallet and powder.

4. One thermal evaporator with two boats.
5. One nanogen to deposit nano-particles.
6. One MAT60 for doing reactive sputtering.

Figure 2.2 shows the schematic of the magnetron sputtering system with various parts such as vacuum pump assembly with throttle valve, the chiller cooling lines, the gas inlet, the power supply and the substrate table.

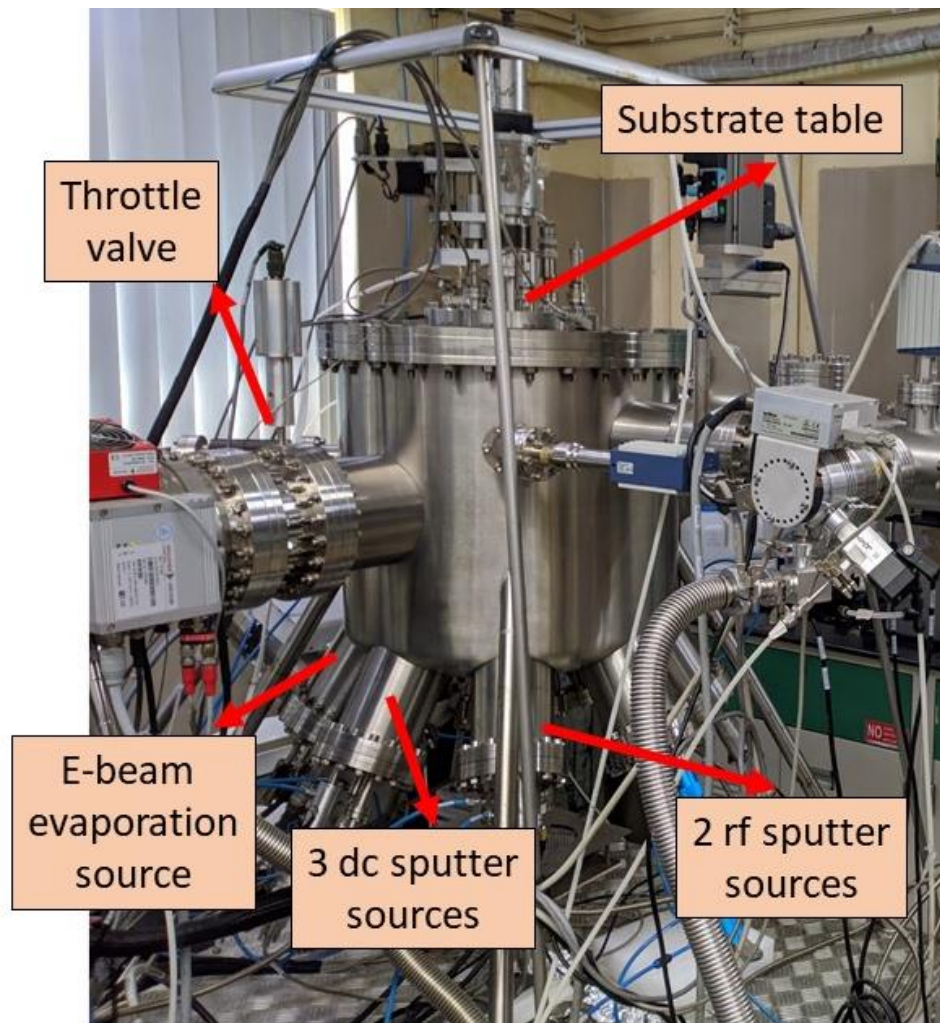


Figure 2.3: The image of the UHV multi-deposition system at NISER manufactured by Mantis deposition Ltd. UK.

To cool the sputtering source and turbo pump, closed cycle chiller liquid is used. The substrate table is at the top of the sputtering system. Using halogen lamps, heating of the substrate upto

800 °C is possible. Rotation of the substrate table upto 20 rotation per minute (rpm) during deposition is possible. Pressure gauges are connected to the main chamber and load lock to view the pressure inside the system. Using quartz crystal monitor (QCM), the thickness of thin film deposited is monitored. To produce Ar plasma, Ar gas in sccm is supplied through the mass flow controller (MFC). The shutter of all the cusps are closed except the shutter of the cusp which is used for deposition for avoiding contamination in all the other targets. The sputtering sources are at an angle of 45° wrt each other and at an angle of 30° wrt to substrate normal. Growth induce magnetic anisotropy is found in the studied samples due to this oblique angle of deposition. Therefore, uniaxial magnetic anisotropy is found in all our magnetic samples.

2.2. X-ray diffraction (XRD) and grazing incidence X-ray diffraction (GIXRD):

X-rays are electromagnetic waves with wavelength ranging from 0.02 Å to 100 Å. In comparison to visible light, the wavelength of X-rays is less, therefore, the energy and penetration depth is more for X-rays. The amount that X-rays penetrate depends on the material density. Therefore, X-ray gives the structural information of the matter. At one end of the evacuated X-ray tube, tungsten filament is the cathode and anode is at another end. Electrons are ejected by applying electric current to the filament. Acceleration of electrons towards the anode takes place due to large potential difference between the anode and cathode. Electron emits when kinetic energy of the accelerated electron is more than the binding energy of the target atom. If the innermost K-shell electron is emitted, then L or M shell electron will move to fill the K-shell. During this transition, an electromagnetic ray is emitted called X-ray. The emission of X-ray during the electron transition from L shell to K shell is called K_{α} X-ray and during the electron transition from M shell to K shell, it is called K_{β} X-ray. Hence, the generator of X-ray is characteristic here instead of continuous.

Crystal structure information is obtained from X-rays. X-ray diffracted differently for distinct structure and orientation of the crystal.

The Bragg's equation provides the resolution of an X-ray diffraction through detector which is given by;

$$2d_{hkl} \sin \theta_{hkl} = n\lambda \quad \dots\dots\dots (2.1)$$

Where, d is the atomic plane spacing, θ is the diffraction angle and λ is the wavelength of the X-ray.

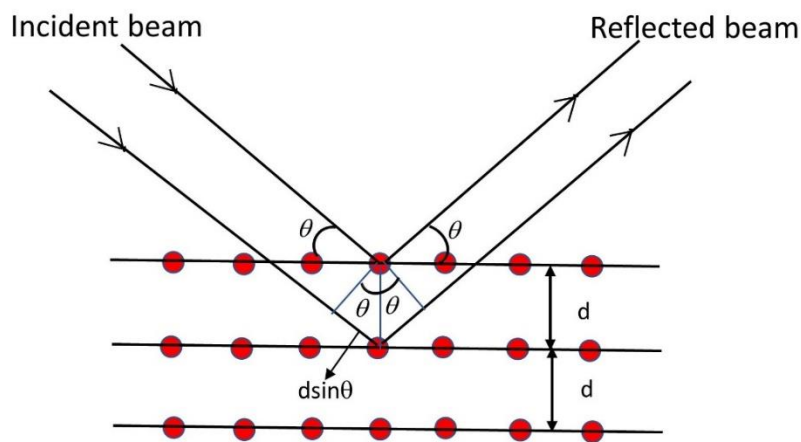


Figure 2.4: Schematic of X-ray diffraction where incident X-ray beam gets diffracted from the atomic planes with constructive interference to give the reflected beam.

Figure 2.4 shows the diffraction of the X-ray beam from the atomic planes separated by distance of d and the reflected X-ray beams follow the Bragg's law of diffraction with the path difference between incident and reflected beam is $2d \sin \theta$.

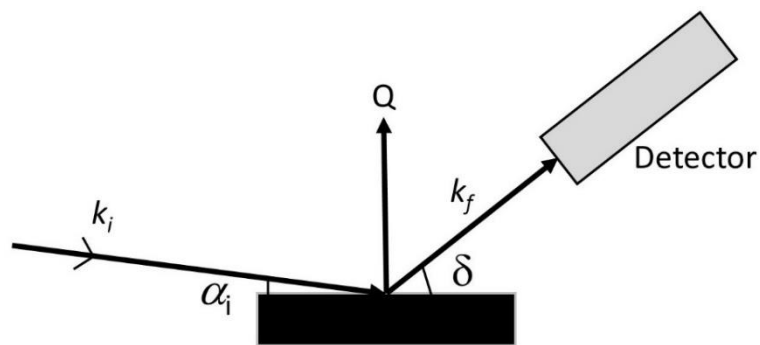


Figure 2.5: Schematic of the geometry of the Grazing incidence X-ray diffraction (GIXRD)

with the detector.

Figure 2.5 shows the geometry of diffraction of GIXRD where the incident angle is less than a degree and the detector move in large angles.

General θ - 2θ Bragg-Brentano geometry is used for characterization of powder samples where the angle of incidence is equal to the angle of diffraction⁴⁶. The diffracted beam from crystallographic plane of the sample will be incident on the detector. In this conventional geometry, the penetration depth of X-ray to the sample surface is several micrometres whereas this penetration depth is too large in case of thin film samples⁴⁶. In case of thin film, as the thickness of the substrate is large therefore the X-ray diffraction intensity is dominated by the substrate and can be abandoned from the thin film in comparison to the substrate in θ - 2θ Bragg-Brentano geometry. To probe the sample surface and minimize the substrate contribution, GIXRD is generally performed⁴⁶. In this asymmetrical geometry, to probe small depths in the thin film sample the incident angle can be varied.

X-ray diffractometer offers to provide crystallographic information of powder and thin film samples. The diffraction for powder samples is done in θ - 2θ geometry. The diffraction for thin film samples can be done both in θ - 2θ geometry (XRD) and 2θ geometry with the angle of incidence for our samples is 1° (GIXRD). Solid state detector is used for first scan. The source of X-ray is Cu-K α radiation. XRD and GIXRD measurements are performed using the X-ray diffractometer from Rigaku.

2.3 X-ray reflectivity (XRR):

X-ray reflectivity (XRR) is a very useful technique to probe the rough surface and interface properties of the material such as multilayer thin film⁴⁷⁻⁵⁴. Information about the sample roughness, thickness and density can be found by this technique as it finds the electron density perpendicular to the sample surface. It is a non-destructive method and obtains information

both for crystalline and amorphous materials⁵⁵. This method can detect the thin film samples for thickness ranging from 0.1 nm to 1000 nm, density < 1-2 % or higher and roughness of the surfaces, interfaces for thickness < 3-5 nm or higher⁵⁶. The intensity of the reflected X-ray beam can be observed close to the critical angle where total internal reflection occurs⁵⁵. The intensity of the specular reflected beam decreases above the critical angle. In the X-ray reflectivity pattern, one can find both Fresnel reflectivity in the form of $1/q^4$ dependence⁵⁷ and Kiessig fringes⁵⁵ coming from the interfaces of the multilayer thin film samples.

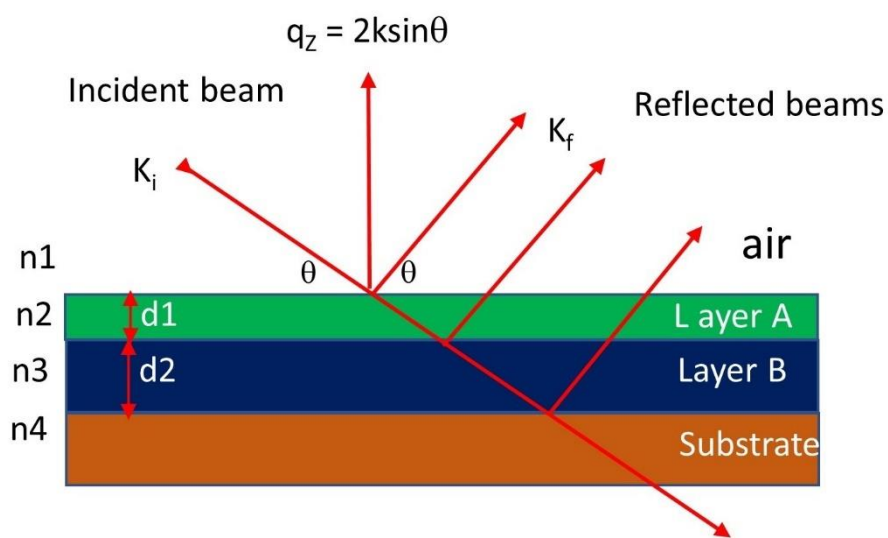


Figure 2.6: The incident beam of wave vector K_i incident on two layers of different refractive indices from vacuum with incident angle θ which is reflected at the same angle with wave vector K_f . X-ray reflectivity results from the interference of the reflected waves from different interfaces.

Figure 2.6 shows the schematic of scattering geometry of the XRR in a two layer system. The information about the interfaces (perpendicular to the sample surface) is obtained from the perpendicular scattering vector q_z . The reflectivity pattern is found by the interference of the reflected wave from different interfaces⁵⁸.

The momentum transfer in elastic scattering is given by⁵⁸

$$q_z = k_f - k_i = \frac{2\pi}{\lambda} (\sin \theta_f - \sin \theta_i) \dots\dots\dots(2.2)$$

For specular reflectivity, $\theta_f = \theta_i$, therefore⁵⁸ $q_z = \frac{4\pi}{\lambda} \sin \theta_i$

The refractive index can be expressed as⁵⁸

$$n = 1 - \delta - i\beta \dots\dots\dots(2.3)$$

The real part gives the dispersion and can be expressed as⁵⁸

$$\delta = \frac{\lambda^2}{2\pi} \rho b$$

where, ρb is the scattering length density. ρ is the coherent scattering length and b is the number density.

The imaginary part gives the adsorption and is given by⁵⁸,

$$\beta = \frac{\mu}{2k}$$

where, μ is the linear absorption coefficient.

The reflectivity from a homogeneous slab where the two interfaces are separated by a slab of thickness d is given by⁵⁸;

$$R(q) = R_F(q) \left| \int \rho(z) e^{2iq_1 z} dz \right|^2 \dots\dots\dots(2.4)$$

Where, $R_F(q)$ is Fresnel reflectivity intensity and scattering length density along z is defined as $\rho(z)$.

In case of specular reflection from multilayers, the reflectivity is obtained from the below relation⁵⁸

$$r_{j,j+1} = \frac{r_{j,j+1} + r_{j+1} e^{2iq_{j+1}d_j}}{1 + r_{j,j+1} r_{j+1} e^{2iq_{j+1}d_j}} \dots\dots\dots (2.5)$$

Where, $r_{j,j+1}$ is the reflectivity from the interface of the j and $j+1$ layers.

This is called Parrat's recursive method⁵⁸.

As the interface is not perfectly sharp, the reflectivity is exponentially damped due to roughness σ and is given by⁵⁸

$$R(q) = R_F(q) e^{-q^2 \sigma^2} \dots\dots\dots (2.6)$$

The roughness reduces the reflected intensity immensely. It causes diffuse scattering. The interface roughness should not be large than 2 to 3 nm⁵⁶.

The interference of the waves reflected from the interfaces causes oscillation of period⁵⁶

$$\Delta q_z = \frac{2\pi}{d} \dots\dots\dots (2.7)$$

Also, amplitude of the thickness fringes increases with the increase in the density⁵⁶.

In X-ray reflectivity (XRR) measurements, the wavelength of X-ray is fixed and varied the angle of incidence. The XRR measurements are performed for all my samples in X-ray diffractometer manufactured by Rigaku. In this measurement, the angle of the detector 2θ is varied from 0 to 10° and the detector records the intensity of the reflected beam. The reflected intensity generates from the constructive interference of the waves of the X-ray beam from various interfaces.

2.4 Ferromagnetic Resonance (FMR) setup:

Spin resonance in ferromagnetic materials is called ferromagnetic resonance²¹. To observe spin resonance, the thin film sample must be put in a magnetic field such that each spin will precess with Larmor frequency where precession frequency ν is proportional to H .²¹

Through the coplanar waveguide (CPW), an alternating magnetic field in the form of microwave power is applied at right angle to the static magnetic field. When the frequency of the microwave field matches with the precession frequency, resonance is observed²¹. At resonance, a sharp drop in transmitted microwave power is found. In the presence of the field, the atomic moments are distributed in the $2J+1$ energy level. The potential energy of each atomic moment in magnetic field is $(-\mu_H H)$ ²¹.

The separation between the levels is given by²¹

$$\Delta(E) = \Delta(\mu_H H) = g \mu_B H \dots\dots\dots (2.8)$$

Where, $\mu_H = g M_J \mu_B$, g is the spectroscopic splitting factor, M_J is the quantum number of J .

For any given value of J , the adjacent value of M_J differs by unity.

At resonance, this energy difference of the atomic levels (given in eq. 2.8) is equal to the energy of the microwave through the CPW which is $h\nu$.²¹

So, $h\nu = g\mu_B H$ (2.9)

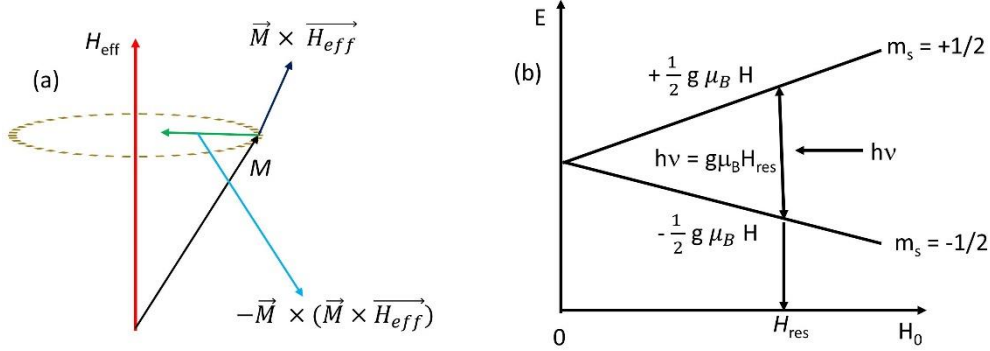


Figure 2.7: (a) precession of the magnetic moment with a magnetization vector M towards the effective magnetic field direction due to the presence of damping like torque, (b) the splitting of the energy levels in the presence of magnetic field where the energy difference of the atomic levels at resonance $g\mu_B H_{res}$ is equal to the energy of the microwave power $h\nu$.

Figure 2.7 (a) shows the magnetic moment precession around the direction of effective magnetic field with the damping like torque effect which is different for different materials. (b) shows the electron ferromagnetic resonance where the microwave power energy is equal to the energy difference of atomic levels which is formed in presence of magnetic field.

The precession of magnetization around the effective magnetic field direction can be due to both precessional torque and the damping term. Considering both the terms the effective torque can be written in the form of Landau-Lifshitz equation²¹:

$$\frac{\partial \vec{M}}{\partial t} = -\gamma (\vec{M} \times \vec{H}_{eff}) - \lambda \frac{\vec{M}}{M^2} \times (\vec{M} \times \vec{H}_{eff}) \quad \dots\dots\dots (2.10)$$

In the above equation, the first term is the precessing torque and the second term is the damping like torque with adjustable damping parameter is defined as λ and $\gamma = ge/2mc$, where c is

the velocity of light, e and m are the mass and charge of electron, respectively. An alternating damping like torque is proposed by Gilbert which is given below;

$$-\frac{\alpha}{M}(\vec{M} \times \frac{d\vec{M}}{dt}), \text{ where } \alpha = \frac{\lambda}{\gamma M}$$

So, the Landau-Lifshitz-Gilbert equation is given as⁵⁹

$$\frac{\partial \vec{M}}{\partial t} = -\gamma (\vec{M} \times \vec{H}_{eff}) - \frac{\alpha}{M} (\vec{M} \times \frac{d\vec{M}}{dt}) \dots\dots\dots (2.11)$$

Figure 2.8 shows the schematic of CPW FMR with the use of lock-in amplifier. In this FMR setup, we sweep the external applied magnetic field and hold the frequency of the perturbing field (h_{rf}) constant.

The effective magnetic field is defined as⁶⁰;

$$H_{eff} = H_{ext} + H_{an} + h_{rf} + H_{demag} + \dots \dots\dots (2.12)$$

Where, H_{ext} , H_{an} and H_{demag} are the externally applied magnetic field, the anisotropy and the demagnetization fields, respectively.

We can write, $\frac{dM}{dt} = -\gamma(M \times H_{in})$

The demagnetizing field $H_d = -NM$, where the demagnetization tensor is defined as⁶¹

$$N = \begin{bmatrix} N_x & 0 & 0 \\ 0 & N_y & 0 \\ 0 & 0 & N_z \end{bmatrix}$$

The modified magnetic field can be written as; $H_{in} = H'_0 - N_i M_i$

The oscillating component of magnetization in x-y plane is defined as⁶¹;

$$\frac{dM_x}{dt} = -\mu_0 \gamma [H'_0 + (N_y - N_z)M]M_y \dots\dots\dots (2.13)$$

$$\frac{dM_y}{dt} = -\mu_0 \gamma [H'_0 + (N_x - N_z)M]M_x \dots\dots\dots (2.14)$$

Where $M_z = M$ and the external field $B'_0 = \mu_0 H'_0$ is applied in the z-direction.

The solution of the equation is the Kittel equation and is given by;

$$\omega_0^2 = \gamma^2 \mu_0^2 [H'_0 + (N_y - N_z)M][H'_0 + (N_x - N_z)M] \dots\dots\dots (2.15)$$

A thin film with negligible in-plane anisotropy and $N_y = N_z = 0$ and $N_x = 1$, we have⁶¹

$$\omega_0 = \gamma\mu_0[H'_0(H'_0 + M)]^{1/2} \dots\dots\dots (2.16)$$

Magnetocrystalline anisotropy also affects ferromagnetic resonance precession frequency. In the presence of magnetocrystalline anisotropy, the above equation modifies to^{61,62}

$$\omega_0 = \gamma\mu_0[(H'_0 + H_{an})(H'_0 + H_{an} + M)]^{1/2} \dots\dots\dots (2.17)$$

Where $H_{an}=2K_1/M_S$ is the anisotropy field.

Using Kittel formula, the values of saturation magnetization M_S , spectroscopic splitting factor g and magnetic anisotropy field H_{an} of thin films with in-plane magnetization are extracted.

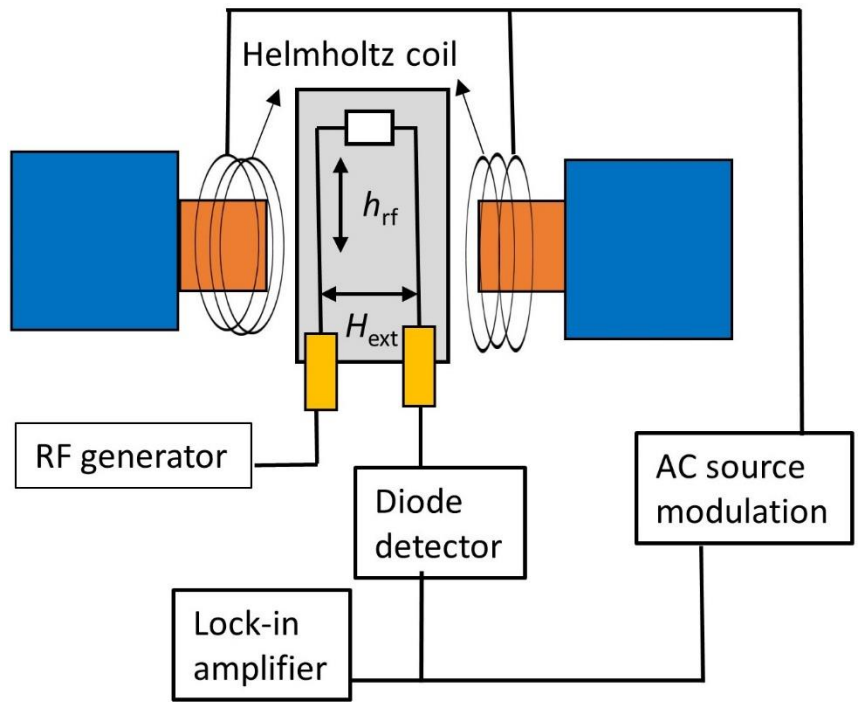


Figure 2.8: Schematic of CPW-FMR with lock-in amplifier.

Using the linewidth ΔH vs frequency f plot, the parameters such as the Gilbert damping constant α and inhomogeneous linewidth broadening ΔH_0 can be extracted.

The setup in lab is incorporated with a lock-in amplifier. The work of lock-in amplifier is to do the phase-sensitive detection. It finds the signal from the noise which has several orders of large magnitude than the signal. A pair of Helmholtz coils incorporated with an ac source of 490 Hz are used for the lock-in FMR detection. This method modulates the FMR spectrum

such that the output is the derivative of absorption spectrum. After using the diode detector to take away the rf part of the signal, the lock-in amplifier is used to find the modulated response. The dynamic properties have been studied for ferromagnetic single layers and bilayers by ferromagnetic resonance (FMR) spectroscopy manufactured by Nano-Osc⁶³.

2.5 Superconducting quantum interference device (SQUID) magnetometer:

Superconducting quantum interference device (SQUID) is a magnetic flux detector with high sensitivity⁶⁴. One can measure magnetic moment in the order of 10^{-7} emu or less using this SQUID magnetometer⁶⁵. Certain materials undergo a transition from normal to superconducting state when the temperature approaches to absolute zero. Kamerlingh-Onnes discovered in 1911 that the resistance of mercury drops to a very low value when the temperature goes below 4.2 K⁶⁴. The reason of resistance in a normal material is the scattering of electrons during their movement. But in superconductors, the electrons condense into Cooper pairs due to phonon exchange among them such that the Cooper pairs can move without scattering according to Bardeen-Cooper-Schrieffer (BCS) theory⁶⁴. SQUID consists of a superconducting ring separated by one or two Josephson junctions. Tunnelling of electrons through superconductor ring separated by resistive barrier is discovered by Josephson in 1962. The resistive barrier must be a “weak link”⁶⁴. It is necessary to apply a bias current (I_b) to SQUID. When I_b is slightly higher than the critical current (I_c), a change in voltage drop is found in the Josephson junction with the variation of external magnetic flux. The change in voltage is a measure of the external magnetic flux coupled to the SQUID. SQUID has small area and inductance of $\sim 10^{-10}$ H. By increasing the area of the loop, the inductance increases which nullifies much of sensitivity gain. The flux transformer is also used as the detection coil which has high input impedance, relatively large loop area and high inductance⁶⁴.

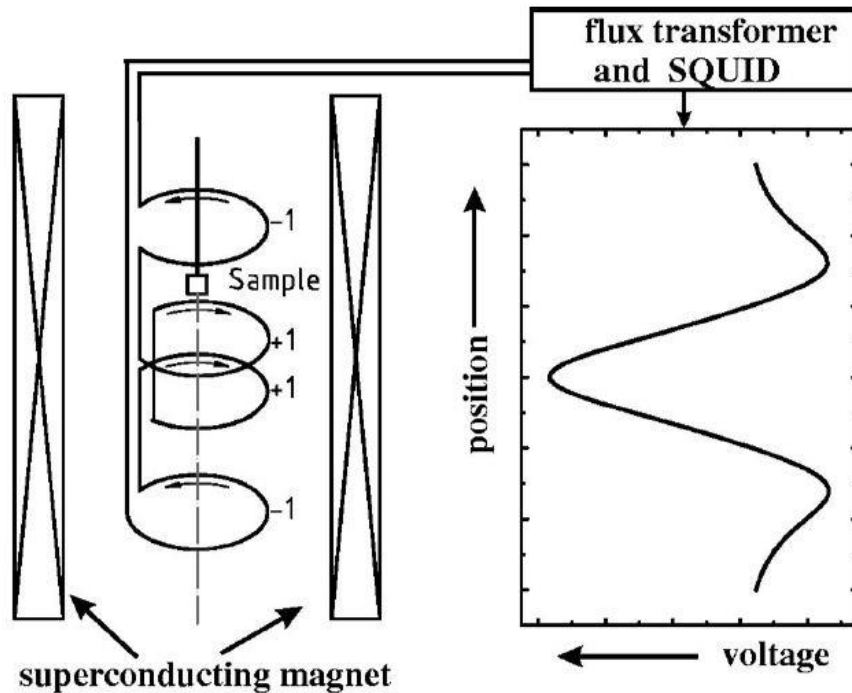


Figure 2.9: Schematic of the pick-up coils, the sample moves inside it which is inductively coupled to the SQUID via an input transformer placed in the magnetic field generated by superconducting magnet and the theoretical response against the position of the sample in the pick-up coils is also shown^{65,66}. This figure is taken from the reference 66.

The hardware components of magnetic property measuring system (MPMS3) are the following: the temperature controller allowing the temperature to be in the range of 1.8 to 400 K, magnetic field controller letting magnetic field to be in the range of 7 T to -7 T, the motion controller for scanning the sample in the field, the superconducting quantum interference device (SQUID) detection system for sensing the induced signals from the pickup coils, controller for controlling the chamber atmosphere and the cryogen. Liquid helium is required to cool the superconducting solenoid, superconducting electrical leads, quick switch etc. Niobium-Titanium (NbTi) superconducting solenoid provides the magnetic field which is placed outside of the cryogenic insert. The cryocooler part consists of cold head and compressor. It is a closed cycle, pulse tube cryo-refrigerator that uses helium gas for operation.

The cold head cools the condenser and dewar shield whereas compressor drives the cold head. The above figure 2.9 shows the coupling of the induced magnetic moment, generated by oscillations through the pick-up coils, to the SQUID via an input transformer and the response of the sample with its position inside the pick-up coils.

The dc scan method is used in this technique to measure the magnetic flux in the superconducting loop. Besides the dc scan method, oscillation of the sample occurs sinusoidally and lock-in amplifier is used to measure the magnetic flux. The sample is inductively coupled to the magnetic field which is placed inside the pickup coils and gives rise to current in the pickup coils. The coil geometry is chosen to maximize the sample response. The current in the superconducting pick up coils are inductively coupled via an input transformer to SQUID which acts as current to voltage converter.

Two parallel Josephson junctions are formed in the SQUID when two superconductors separated by a thin insulating layer. SQUID has a great sensitivity which can measure one flux quantum change in magnetic field⁶⁷ and is given by;

$$\varphi_0 = \frac{2\pi\hbar}{2e} \cong 2.0678 \times 10^{-15} \text{ tesla.m}^2$$

The supercurrent between two superconductors is related to the phase difference of the Cooper pair across the superconductors separated by an insulator. Since phase difference of the waves between two superconductors can be altered by magnetic flux, then we can measure the change in magnetic field⁶⁸.

The wave function of the Cooper pair can be given as

$$\Psi(\vec{r}) = \sqrt{n_s} \cdot e^{i\varphi(\vec{r})} \dots\dots\dots (2.18)$$

Where $n_s = \Psi \cdot \Psi^*$ is the Cooper pair density, $\varphi(\vec{r})$ is the phase.

Using the Schrodinger equation with the above wave function, Josephson derived the first Josephson equation where the tunnelling current is directly related to the phase difference which is given below⁶⁸,

$$I_S = I_0 \cdot \sin(\varphi_2 - \varphi_1) \dots\dots\dots (2.19)$$

The second Josephson equation is given by,

$$\frac{d}{dt}(\varphi_2 - \varphi_1) = \frac{qV}{\hbar} \dots\dots\dots (2.20)$$

The above equation indicates that the time evolution of the phase difference gives the voltage⁶⁸.

Using SQUID magnetometer, one can obtain the dynamic behaviour by applying a small alternating magnetic field where real and imaginary parts of ac susceptibility (χ' and χ'') are measured w.r.t. temperature at different frequencies ranging from 1 to 444 Hz.

The magnetic *M-H* and ac susceptibility measurements have been performed using magnetic property measuring system (MPMS 3) manufactured from Quantum Design⁶⁹.

2.6 Magneto optic Kerr effect (MOKE) related phenomena:

The interaction of light with magnetically polarized matter results into magneto-optic effects⁷⁰. It is discovered by Michael Faraday in 1845 that there is rotation of the plane of polarization of incident plane polarized light after passing through matter placed in a magnetic field which is known as Faraday effect⁷⁰. In addition to Faraday effect, magneto optic Kerr effect (MOKE) arises after reflection of the light from the matter placed in a magnetic field. MOKE determines the surface magnetization of thin films with higher sensitivity than SQUID⁷⁰.

2.6.1 Theory of magneto-optic phenomena:

Light can be linearly, elliptically or circularly polarized. Linear polarized light is also called plane polarized light. The electric field vector of the linearly polarized light is perpendicular to the propagation direction. Linearly polarized light is composed of two circularly polarized components namely left hand circularly polarized light (LCP) and right hand circularly polarized light (RCP) where the amplitudes of left and right handed circularly polarized light is defined such that $E_L=E_R=E/2$. Elliptically polarized light consists of two linearly polarized light those are out of phase and different amplitude. If the amplitude of two linearly polarized

components are same then it is called circularly polarized light.

Consider that light is propagating through a medium made of free electrons and fixed positive centres such that it maintains charge neutrality. In magnetic field absence, the radius of left and right circular motion are same and is given by⁷⁰;

$$r_{L,R} = \frac{eE/2m}{(\omega^2 - \omega_0^2)} \dots\dots\dots (2.21)$$

Where ω the angular frequency of radiation, E is is the amplitude of electric field, m is the electron mass, $\omega_0^2 = k/m$ is the material dependent constant, e is the elementary charge.

From the relations $P=NP_i=NeR$ and $D=\epsilon_0E+P$, we can evaluate the dielectric constant ϵ

$$\epsilon = \epsilon_0 \left(1 + \frac{Ne^2/2m\epsilon_0}{\omega^2 - \omega_0^2}\right) \dots\dots\dots (2.22)$$

where, $n^2 = \frac{\epsilon}{\epsilon_0}$, N is the number of dipoles per unit volume, R is the radius of the circular orbit of electron, P is the electric polarization.

In presence of magnetic field, Lorentz force acts differently to left and right circular motion of the electron and therefore the radii of circular motion are different in this case⁷⁰;

$$r_{L,R} = \frac{eE/2m}{(\omega^2 - \omega_0^2 \pm \omega B e/m)} \dots\dots\dots (2.23)$$

As a result, the refractive index for left and right circular motion n_L and n_R are different. After travelling a distance L , there is phase difference between the left and right circularly polarized light. The phase difference is given by, $\Delta\theta = (\omega L/c) (n_L - n_R)$

The refractive indices n_L and n_R can be conveyed as⁷⁰,

$$n_{L,R} = n \left(1 \pm \frac{1}{2} \xi\right) \dots\dots\dots (2.24)$$

Where, $\xi = \left(\frac{\omega B}{m}\right) \left(\frac{1}{\omega^2 - \omega_0^2}\right)$

$$\theta = \frac{\omega L}{2c} (n_L - n_R) = \frac{ne}{2mc} \frac{\omega^2}{\omega^2 - \omega_0^2} LB \cong K(\omega) LB \dots\dots\dots (2.25)$$

Two events take place during the propagation of circularly polarized light consisting of left and right circularly light in magnetized medium⁷⁰

- (1) The two polarized components of circularly polarized light are propagating with different velocities in a magnetized media and therefore has a phase shift which leads to Faraday rotation.
- (2) The two polarized components can have different absorption coefficients in the medium which cause different amplitudes of the electric field vector E_L and E_R resulting into ellipticity.

Therefore, the refractive index $n_{L,R}$ can be expressed as complex number and is given by;

$$n^* = n + ik$$

One can consider the perturbation ξ in the refractive index in presence of magnetic field which depends not only on B but also on the angle with the propagation direction, $u_k = \mathbf{k}/k$.

Where \mathbf{k} is the wave vector in vacuum and u_k is its versor.

Generally, the perturbation ξ can be expressed as the product $Q \cdot u_k$.

Where, Q is the Voight vector.

$$n_{L,R} = n(1 \pm \frac{1}{2}Q \cdot u_k) \dots\dots\dots (2.26)$$

Where n is a complex refractive index, the real part of which is the general refractive index and the imaginary part of which depends on absorption coefficient.

2.6.2 Magneto-Optic Kerr Effect (MOKE):

In 1877, Kerr effect was discovered⁷⁰. Kerr effect is observed during reflection of polarized light from a metal surface in presence of magnetic or electric field. The rotation of the plane of polarization and ellipticity of the reflected light is dependent on the magnetization M and sample thickness. Its microscopic origin is Zeeman effect which is based on spin-orbit interaction and relativistic effect.

There can be three MOKE geometries namely polar, longitudinal and transverse Kerr effect which are magnetization direction dependent⁷⁰.

The polar Kerr effect

In polar Kerr effect, magnetization of sample is perpendicular to its surface that interacts with light of rectilinear polarization and incident in perpendicular direction wrt sample surface. As a result, rotation of plane of polarization occurs by an angle θ_k which is less than a degree and also the reflected light becomes elliptical⁷¹.

The longitudinal Kerr effect

In this case, sample has in-plane magnetization and light is propagated at oblique angle of incidence. If the reflected light has polarization, (i) perpendicular (s-polarization) or (ii) parallel (p-polarization) wrt the plane of incidence of light then ellipticity and rotation of plane of polarization of the incident light occurs⁷¹.

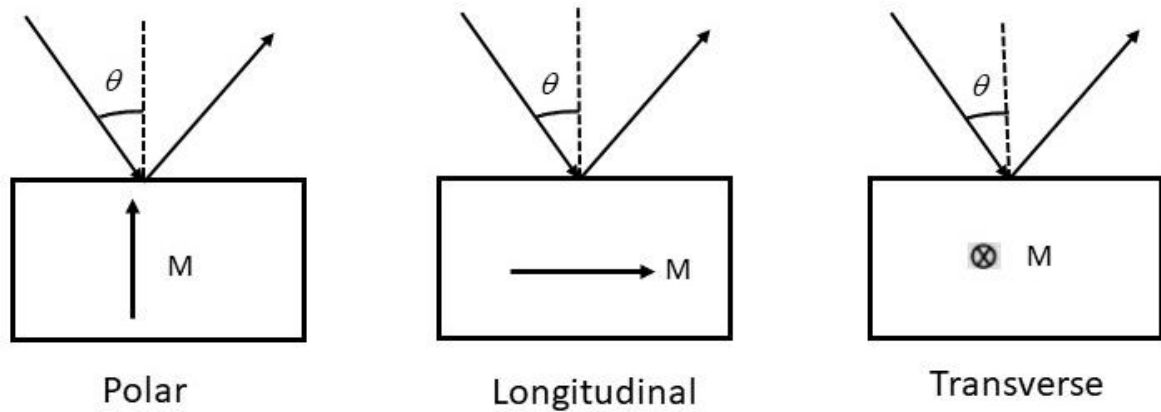


Figure 2.10: The three different geometries of magneto optic Kerr effect (MOKE) are polar, longitudinal and transverse.

The transverse Kerr effect

In this case magnetization is in-plane but perpendicular to plane of incidence of light. No rotation of plane of polarization happens for s or p polarization whereas in case of s polarization, there is not any effect at all. There is a change in intensity of the reflected light by reversing the direction of magnetization but this affects only to p polarization⁷¹.

Figure 2.10 shows the different geometries of magneto optic Kerr effect (MOKE).

Propagation equation: Eigenmodes

The expression of a propagating electromagnetic wave in a medium is given by⁷¹

$$E = E_0 \exp -i(\omega t - k \cdot r) \dots\dots\dots (2.27)$$

$$\text{and } B = \mu H = \mu_0 \mu_r H, \dots\dots\dots (2.28)$$

$$D = \epsilon_0 \epsilon E = \epsilon_0 E + P \dots\dots\dots (2.29)$$

Where, the relative electrical permittivity tensor is denoted as ϵ , the relative magnetic permeability tensor is denoted as μ_r .

The polarization vector can be written as the below equation⁷¹,

$$P = \epsilon_0 \chi_{el} E \dots\dots\dots (2.30)$$

Where, the electrical susceptibility is denoted as χ_{el} .

One can write $\epsilon = 1 + \chi_{el}$ and $\epsilon' = \epsilon - \sigma / i\omega \epsilon_0$

Where, σ is the conductivity tensor.

As ϵ and σ are tensors, so we can write ϵ' as⁷¹

$$\epsilon' = \begin{bmatrix} \epsilon'_{11} & \epsilon'_{12} & \epsilon'_{13} \\ \epsilon'_{21} & \epsilon'_{22} & \epsilon'_{23} \\ \epsilon'_{31} & \epsilon'_{32} & \epsilon'_{33} \end{bmatrix}$$

Since, $\epsilon_{ij} (M) = -\epsilon_{ji} (M) (i \neq j)$, therefore ϵ' takes the form⁷¹

$$\epsilon' = \begin{bmatrix} \epsilon'_{11} & \epsilon'_{12} & \epsilon'_{13} \\ -\epsilon'_{12} & \epsilon'_{22} & \epsilon'_{23} \\ -\epsilon'_{13} & -\epsilon'_{23} & \epsilon'_{33} \end{bmatrix}$$

If the magnetization direction is along the Z direction then no effect is found on the tensor for rotation around the axis and is given by⁷¹;

$$\epsilon' = \begin{bmatrix} \epsilon'_{11} & \epsilon'_{12} & 0 \\ -\epsilon'_{12} & \epsilon'_{11} & 0 \\ 0 & 0 & \epsilon'_{11} \end{bmatrix}$$

Showing the non-diagonal elements as the magneto-optical coefficient Q, the tensor can be expressed as⁷¹;

$$\epsilon' = \begin{bmatrix} \epsilon'_1 & iQ\epsilon'_1 & 0 \\ -iQ\epsilon'_1 & \epsilon'_1 & 0 \\ 0 & 0 & \epsilon'_1 \end{bmatrix}$$

The amplitudes of the reflected light for parallel p and perpendicular s polarizations wrt the plane of incidence are connected to the incident amplitude via the Fresnel coefficients and is given by⁷¹;

$$\begin{bmatrix} E_{p\ refl} \\ E_{s\ refl} \end{bmatrix} = \begin{bmatrix} r_{pp} & r_{ps} \\ r_{sp} & r_{ss} \end{bmatrix} \begin{bmatrix} E_{p\ inc} \\ E_{s\ inc} \end{bmatrix} \dots\dots\dots (2.31)$$

Where r_{ij} correspond to the amplitude ratio and $r_{ps} = E_{p\ refl}/E_{s\ inc}$.

The Kerr rotation, θ_{Kerr} and ellipticity η_{Kerr} for s and p lights are given by⁷¹;

$$\theta_{Kerr, s} = -Re(r_{ps}/r_{ss})$$

$$\theta_{Kerr, p} = Re(r_{sp}/r_{pp})$$

$$\eta_{Kerr, s} = Im(r_{ps}/r_{ss}) Re(r_{ps}/r_{ss})$$

$$\eta_{Kerr, p} = Im(r_{sp}/r_{pp}) Re(r_{sp}/r_{pp})$$

2.6.3 Kerr microscopy:

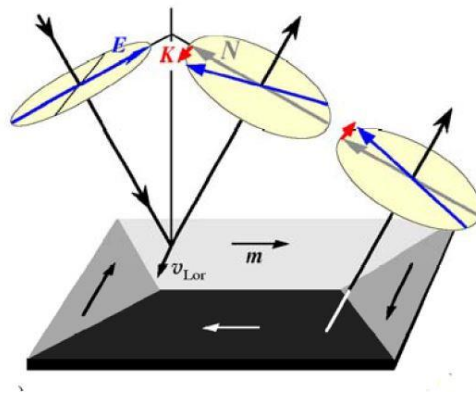


Figure 2.11: Schematic of longitudinal Kerr effect⁷². This figure is taken from the reference 72.

The interaction of electric field vector of the electromagnetic wave and magnetization of the sample placed in a magnetic field leads to Lorentz motion of the electrons in the sample⁷². This Lorentz motion of the electrons leads to the formation of the Kerr amplitude K , which is perpendicular to the normally reflected component N ⁷². A phase shift occurs in the reflected light due to the interference with the normally reflected component⁷². Figure 2.11 shows the

schematic of longitudinal Kerr effect with the formation of Kerr amplitude K after reflection from the sample surface.

Figure 2.12 shows the different component of Kerr microscopy. Unpolarized LED light is used as the light source in the Kerr microscopy setup of the lab. Using polarizer, an unpolarized light is converted into plane polarized light. The sample is placed in a magnetic field to induce net magnetization in the sample. The electric field vector of the LED source interacts with the magnetization of the sample to develop Lorentz motion $m \times E$ in the electrons of the sample. The light can reflect or transmit through

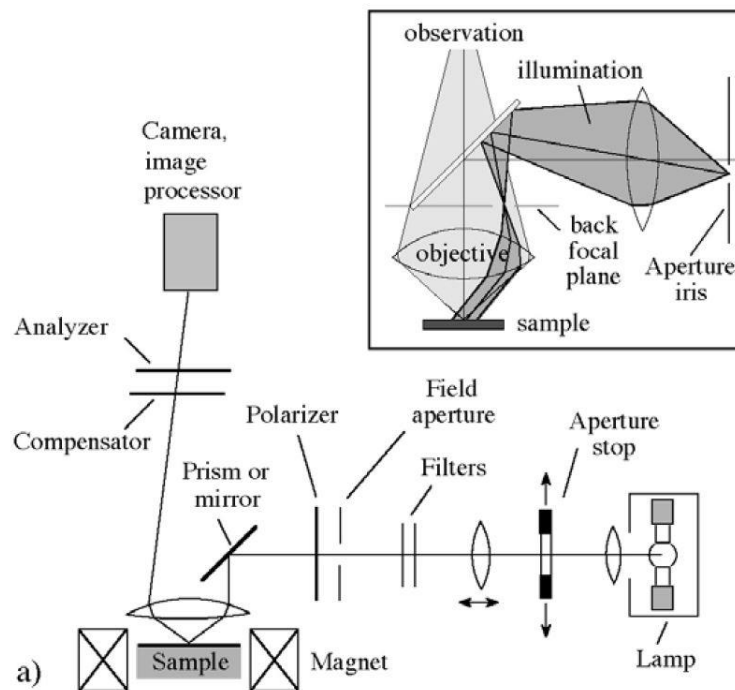


Figure 2.12: Shows various components of Kerr microscopy. For oblique incidence of light, the iris is deviated from its optical axis⁷². This figure is taken from the reference 72.

the sample. To observe Kerr effect, the light should be reflected from the sample surface. The reflected light becomes elliptically polarized after interaction of the light with the magnetization vector in the sample and also Kerr rotation appears. The reflected light then passes through the compensator. The compensator works in the same way as $\lambda/4$ plate. There

is a phase difference develops in the reflected elliptically polarized light after passing through compensator and then it becomes plane polarized. The plane polarized light then passes through the analyser. Consider the sample consists of magnetic domains with 180° domain wall. The interaction of the polarized light with the up spin is different from the interaction with the down spin. The Kerr rotation is different in both cases. If the up spin rotates the reflected light in clockwise direction then the down spin rotates the polarization of the reflected light in anti-clockwise direction. The analyser is crossed with one beam (which comes from the interaction with either up or down spin) and the domain appears dark in this case. Domains appear grey when the reflected beam is not extinguished from the analyser.

Longitudinal magneto optic Kerr effect (LMOKE) based microscopy and magnetometry measurements have been performed to study the magnetic hysteresis loop along with simultaneous domain imaging manufactured by Evico Magnetics Ltd., Germany⁷³. The magnetic field is generated by using an electromagnet and the current to the coils is given by Kepco power supply. The maximum magnetic fields are 1300 mT and 900 mT in the longitudinal and polar Kerr microscopy geometry, respectively. Instead of detector, a ccd camera is provided to capture the domain images. Using Kerr microscopy, one can find the anisotropy field $H_K=2K/M_S$, the magnetic hysteresis loop, and the magnetic domain images, respectively. The anisotropy field H_K is the saturation field along hard axis. The angle dependent ($0-360^\circ$) measurements are performed to find the anisotropy nature such as uniaxial, cubic and six-fold anisotropies.

2.7 Polarized neutron reflectivity (PNR):

X-ray does not give good contrast for light atoms but enough contrast is found from neutron. Magnetic information is found using neutron due to its magnetic moment whereas X-ray cannot provide magnetic information⁵⁷. One can neglect doubly scattered neutron due to weak scattering of it. This is called Born approximation⁷⁴. Perfect reflection of neutrons from the

surface occurs for angle of incidence less than critical angle and in this case Born approximation is not applicable⁷⁴. Above critical angle of incidence, the neutron reflectivity is found from the variation of the scattering length density perpendicular to the sample surface⁷⁴. Neutron reflectivity can be three types (1) specular neutron reflectivity (2) off-specular (diffuse) neutron reflectivity and (3) grazing incidence neutron reflectivity⁷⁴.

Advantages of neutron reflectivity⁷⁴: (1) reflectivity pattern is separate for Hydrogen (H) and Deuterium (D), (2) absorption is low, (3) method is non-destructive, (4) one can get magnetic density profile, (5) gives information of thickness ranging from 10 Å to 5000 Å.

Issues⁷⁴: (1) Unique solution for scattering length profile is not possible, (2) bigger samples with good contrast is required.

Refractive index for neutrons:

The neutron-nucleus potential for a single nucleus is given by⁷⁴

$$V(\vec{r}) = \frac{2\pi\hbar^2}{m} b\delta(\vec{r}) \dots\dots\dots (2.32)$$

Therefore, inside a medium the average potential is⁷⁴;

$$V(\vec{r}) = \frac{2\pi\hbar^2}{m} \rho \text{ where } \rho = \frac{1}{\text{Volume}} \sum_i b_i \text{ is the nuclear scattering length density (SLD).}$$

Inside the medium the total energy is $\frac{\hbar^2 k^2}{2m} + V$

Conservation of energy gives⁷⁴

$$\frac{\hbar^2 k_0^2}{2m} = \frac{\hbar^2 k^2}{2m} + V \dots\dots\dots (2.33)$$

$$\text{So, we get } k_0^2 - k^2 = 4\pi\rho \dots\dots\dots (2.34)$$

By using $k/k_0 = n$ and very small ρ , we can get⁷⁴

$$n=1-\lambda^2\rho/2\pi \dots\dots\dots (2.35)$$

Hence, we found that $n<1$, therefore total external reflection occurs.

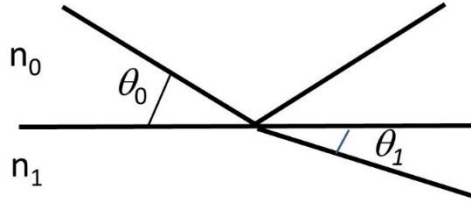


Figure 2.13: Schematic of neutron refraction from a surface at angle θ_1 and with refractive index n_1 different than incident beam medium with refractive index n_0 and angle θ_0 .

Neutron beam obeys Snell's law which is given below⁷⁵;

$$n = \frac{n_1}{n_0} = \frac{\cos \theta_0}{\cos \theta_1} \dots\dots\dots (2.36)$$

When there is total reflection, we have $\theta_0 = \theta_c$ and $\theta_1 = 0.0^\circ$

For, $\theta < \theta_c$ we have reflectivity $R=1.0$.

Whereas for $\theta > \theta_c$, reflectivity obeys Fresnel's law and is given by⁷⁵;

$$R = \left| \frac{n_0 \sin \theta_0 - n_1 \sin \theta_1}{n_0 \sin \theta_0 + n_1 \sin \theta_1} \right|^2 \dots\dots\dots (2.37)$$

Reflectivity from single and smooth interface is given by Fresnel's law⁷⁵.

As there is no absorption for most neutron wavelengths, we can neglect the dispersion correction for neutron scattering. For unpolarized neutron the refractive index is similar to X-ray and is given by⁵⁷;

$$n = 1 - \frac{2\pi}{k_0^2} N b_{coh} = 1 - \frac{2\pi}{\hbar} V_n \dots\dots\dots (2.38)$$

Where, b_{coh} is the coherent scattering length and V_n is the neutron-nucleus pseudo potential.

By replacing NZr_0 by Nb_{coh} we can get the refractive index for X-ray. Where N is the atomic number density, Z is the atomic number and r_0 is the classical electron radius.

The penetration depth of neutron is larger than X-ray as a result the product Nb_{coh} is much smaller than NZr_0 . Also, the critical perpendicular scattering vector for neutrons is 5 to 10 times smaller than X-ray scattering vector.

Neutron reacts with the magnetic moment of the sample therefore the refractive index is

expressed as the potential from magnetic moment V_m . If the magnetic moment of neutron is aligned parallel or antiparallel with the magnetic moment of the sample, the refractive index can be written as⁵⁷;

$$n(Q_0) = 1 - \frac{2\pi}{h} (V_n \pm V_m) \dots\dots\dots (2.39)$$

Where, V_m is the magnetic potential.

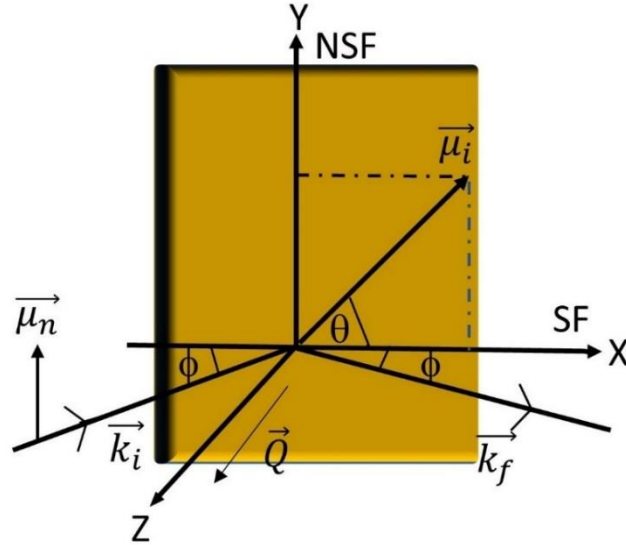


Figure 2.14: Schematic of the scattering geometry of spin polarized and monochromatic neutron beam. Spin flippers are used before and after the neutron reflection to find spin flip (SF) and non-spin flip (NSF) scattering.

Figure 2.14 shows the scattering geometry of polarized neutron beam with the incident wave vector k_i and reflected wave vector k_f . The scattering vector Q pointing normal to the sample surface gives the information about the sample.

Let us assume that magnetization in the sample is in-plane. To get maximum interaction of the neutron magnetic moment μ_n with the sample magnetic moment μ_s , magnetic moment of the neutron must be aligned parallel to the film plane. The neutron beam can be oriented parallel to y-direction after reflection from the supermirror. We can get the spin down state of neutron by activating the spin-flip filter in front of the sample. After reflection from the sample, a

second π flip filter sees if the spin has flipped after reflection or not. In the exit beam the supermirror acts as a spin flip filter. If both the spin flippers are deactivated then we will get non spin flip scattering (+ +) state and if both the flippers are activated then we will get the (- -) state⁵⁷. If one flipper is activated and other is deactivated then we will get the (+ -) and (- +) states respectively⁵⁷.

Let's assume that the magnetization of the sample makes an angle θ with the sample x-axis.

The interaction potential of neutron and i th layer sample magnetizations is given by⁵⁷;

$$V_{m,i} = -\mu_n \cdot B_i = -4\pi\mu_n\mu_i \sin \theta_i \dots\dots\dots (2.40)$$

Thus, the y component of magnetization is solely responsible for the change in effective potential. However, x component of magnetization is not responsible for the change in effective potential. The neutron spin state can be flipped from (+) state to (-) state due to the interaction of the neutron with the x component of the magnetization which occurs after neutron beam passes through some path length⁵⁷.

In neutron reflectivity measurements, either the wavelength of incident neutron or the angle of incidence is varied to find the chemical or magnetic density profile of the material⁷⁶. If the interface is not homogeneous then the angle of reflected neutron beam is different from the incident beam which is called off specular reflectivity⁷⁶. Momentum transfer can be perpendicular or parallel to the sample surface. Only the momentum transfer perpendicular to the surface is altered by the potential $V(Z)$. The perpendicular scattering vector is represented as⁷⁶;

$$Q_z = K_f - K_i = \frac{4\pi \sin \varphi}{\lambda} \dots\dots\dots (2.41)$$

The critical scattering vector is defined as

$$Q_c = \sqrt{16\pi N b} \dots\dots\dots (2.42)$$

Where, b is the scattering length.

For $Q > Q_c$, the reflectivity follows the $1/Q^4$ relation.

For $Q \gg Q_C$, the reflectivity from a series of L layers can be derived using first Born approximation and is given below⁷⁶;

$$R = \frac{1}{Q^4} |4\pi \sum_{l=1}^L [(Nb)_l - (Nb)_{l-1}] \exp(iQ_Z d_l)|^2 \dots\dots\dots (2.43)$$

where, d_l is the distance of the l_{th} layer from the top surface.

Layer selective magnetic properties in multilayers with subnanometer depth resolution can be obtained using Polarized neutron reflectivity (PNR). One can find the quantitative information of the interface such as magnetic moment, roughness, density, and thicknesss using PNR. PNR experiment was performed at room temperature using POLREF neutron reflectometer at Rutherford Appleton Laboratory, UK for characterizing Fe/NiFe bilayer samples.

Chapter 3

FM1/FM2 bilayers give optimum static magnetic properties for various applications due to the exchange coupling between the two ferromagnetic layers FM1 and FM2^{4,5,8-10}. Magnetic anisotropy has advantages in the retaining data in the presence of magnetic field in data storage devices. The anisotropy of magnetic materials has importance in determining the magnetization reversal mechanism⁷⁷⁻⁸². The effective magnetic anisotropy of a typical FM magnetic material system has contributions from the shape, surface, strain, magnetocrystalline and magnetostriction anisotropies⁷⁷. Magnetic anisotropy have been induced and tuned by utilizing various growth methodologies of FM materials like oblique angle of deposition⁷⁷⁻⁸¹, post deposition magnetic annealing⁸³, deposition in presence of magnetic field^{84,85}, growth on stepped substrate^{86,87}, placing the substrate at different position w.r.t. the flux direction⁸⁸, gradient composition sputtering⁸⁹, by changing the growth of the buffer layer⁹⁰ etc. Apart from the magnetic anisotropy, low Gilbert damping constant α of FM layer is also important for development of low power consumption devices, exhibiting less critical switching current density⁹¹, longer spin wave propagation lifetime etc. The value of the α has also been tuned by different deposition methods like working pressure⁹², glancing angle of deposition⁹³, different fabrication procedures etc. By depositing magnetic layer on top of polycrystalline seed layer, the α value increases due to extrinsic contribution of damping mechanism⁹⁴. Interface roughness⁹⁵, defects⁹⁵, spin pumping⁹⁵ and two-magnon scattering⁹⁴ also enhance damping in magnetic layers.

In this chapter, the static and dynamic magnetic properties of soft (Co)/hard (Co₄₀Fe₄₀B₂₀) magnetic bilayers have been studied. Magnetic bilayers have been fabricated in different deposition configuration and also the order of magnetic layers have been alternated with different thicknesses. Uniaxial magnetic anisotropy is found in all the bilayer samples due to

oblique angle of deposition of 30° wrt the substrate normal. Different deposition configurations modified the magnetic domain structures and magnetization reversal in the Co/CoFeB bilayer samples. Further, dynamic magnetic properties have been studied in these bilayers. The tuning of α is found in the magnetic bilayers using different deposition methodologies. Chapter 3 has been divided into two sections.

Section 3.1: Effect of sputtered flux direction of Co and CoFeB on magnetization reversal and damping properties in Co/CoFeB bilayers.

Section 3.2: Effect of order and thickness of Co and CoFeB layers on magnetic anisotropy and damping properties in Co/CoFeB bilayers.

Section 3.1: Effect of sputtered flux direction of Co and CoFeB on magnetization reversal and damping properties in Co/CoFeB bilayers.

3.1.1: Introduction:

Soft magnetic layers provide high M_S whereas hard magnetic layers provide high H_C and magnetic anisotropy³. Hard magnetic layer stabilizes soft magnetic layer against demagnetization. Soft/hard magnetic bilayers provide high M_S and H_C values compared to its constituent layers³. These magnetic bilayers provide high energy product $(BH)_{\max}$ value which have the application in permanent magnets^{4,5,8-10}. These magnetic bilayers are considered as single unit rigid magnet system when the soft and hard magnetic phases reverses at a single nucleation field H_N due to high exchange coupling between the magnetic layers. In addition to this, low α value is very important for the development of spin transfer torque-based memory devices¹¹ etc. α value depends on the magnetocrystalline anisotropy, exchange coupling between magnetic layers.

3.1.2: Experimental details:

The bilayers Co/ Co₄₀Fe₄₀B₂₀ including single layers of Co and Co₄₀Fe₄₀B₂₀ (CFB) have been

fabricated by dc magnetron sputtering on Si (100) substrate. The details of the sample structure are shown in the Table 3.1.1. The deposition is performed in ultra-high vacuum (UHV) chamber manufactured by Mantis deposition Ltd., UK. The base pressure in high vacuum chamber was better than 3×10^{-7} mbar. There are 8 sputter sources in the periphery of the sputtering system which are at an angle 45° wrt to each other. Thus, the atomic flux directions from the two neighboring sources on to the substrate plane are at angle of 45° wrt to each other. The CoFeB and Co targets are positioned at the 1 and 3 cusps, respectively. Therefore, the projection of atomic flux from Co and CoFeB targets on to the substrate plane are at an angle of 90° to each other (see fig. 3.1.1). Thus, in standard deposition condition the sputtered flux from Co and CFB targets are in perpendicular (\perp) configuration. Rotation of the substrate is performed by 90° after the deposition of first magnetic layer to deposit second magnetic layer. In this case, the angle between the sputtered fluxes onto the substrate plane is 0° i.e. the two

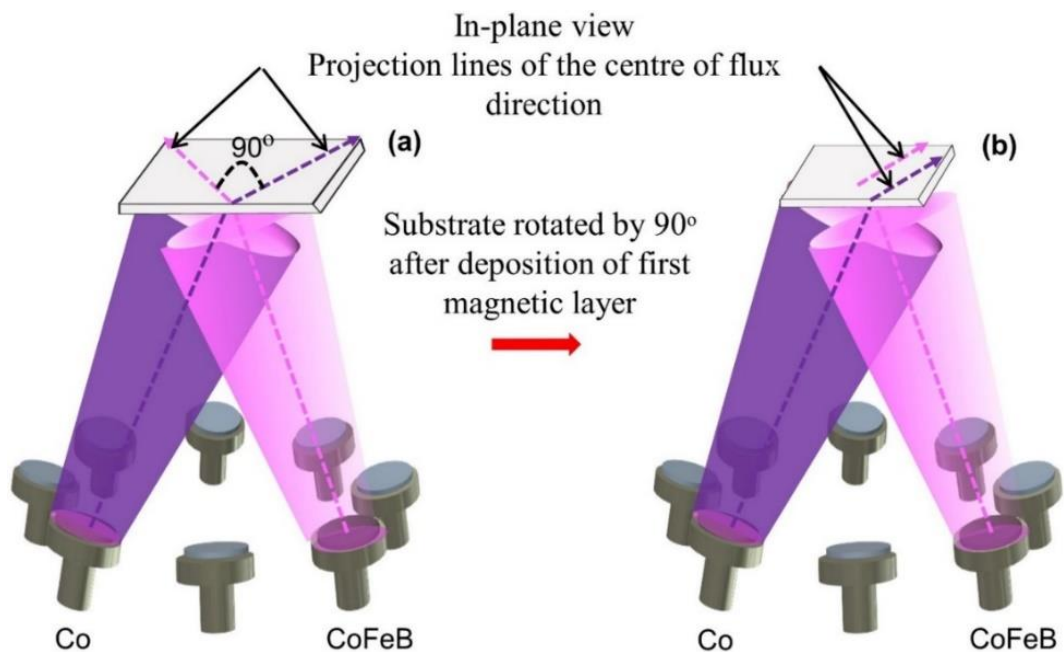


Figure 3.1.1: Schematic illustration of (a) perpendicular (\perp) (b) parallel (\parallel) deposition configuration.

layers are parallel to each other. This is named as parallel (\parallel) configuration. Magnetic domain imaging and hysteresis loops were taken by magneto-optic Kerr effect (MOKE) based microscopy. The dynamic magnetic properties have been studied by using ferromagnetic resonance (FMR) spectroscopy.

Table 3.1.1: The sample nomenclatures, structures, deposition configurations, substrate rotation speed, H_C along easy axis (EA) and hard axis (HA).

Name	Sample structure	Deposition configuration	Rotation Speed (rpm)	H_C (EA) (mT)	H_C (HA) (mT)
S1	Si(100)/Ta(3 nm)/Co(10 nm)/Ta(3 nm)	--	0	2.73	0.80
S2	Si(100)/Ta(3 nm)/CFB(10 nm)/Ta(3 nm)	--	0	8.89	0.34
S3	Si(100)/Ta(3 nm)/CFB(10 nm)/Co(10 nm)/Ta(3 nm)	CoFeB \perp Co	0	4.79	1.35
S4	Si(100)/Ta(3 nm)/CFB(10 nm)/Co(10 nm)/Ta(3 nm)	CoFeB \parallel Co	0	7.53	2.79
S5	Si(100)/Ta(3 nm)/CFB(10 nm)/Co(10 nm)/Ta(3 nm)	--	20	6.23	3.10

3.1.3: Magnetization reversal and magnetic domains:

Figures 3.1.2(a)-(d) show the magnetic hysteresis loop plots along $\phi = 0^\circ, 30^\circ, 60^\circ$ and 90° , respectively, measured by longitudinal magneto optic Kerr effect (LMOKE) based magnetometry at room temperature for all the samples. The square shaped loops along EA for all the samples indicates that the magnetization reversal is through domain wall motion.

The S-shaped loop along HA for all the samples indicates that the magnetization reversal is through coherent rotation. Sample S2 has higher H_C than sample S1. Thus, sample S2 is the hard-magnetic layer and sample S1 is the soft magnetic layer. It is found that magnetic bilayers have the higher H_C than S1 and lesser H_C than S2. Thus, the magnetic hardness of S2 is responsible for the elevation of H_C in magnetic bilayers. Sample S4 deposited in \perp configuration has higher H_C than sample S3 deposited in \parallel configuration. This can be explained in terms of grain growth in both the configurations. In \parallel configuration, the plume directions from the targets are parallel to each other whereas in \perp configuration, the plume directions

from both the targets are perpendicular to each other. Therefore, the interface roughness is more in the bilayer deposited in \perp configuration which gives a greater number of pinning

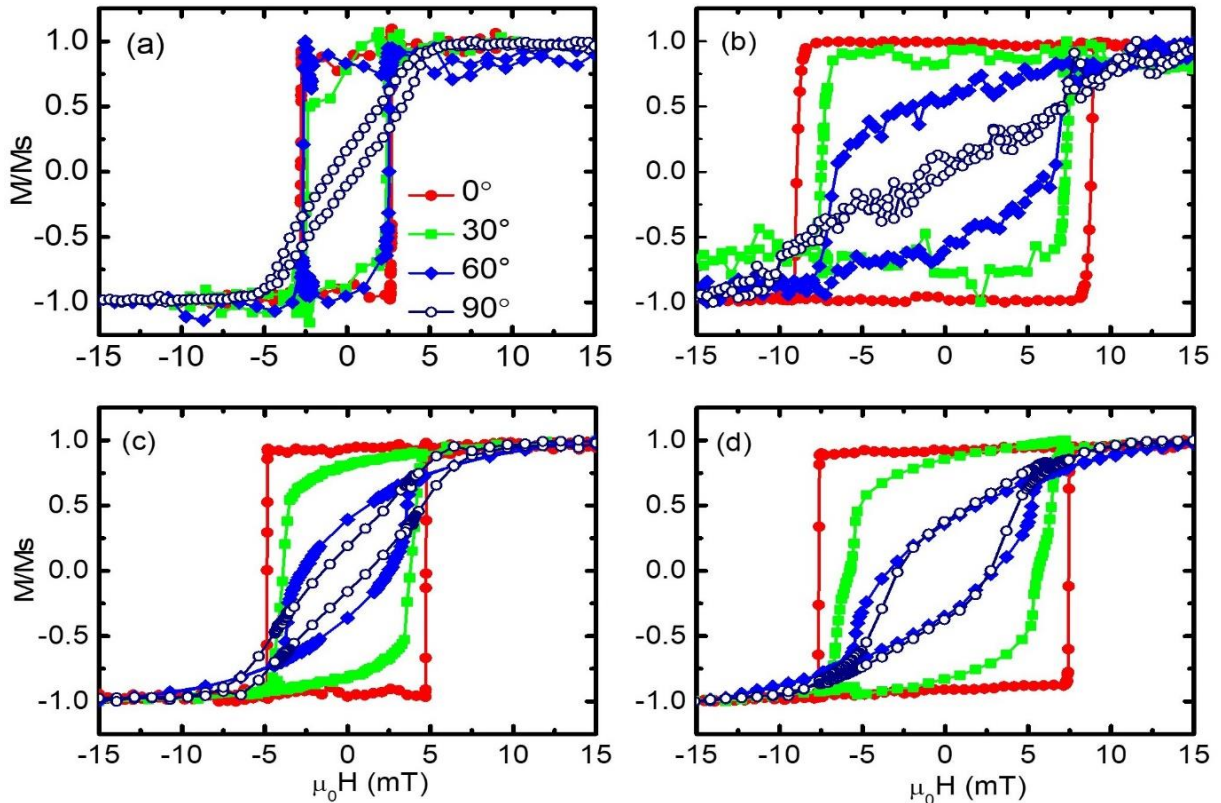


Figure 3.1.2: (a)-(d) show the magnetic hysteresis loops measured by longitudinal MOKE based magnetometry for the samples S1 to S4 along $\phi=0^\circ$ (EA), $30^\circ, 60^\circ$ and 90° (HA), respectively.

centres in sample S4 and thus higher H_C .

Figure 3.1.3 shows the plot of H_C as a function of angle ϕ for the samples S1-S4. It is observed that all the samples are showing uniaxial magnetic anisotropy irrespective of the deposition configurations. The change in coercivity between EA and HA directions is higher in sample S2, which indicates the presence of higher uniaxial magnetic anisotropy compared to other samples. This uniaxial magnetic anisotropy in all the samples is due to oblique angle of deposition. Sample S2 is a single layer CoFeB and its anisotropy is expected to be large compared to single layer of Co (sample S1). The other bilayer samples (S3 and S4) consists of

Co and CoFeB layers. Therefore, the anisotropy of samples S3 and S4 lie in between the values for samples S1 and S2. This is the reason among all samples the anisotropy is maximum for sample S2. We did not observe any crystalline peak in the XRD pattern which indicates that the grown CoFeB thin film is amorphous in nature. The magnetic anisotropy of CoFeB is growth induced (by oblique angle of deposition).

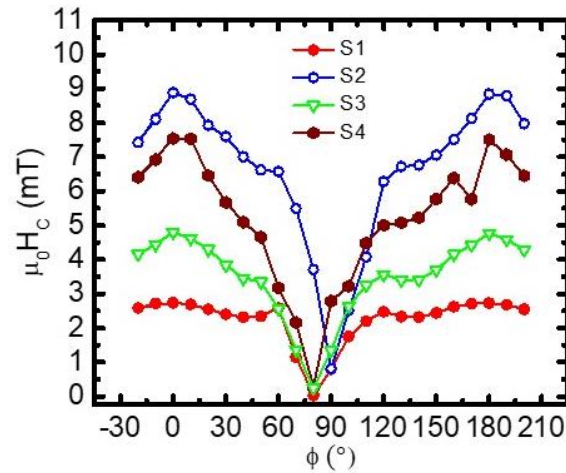


Figure 3.1.3: $\mu_0 H_C$ vs ϕ plot for all the samples.

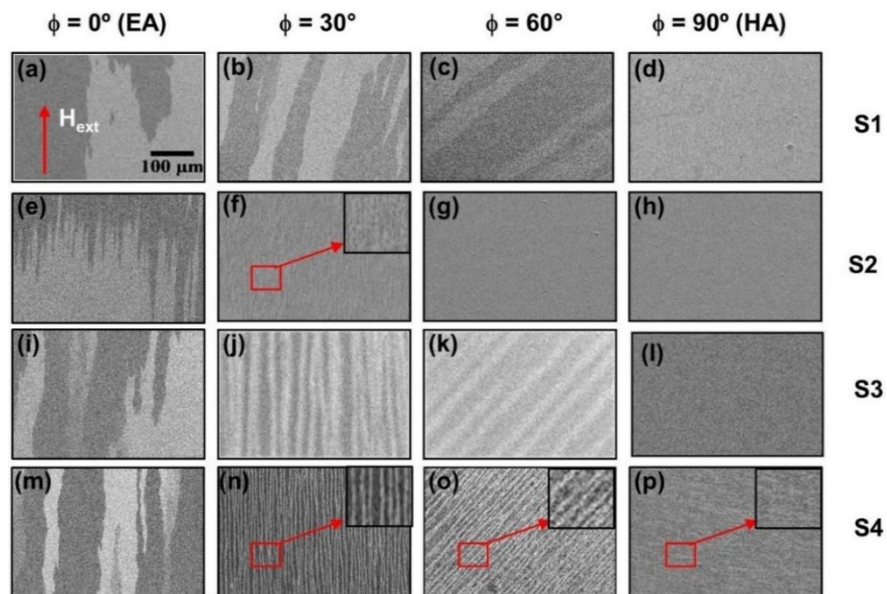


Figure 3.1.4: The magnetic domain images recorded by Kerr microscopy along $\phi = 0^\circ, 30^\circ, 60^\circ$ and 90° for the samples S1 to S4. The scale bar shown in figure (a) is valid for all the domain images. The insets shown in images (f), (n), (o), and (p) are the zoomed-in view of the square marked areas⁹⁶.

Figure 3.1.4 shows the magnetic domain images which are recorded along $\phi = 0^\circ, 30^\circ, 60^\circ$ and 90° for the samples S1 (a)-(d), S2 (e)-(h), S3 (i)-(l), S4 (m)-(p), respectively. One can observe two phase, three phase and multiphase domain branching depending upon the anisotropy of the system. Two phase domain branching is found in samples having uniaxial magnetic anisotropy. Two phase domain branching like branch domains are found along EA in sample S1 and stripe domains along EA in sample S2. Further, sample S2 has smaller domains in comparison to sample S1. The magnetic bilayers have magnetic domains with intermediate size of single layers. This is due to the direct exchange coupling of Co and CFB in the bilayers. Sample S4 has smaller stripe domains away from EA in comparison to sample S3. Therefore, it is concluded that deposition configuration can tune the shape and size of magnetic domains.

3.1.4: Damping properties:

Figure 3.1.5 shows the plot of FMR intensity vs applied magnetic field (H) for all the samples measured at 13 GHz frequency. The FMR data are fitted with Lorentzian shape function⁹⁷ to extract the values of line width (ΔH) and resonance magnetic field (H_{res}). Figure 3.1.6 (a) shows the plot of H_{res} vs frequency and 3.1.6 (b) shows the plot of ΔH vs frequency for all the samples. The values of effective demagnetization field ($4\pi M_{eff}$), anisotropy field (H_K), Lande's g-factor have been obtained using the following relation⁶².

$$f_{FMR} = \frac{\gamma}{2\pi} \sqrt{(4\pi M_{eff} + H_{res} + H_K)(H_{res} + H_K)} \quad \dots\dots\dots (3.1.1)$$

Where, $\gamma = \frac{g\mu_B}{\hbar}$. μ_B is the Bohr Magnetron and \hbar is the reduced Planck's constant.

ΔH vs frequency data are linearly fitted to find the value of α using the following equation:

$$\Delta H = \frac{4\pi\alpha f_{FMR}}{\gamma} + \Delta H_0 \quad \dots\dots\dots (3.1.2)$$

Where, ΔH_0 is the inhomogeneous line width broadening which comes from magnetic imperfections in the sample⁹⁸.

Table 3.1.2 shows the list of extracted parameters obtained from fitting equations (3.1.1) and

(3.1.2). α value of 0.0224 ± 0.0016 is found in CoFeB single layer which is much higher than Co single layer. Higher value of α in CoFeB layer may be due to large uniaxial magnetic anisotropy compared to the Co thin film. Bilzer et al., reported that the crystallization induced by annealing enhances damping constant⁹⁹. In this study, CoFeB is amorphous and the in-plane anisotropy of CoFeB is growth induced. Ta is a high spin orbit coupling material. The spin orbit coupling of Ta with CoFeB enhances the damping constant. Zhang *et al.*, also reported that the enhanced Gilbert damping constant is due to spin orbit coupling from GeBi in GeBi/NiFe bilayers¹⁰⁰. Further, higher value of α is observed in the magnetic bilayers in comparison to single layers. In literature, it has been reported that

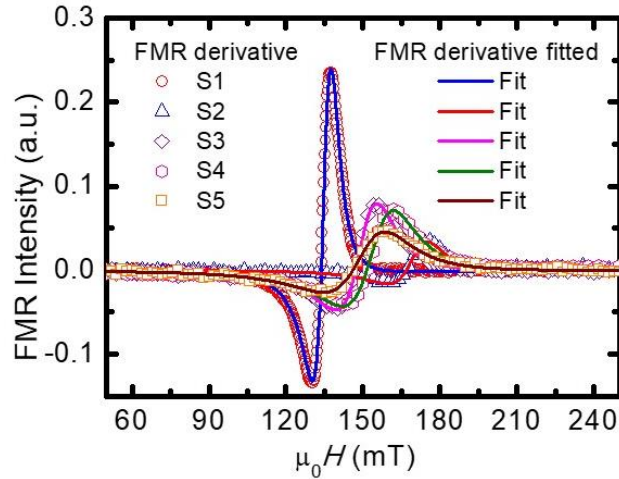


Figure 3.1.5: Shows the plot of FMR spectra vs applied magnetic field for all the samples. The open symbols are the experimental data taken at 13 GHz frequency and solid lines generated from the fitting of the experimental data with Lorentzian shape function.

Table 3.1.2: Extracted parameters α , ΔH_0 , $4\pi M_{eff}$, H_K , and g-factor evaluated by fitting data of H_{res} vs frequency and ΔH vs frequency using equation (3.1.1) and (3.1.2) for all the samples.

Sample	α	ΔH_0 (mT)	$4\pi M_{eff}$ (mT)	H_K (mT)	g-factor
S1	0.0136 ± 0.0001	0.10 ± 0.11	1387.7 ± 26.3	9.12 ± 0.16	2.125 ± 0.016
S2	0.0224 ± 0.0016	2.88 ± 1.56	1355.2 ± 105.2	20.14 ± 0.95	1.949 ± 0.060
S3	0.0236 ± 0.0011	2.08 ± 1.18	1856.1 ± 326.1	17.67 ± 1.31	1.814 ± 0.138
S4	0.0282 ± 0.0015	6.93 ± 1.40	1296.6 ± 89.3	16.32 ± 0.76	2.079 ± 0.057
S5	0.0204 ± 0.0006	18.20 ± 0.70	1708.2 ± 151.3	13.84 ± 0.78	1.832 ± 0.068

α is also dependent on growth conditions¹⁰¹ and compositions¹⁰². But, in our case deposition conditions were same in the magnetic bilayers whereas the flux directions from the targets are different. The value of α was lower in \parallel configuration compared the α value in bilayer deposited in \perp configuration. The different interface quality between Co and CoFeB might be a reason for different value of α in the two configurations. We have performed inverse spin Hall effect (ISHE) measurements to find if there is spin pumping from one FM layer to another. But, we could not observe any ISHE signal indicating that spin pumping may not be a reason for enhancement of damping constant in the studied magnetic bilayers. In order to understand the effect of anisotropy on the value of α , we have fabricated sample 5 at 20 rpm speed of substrate. It has been observed that the value of α in S5 sample is comparable to S3, whereas

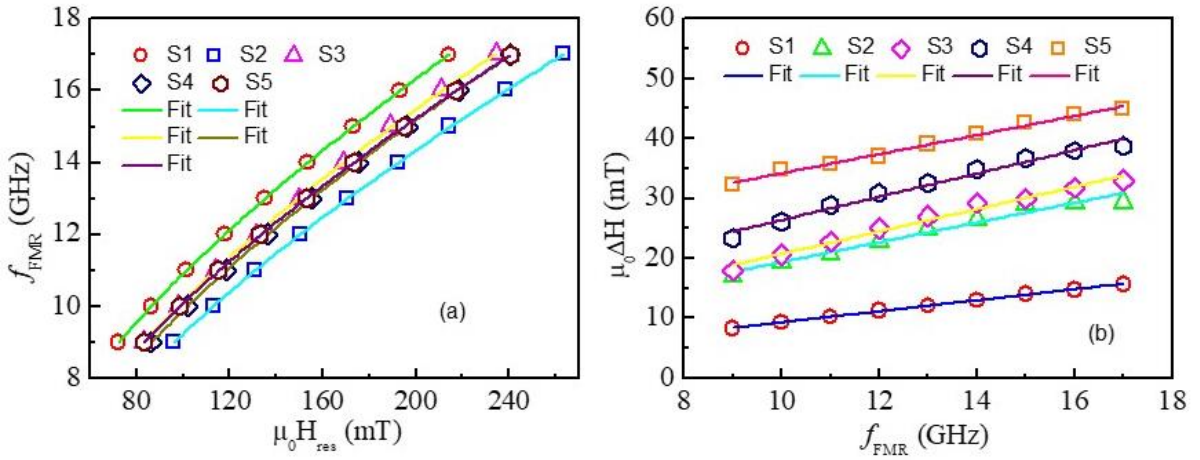


Figure 3.1.6: Shows the plot of H_{res} vs frequency (a) and ΔH vs frequency (b) for all the samples.

the H_K value is 21% less compared to this sample. Thus, a new deposition methodology is found to find a lower value of α and optimum value of H_K which is good from application point of view. It should be noted that error in ΔH_0 is more compared to the value for sample S1. This is due to noisy data and therefore, ΔH_0 approaches zero value. The obtained value

of inhomogeneous linewidth broadening ΔH_0 which is due to magnetic imperfections is high in magnetic bilayer deposited in \perp configuration. This indicates that the interface roughness is more in the magnetic bilayer deposited in \perp configuration. Also, $4\pi M_{eff}$ value is higher in the magnetic bilayer deposited in \parallel configuration. Anisotropy field value is similar in the magnetic bilayers deposited in \parallel and \perp configuration whereas the coercive field value is more in the magnetic bilayer deposited in the \perp configuration. The interface is smoother in \parallel configuration sample which leads to higher exchange coupling in this sample that results into lesser H_C .

From figure 3.1.6 (a), it is found that the linewidth of magnetic bilayers is more than the single layers. It is reported in literature that the linewidth value depends on the bilinear and biquadratic interaction between two ferromagnetic layers separated by a nonmagnetic layer and also on H_K ¹⁰³. But, in our case we have two ferromagnetic layers interacted through direct exchange coupling. Thus the direct exchange interaction might be a reason behind this higher value of linewidth value in the magnetic bilayers. The linewidth contains both the frequency dependent and independent part. The frequency independent part is the inhomogeneous linewidth broadening which comes from magnetic imperfections. However, the frequency dependent part originates from the intrinsic damping due to the effects of exchange interaction and spin orbit coupling. According to Kittel equation, the frequency is dependent on anisotropy field, exchange field etc. Further, the effective magnetic field is the sum of external magnetic field, exchange field, anisotropy and demagnetization fields. The expression for it is $H_{eff} = H_{ext} + H_{exch} + H_{ani} + H_{demag}$. Therefore, higher the values of exchange coupling and spin orbit coupling, we will find the higher values of intrinsic damping and hence, linewidth. Also the H_{res} value is the intermediate of Co and CoFeB single layers. It has been found that H_{res} value depends on coupling between two ferromagnetic layers separated by a non-magnetic layer¹⁰⁴. Thus the direct exchange coupling between Co and CoFeB magnetic layers is responsible for the modification of H_{res} value in the magnetic

bilayers.

3.1.5. Anisotropy energy:

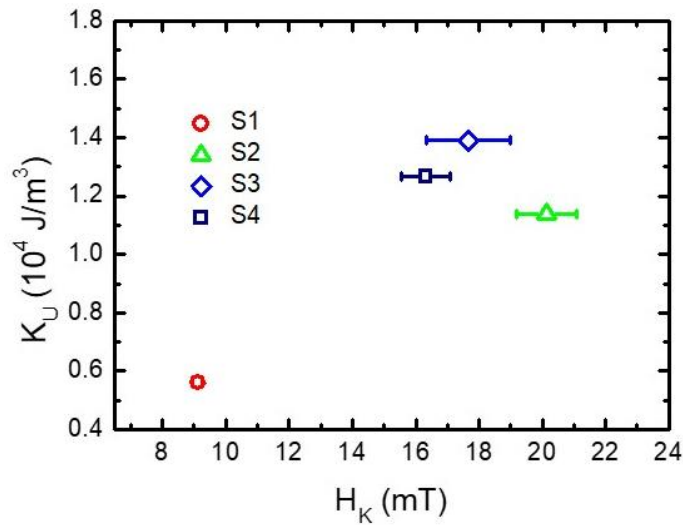


Figure 3.1.7: Anisotropy field (H_K) vs anisotropy energy (K_U) plot for the samples.

The anisotropy energy K_U vs anisotropy field H_K has been plotted for the samples S1-S4 which is shown in figure 3.1.7. The value of saturation magnetization (M_S) was measured from vibrating sample magnetometry (VSM) and H_K value from MOKE magnetometry to calculate the value of anisotropy energy K_U . Higher value of K_U is found in the magnetic bilayers than the single layers and also K_U is much higher in CoFeB than Co. Thus, CoFeB is much responsible for the enhancement of K_U in the magnetic bilayers.

3.1.6. Conclusions:

In this study, lower value of damping is found in magnetic bilayer deposited in parallel configuration (\parallel) than the magnetic bilayer deposited in perpendicular configuration (\perp). The elongation of sputtered flux at the interface is different in the different deposition configuration's which results into higher interface roughness in \perp configuration than \parallel configuration. Therefore, damping constant is high in magnetic bilayer deposited in \perp configuration. Magnetic bilayers have uniaxial magnetic anisotropy irrespective of the deposition configuration. The domain structure and coercivity in the magnetic bilayers showed

the combined effect of the individual layers. The magnetic anisotropy energy (K_U) is higher in the magnetic bilayers than the single layers. Thus, we have demonstrated a new deposition methodology to tune the magnetic properties.

Section 3.2: Effect of order and thickness of Co and CoFeB layers on magnetic anisotropy and damping properties in Co/CoFeB bilayers.

3.2.1: Introduction:

Magnetic properties of thin film systems can be tuned by the thickness and order of the various magnetic materials for various applications^{4,5,8-10}.

Rementer *et al.* has shown the tuning of the coercivity and linewidth systematically in FeGa/NiFe system by increasing the number of interfaces with decreasing the individual layer thickness with keeping total thickness fixed¹⁰⁵. The multilayer of structure Ti(30nm)/[((Pr_{0.9}Dy_{0.1})(Fe_{0.77}Co_{0.12}Nb_{0.03}B_{0.08})_{5.5})(16 nm)/Fe(x nm)] \times 20/Ti(30 nm)/(Si substrate) shows the decrease in H_C and increase in remanence with the increase in thickness of the soft magnetic layer due to effective exchange coupling between the soft and hard magnetic layers¹⁰⁶. Similarly, the multilayer of structure Ti(30 nm)/[((Nd_{0.95}Dy_{0.05})(Fe_{0.77}Co_{0.12}Nb_{0.03}B_{0.08})_{5.5})(15 nm)/Fe(y nm)] \times 20/Ti(30 nm)/(Si substrate) which is annealed at 600°C for 5 minutes has remanence enhancement and high energy product value compared to the soft magnetic layer due to the exchange coupling between the soft and hard magnetic phases¹⁰⁷. In NiFe(10–30 nm)/Co(10 nm) bilayers, the coercive field H_C decreases with the increase in soft layer thickness¹⁰⁸. In (FePt)_m/(FeCo)_n magnetic bilayers, the magnetization increases or decreases with the increase in FeCo or FePt layers whereas the anisotropy energy decreases with the increase in FeCo layers¹⁰⁹. In Co/NiFe system, by varying the thickness of NiFe, a change in interfacial exchange coupling and uniaxial magnetic anisotropy has been observed¹¹⁰. In epitaxial Fe₃O₄ (soft) /CoFe₂O₄ (hard) system, the

coercivity reduces with the increase in soft layer thickness and thus the switching field of the hard layer decreases¹¹¹. In this section, the order and thickness dependence of Co and CFB layers in Co/CFB bilayers on the magnetic anisotropy and damping properties have been studied.

3.2.2: Experimental details:

The Co/CFB bilayers and single layers of Co and CoFeB have been deposited in high vacuum of $\sim 5 \times 10^{-8}$ mbar on Si (100) substrate at room temperature. FMR measurements have been performed in 7-17 GHz frequency range. We placed the sample in flip-chip manner on the coplanar waveguide (CPW). Saturation magnetization (M_S) value have been obtained from superconducting quantum interference device (SQUID) based magnetometer manufactured by Quantum Design. Magnetic domain images, coercive field (H_C) and anisotropy field (H_K) have been found using Kerr microscopy.

Table 3.2.1: Sample nomenclature, structure, H_C along EA, H_C along HA and H_K in mT for all the samples.

Sample name	Sample structure	$\mu_0 H_C$ (EA) (mT)	$\mu_0 H_C$ (HA) (mT)	$\mu_0 H_K$
S1*	Si(100)/Ta(3 nm)/Co(5 nm)/Ta(3 nm)	2.3	1.2	5.5
S1	Si(100)/Ta(3 nm)/Co(10 nm)/Ta(3 nm)	2.7	0.8	5.5
S2*	Si(100)/Ta(3 nm)/CoFeB(5 nm)/Ta(3 nm)	4.4	0.2	9.0
S2	Si(100)/Ta(3 nm)/CoFeB(10 nm)/Ta(3 nm)	8.9	0.8	11.5
S10	Si(100)/Ta(3 nm)/Co(5 nm)/CoFeB(10 nm)/Ta(3 nm)	2.2	0.2	5.7
S11	Si(100)/Ta(3 nm)/Co(10 nm)/CoFeB(5 nm)/Ta(3 nm)	3.6	3.1	5.8
S12	Si(100)/Ta(3 nm)/CoFeB(5 nm)/Co(10 nm)/Ta(3 nm)	4.3	1.4	4.2
S13	Si(100)/Ta(3 nm)/CoFeB(10 nm)/Co(5 nm)/Ta(3 nm)	3.4	0.1	5.6

Sample nomenclature, structure, H_C along EA, H_C along HA and H_K for all the samples are given in table 3.2.1.

3.2.3: Magnetization reversal, anisotropy, and domain imaging study:

Figure 3.2.1 shows the magnetic hysteresis loops of samples S1* (a), S1 (b), S2* (c) and S2

(d), respectively along $\phi = 0^\circ, 30^\circ, 60^\circ$ and 90° measured using LMOKE based magnetometry at room temperature. H_C for CoFeB is higher than Co indicating that CoFeB is relatively harder than Co. So, Co is the soft magnetic layer and CoFeB is the hard-magnetic layer in this case. Figure 3.2.2 shows the magnetic hysteresis loops of samples S10 (a), S11 (b), S12 (c) and S13 (d) along $\phi = 0^\circ, 30^\circ, 60^\circ$ and 90° measured using LMOKE based magnetometry at room temperature. The square shaped loops along EA indicates that magnetization reversal is through domain wall motion. The S-shaped loops along hard axis indicates that the magnetization reversal is through coherent rotation. It is found that the H_C

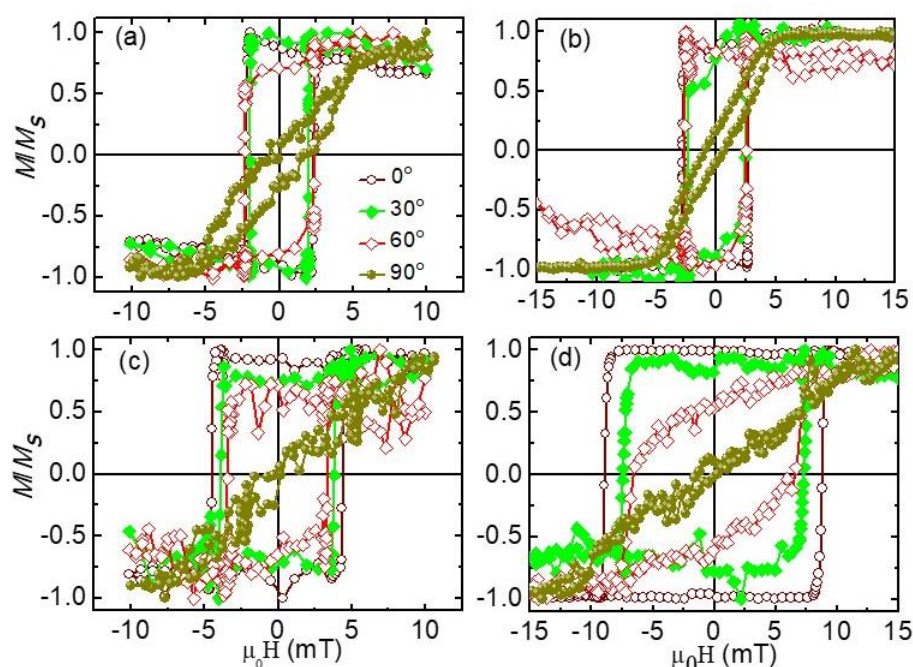


Figure 3.2.1: (a)-(d) show the magnetic hysteresis loops of samples S1*, S1, S2* and S2, respectively measured using LMOKE based magnetometry at room temperature along $\phi = 0^\circ$ (wine curve), 30° (green curve), 60° (red curve) and 90° (dark yellow curve).

value of sample S11 is higher than S10. Thus, by increasing the thickness of soft Co layer from 5 nm to 10 nm and decreasing the thickness of CoFeB magnetic layer from 10 nm to 5 nm, the H_C value increases. Similarly, sample S12 has higher H_C than sample S13. This is due to increased interfacial exchange coupling between Co and CoFeB magnetic layers. It is also

found that S13 has higher H_C than S10. Similarly, sample S12 has higher H_C than S11. Thus, by alternating the order of magnetic layers an enhancement of H_C is found when CoFeB is at the bottom. The increased interfacial exchange coupling by alternating the order of magnetic layers might be the reason for the increase in H_C value. Figure 3.2.3 shows the magnetic domain images of samples S10-S13 along $\phi=0^\circ, 30^\circ, 60^\circ$ and 90° measured using LMOKE based microscopy at room temperature. Big branch domains are observed along EA for the samples S10-S13. So, domain size and type are not affected by changing the order of Co and CFB layers along EA. However, domain size and type are significantly affected by order

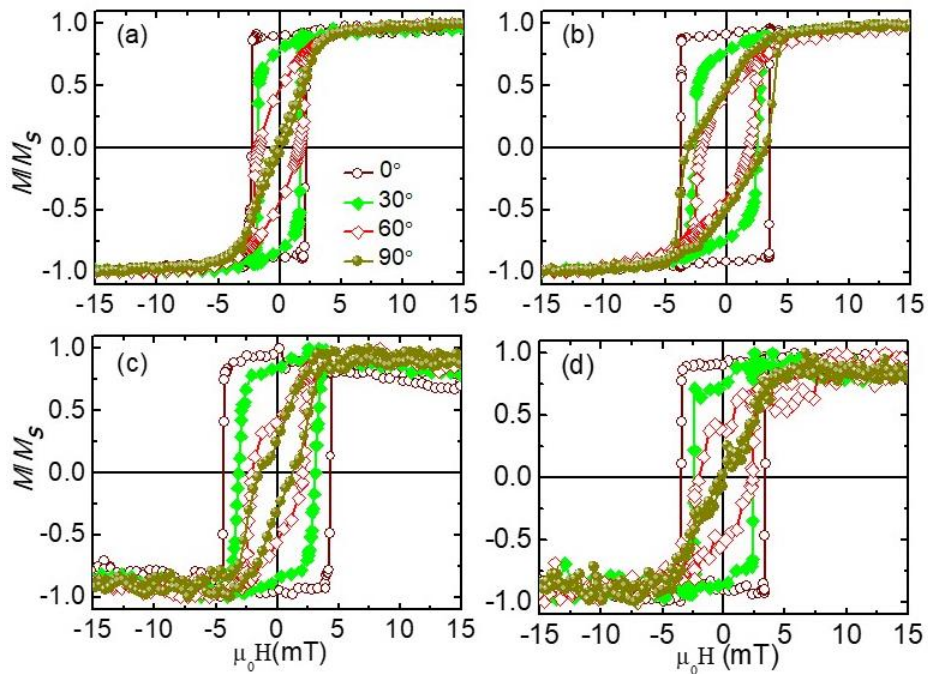


Figure 3.2.2: (a)-(d) magnetic hysteresis loops of samples S10-S13 measured using LMOKE based magnetometry at room temperature along $\phi=0^\circ$ (wine curve), 30° (green curve), 60° (red curve) and 90° (dark yellow curve).

of deposition of individual layers away from EA for all the samples. Big branch domains are found along $\phi=30^\circ$ and 60° for sample S10 whereas no magnetic domains along $\phi=90^\circ$. In sample S11, small stripe domains are found along $\phi=30^\circ$ and 60° and patch like domains along

$\phi=90^\circ$.

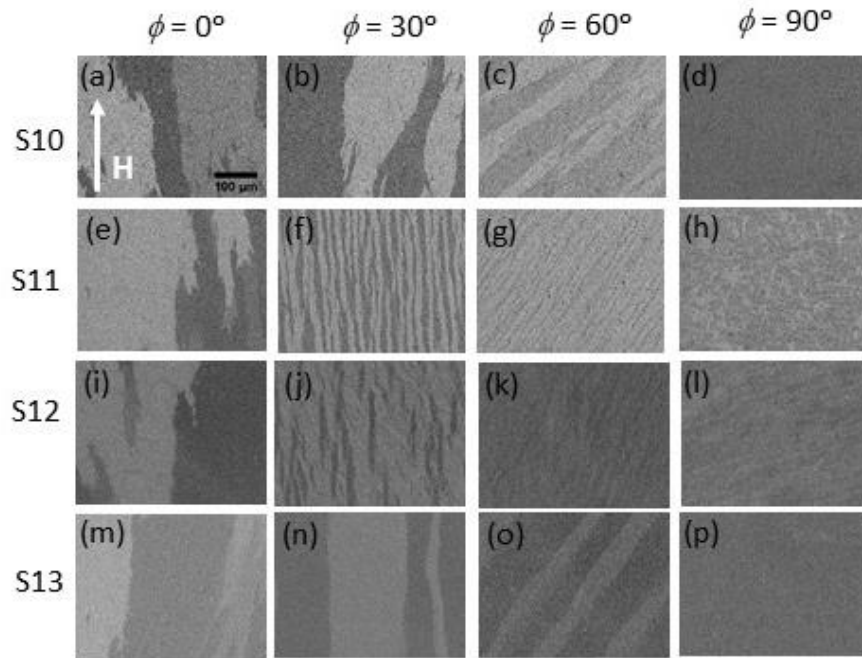


Figure 3.2.3. Shows the magnetic domain images along $\phi=0^\circ$, 30° , 60° and 90° measured using LMOKE based microscopy at room temperature for samples S10-S13, respectively.

Similarly, small branch domains are found along $\phi=30^\circ$, 60° and 90° in sample S12. In sample S13, big stripe domains are found along $\phi=30^\circ$ and 60° and no magnetic domains along $\phi=90^\circ$. Thus, with the increase in thickness of Co from 5 nm to 10 nm and decrease in thickness of CoFeB from 10 nm to 5 nm, the increase in interfacial exchange coupling along EA results into smaller magnetic domains away from EA in samples S11 and S12. Due to anisotropy dispersion, magnetic domains along HA are found for samples S11 and S12.

Figure 3.2.4 shows the anisotropy plot of all the samples. Samples S10 and S13 show a mixture of uniaxial and six-fold magnetic anisotropies. Sample S12 has uniaxial magnetic anisotropy. Sample S11 has uniaxial magnetic anisotropy with a peak along hard axis. Due to misalignment of local grain anisotropy¹¹², a peak along HA is found for the sample S11. It should be noted that uniaxial magnetic anisotropy is found in all the samples due to oblique

angle of deposition.

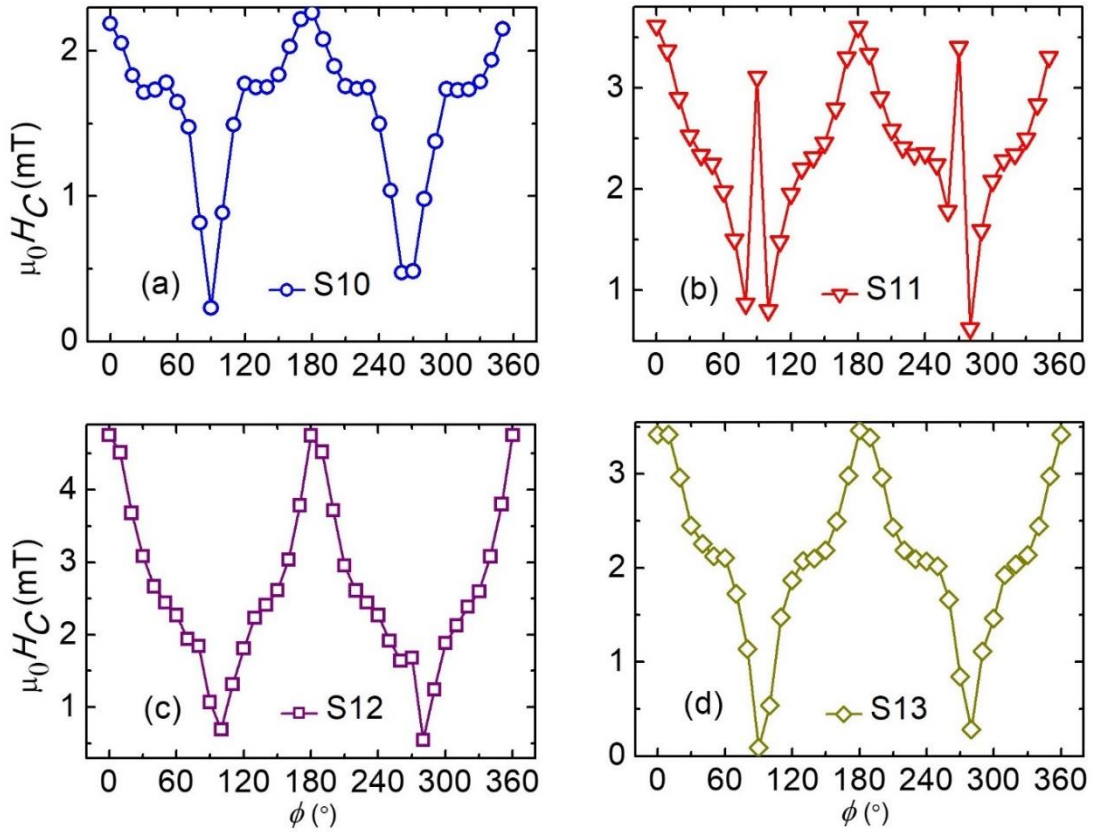


Figure 3.2.4: (a)-(d) show μ_0H_C vs ϕ plot for the samples S10-S13.

3.2.4: Damping properties study:

The frequency dependence of H_{res} and ΔH are shown in figs. 3.2.5 (a) and (b), respectively, for samples S10 to S13 (open symbol). Solid lines are the best fits using equation 3.1.1 and 3.1.2. The extracted parameters i.e. α , $\mu_0\Delta H_0$, $\mu_04\pi M_{eff}$, μ_0H_{Keff} in mT, g-factor, are given in the table 3.2.2.

The effective demagnetizing field ($4\pi M_{eff}$) is related to saturation magnetization M_S through the below relation;

$$4\pi M_{eff} = 4\pi M_S + \frac{2K_S}{M_S t_{FM}} \dots\dots\dots (3.2.1)$$

Where, K_S is the perpendicular surface anisotropy constant and t_{FM} is the thickness of the ferromagnetic layer.

Table 3.2.2: The values of the parameters α , $\mu_0\Delta H_0$, $\mu_04\pi M_{eff}$, μ_0H_{Keff} in mT, g-factor, M_S in emu/cc, K_U in J/m³ and K_S in erg/cm² for all the samples.

Sample name	α	$\mu_0\Delta H_0$ (mT)	$\mu_04\pi M_{eff}$ (mT)	μ_0H_{Keff} (mT)	g-factor	M_S (emu/cc)	$K_U \times 10^4$ (J/m ³)	K_S (erg/cm ²)
S10	0.0129± 0.0004	-0.9 ± 0.4	1470± 50	5.0± 0.2	2.02± 0.03	793	0.23	0.22 ± 0.03
S11	0.0184± 0.0002	-1.2 ± 0.1	1300± 30	6.5± 0.1	2.13± 0.02	1255	0.36	-0.21 ± 0.02
S12	0.0314± 0.0010	2.4 ± 0.8	1120± 80	3.4± 0.7	2.19± 0.06	1094	0.23	-0.17± 0.06
S13	0.0229± 0.0006	2.1 ± 0.5	1200± 50	9.8± 0.4	2.04± 0.03	756	0.21	0.11 ± 0.02

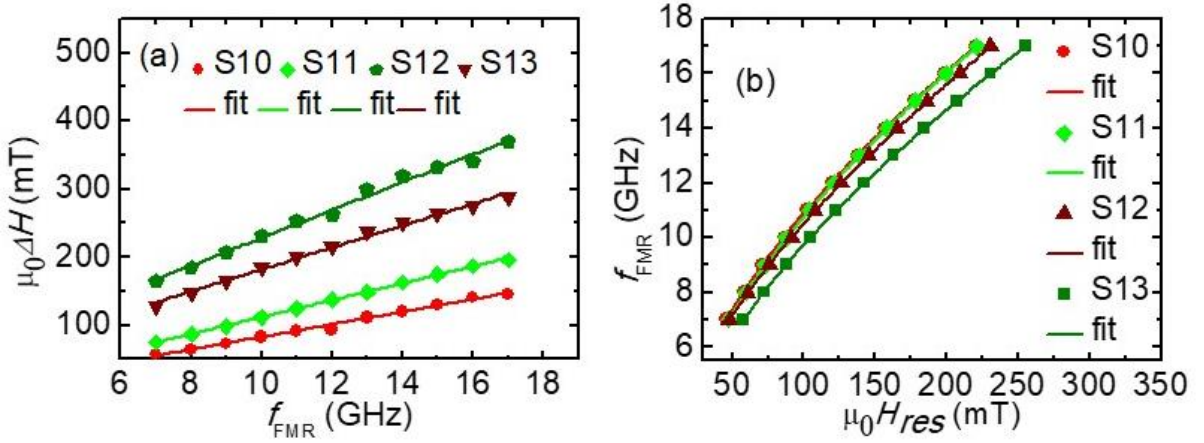


Figure 3.2.5: Represents the plot of (a) ΔH vs frequency (f) (b) H_{res} vs frequency (f) for all the samples.

The value of K_U is obtained from the relation $K_U = H_K M_S / 2$ where the value of H_K is the saturation field along HA and found from Kerr microscopy.

Figure 3.2.5 (a) shows the plot of ΔH vs frequency (f) and figure 3.2.5 (b) shows the plot of H_{res} vs frequency (f) for all the samples. From figure 3.2.5 (a), different ΔH values are found in all the magnetic samples. It is reported in literature that the ΔH value depends on the bilinear, biquadratic exchange coupling in a spin valve like structure and also on H_K ¹⁰³. However, in these samples the direct exchange coupling might be responsible for the tuning of ΔH value⁹⁶. Higher ΔH values have been found when CoFeB is at the bottom of magnetic bilayer. Thus,

one can tune the ΔH value by alternating the order and varying the thickness of magnetic layers. Similarly, the H_{res} is tuned in magnetic bilayers due to direct exchange coupling between magnetic layers.

It is found that S11 has higher α than sample S10. Similarly, sample S12 has higher α than sample S13. Thus, by increasing the thickness of Co from 5 nm to 10 nm and decreasing the thickness of CoFeB from 10 nm to 5 nm, an increase in interfacial exchange coupling is responsible for the enhancement of α value. Oblique angle deposition results into higher uniaxial magnetic anisotropy in all the bilayer samples⁹⁶. This may be a reason for the enhancement of α in all the magnetic bilayers. Ta is used as seed and capping layer which has high spin-orbit coupling. Therefore, spin pumping may be a reason for the enhancement of α ⁹⁶. Also, it is found that α value is high in magnetic bilayers where CoFeB is at the bottom. Thus, increase in interfacial exchange coupling by depositing CoFeB at the bottom of the magnetic bilayer results into higher α . It should be noted that the two-magnon scattering is not a mechanism here for the enhancement of α due to linear relationship of ΔH vs f at higher frequencies^{113,114}.

It is found that magnetic bilayers with higher value of ΔH_0 has higher α . Thus, ΔH_0 and α are related to each other. ΔH_0 is due to magnetic imperfections. Thus, magnetic bilayers with large magnetic imperfections have higher α .

All magnetic bilayers have g-factor greater than free electron value of 2. For a crystalline bilayer, the average value of orbital angular momentum is zero due to symmetry in crystal lattice but the orbital contribution of magnetic moment is non zero¹¹⁵. Therefore, g-factor follows the below relation which gives the value of g above 2.

$$g = 2\left(1 + \frac{\mu_L}{\mu_S}\right) \dots\dots\dots (3.2.2)$$

Samples S10 and S11 have higher $4\pi M_{eff}$ than the samples S12 and S13. Thus, $4\pi M_{eff}$ is higher

in the magnetic bilayers when Co layer is at the bottom. $4\pi M_{eff}$ and M_S do not follow the same relationship due to its direct relation with perpendicular surface anisotropy constant K_S . Due to high interfacial exchange coupling in samples S11 and S12, higher value of M_S is found in these samples. Negative value of K_S is found in samples S11 and S12 whereas positive values of K_S is found in samples S10 and S13.

3.2.5. Conclusions:

We have studied the magnetic properties by alternating the order and varying the thickness of magnetic layers.. For the bilayer samples, it is found that by depositing CoFeB (5 nm) at the bottom and Co (10 nm) at the top, coercivity gets enhanced by 0.7 mT. The magnetic property also changes by alternating the order of the layers. This is due to the increase in exchange coupling between Co and CoFeB. Also, the tuning of domain structure and damping constant α are found with this fabrication methodology.

Chapter 4: Effect of interfacial exchange coupling on static and dynamic magnetic properties.

4.1: Introduction:

Hard magnetic layers provide high coercive field (H_C) whereas soft magnetic layers give high saturation magnetization (M_S). The exchange coupled hard/soft magnetic bilayers give the H_C and M_S values higher than its constituent layers. As a result, soft/hard magnetic bilayers provide high energy product $(BH)_{\max}$ value which have the application in permanent magnets, magnetic devices etc.^{4,5,8-10}. For application in microwave devices, one needs to overcome the anisotropy⁷⁷. One of the method to overcome the growth induced magnetic anisotropy is the rotation of the substrate during deposition so that isotropic thin film is obtained⁷⁷. The study of tuning of magnetic anisotropy has utmost importance in fundamental understanding and also in application of data storage devices⁷⁷. Various methods to tune the magnetic anisotropy are oblique angle of deposition, deposition in magnetic field, magnetic annealing etc⁷⁷. In addition to static magnetic properties, materials with low Gilbert damping constant is necessary in the application of notch filters and materials with fast relaxation is required in the application of band-stop filters¹¹⁶. It is necessary to reduce the critical current for the application in spin transfer torque magnetic random access memory (STT-MRAM)¹¹⁷. However, the critical current is directly proportional to the damping constant α and effective uniaxial magnetic anisotropy $K_{U\text{eff}}$ ¹¹⁷. But, high uniaxial magnetic anisotropy is needed for thermal stability¹¹⁷. Therefore, one need to keep the low value of damping constant and at the same time high value of uniaxial magnetic anisotropy is desired. There are several methods to tune the Gilbert damping constant α . The damping constant can be enhanced by spin pumping in nonmagnetic (NM)/ ferromagnetic (FM) heterostructure¹⁰⁰. We can insert magnetic underlayers such as Co, NiFe, IrMn, NiMn etc. and/or nonmagnetic underlayers such as Ta, Pt, W etc. to tune the damping properties^{118,119}. It is reported that the modulation of damping

constant is possible by the construction of following systems such as permalloy (NiFe)/ heavy metal, magnetic insulator Yttrium iron garnet (YIG)/ permalloy (Py), FM/FM etc¹⁰⁰. One can do magnetic annealing and also annealing to tune the damping properties¹²⁰. Bilzer *et al.*, reported a very low Gilbert damping constant α of 0.006 in CoFeB and also the increment of damping by annealing which is due to crystallization⁹⁹. Thus, exchange bias effect and exchange coupling interactions can also modify α .¹¹⁶ It is reported by Wang *et al.*, that the strong exchange coupling between YIG and Py gives a higher value of α in the bilayer in comparison to YIG¹²¹. Tang *et al.*, reported the static and dynamic magnetic properties of CoFe by depositing in ultra-low gas pressure without doing magnetic annealing or depositing underlayers¹²⁰. Xu *et al.*, reported the tuning of dynamic magnetic properties of FeCoSiN by varying the deposition pressure¹²². Tuning of high frequency magnetic properties of FeCoN has been reported by varying deposition pressure¹²³. Deposition pressure develops inner (compressive or tensile) stress in thin film materials which affects the soft magnetic layer properties¹¹⁶. So, the inner stress is basically lattice stress. Seed layer also develops (compressive or tensile) stress which affects the magnetic properties¹²³. It is reported that the improvement of soft magnetic properties of FeCo is possible by depositing an underlayer due to modification in surface morphology and structure¹²⁴. It is believed that the structure and morphology improvement play an important role than the exchange coupling between FeCo and underlayer¹²⁵.

In this study, we have performed Kerr microscopy measurements to find the effect of interfacial exchange coupling on domain images and magnetic hysteresis loops. Ripple and labyrinth domains have been observed in magnetic bilayers⁷⁷ whereas ripple domains are observed only in single Co layer deposited in 50 sccm of Ar gas flow. So, we can conclude that interfacial exchange coupling in the magnetic bilayers might be a reason for the observation of ripple and labyrinth domains. It is also found the enhancement of anisotropy

energy (K_U) and coercive field (H_C) in magnetic bilayers than CoFeB layer due to interfacial exchange coupling. We found the tuning the Gilbert damping constant α and effective demagnetization field $4\pi M_{\text{eff}}$ by deposition pressure of the thin film.

4.2: Experimental details:

Co, Co₄₀Fe₄₀B₂₀ single layers and Co/Co₄₀Fe₄₀B₂₀ bilayers have been deposited by dc magnetron sputtering on Si (100) substrate. Ta of 1.5 nm thickness has been deposited as capping layer to avoid oxidation in all the samples. In some of the bilayers (samples 7 and 8), Ta of 3 nm thickness has been deposited as buffer layer. All the thin film systems have been fabricated at room temperature in an ultra-high vacuum (UHV) chamber manufactured by Mantis deposition Ltd., UK. The base pressure during the sample fabrication was better than $\sim 8 \times 10^{-8}$ mbar. The deposition was performed by keeping the throttle valve angle at 90° (completely open) and varying the Ar gas flow amount such as 10 and 50 sccm, respectively. The deposition pressure was $\sim 8 \times 10^{-4}$ and $\sim 3.3 \times 10^{-3}$ mbar during the Ar gas flow of 10 and 50 sccm, respectively. However, Ta was deposited in 20 sccm of Ar gas flow maintaining the deposition pressure of $\sim 1.5 \times 10^{-8}$ mbar. The rate of deposition of Ta, Co and Co₄₀Fe₄₀B₂₀ is 0.17 Å/sec. The substrate was rotated at 20 rpm speed during the deposition of Ta, Co and Co₄₀Fe₄₀B₂₀ thin film layers to avoid growth induced magnetic anisotropy developed due to oblique angle of deposition. Longitudinal magneto optic Kerr effect (LMOKE) based microscopy and magnetometry measurement is performed at room temperature to find magnetic domain images and hysteresis loops, respectively. Dynamic magnetic properties have been studied using ferromagnetic resonance (FMR) setup manufactured by Nano Osc. Saturation magnetization (M_S) values have been measured using superconducting quantum interference device (SQUID) based magnetometer manufactured by Quantum Design.

Sample name, structure, and Ar gas flow amount in sccm are given in table 4.1.

Table 4.1: Sample nomenclature, structure, and Ar gas flow amount in sccm. The numbers in

the brackets are in nm.

Sample name	Sample structure	Ar gas flow amount in sccm for Co and CoFeB deposition
Sample 1	Si/Co(5)/Ta(1.5)	10
Sample 2	Si/Co(5)/Ta(1.5)	50
Sample 3	Si/CoFeB(5)/Ta(1.5)	10
Sample 4	Si/CoFeB(5)/Ta(1.5)	50
Sample 5	Si/CoFeB(5)/Co(5)/Ta(1.5)	10
Sample 6	Si/CoFeB(5)/Co(5)/Ta(1.5)	50
Sample 7	Si/Ta/CoFeB(5)/Co(5)/Ta(1.5)	10
Sample 8	Si/Ta/CoFeB(5)/Co(5)/Ta(1.5)	50

4.3: Magnetization reversal, domain imaging and anisotropy energy:

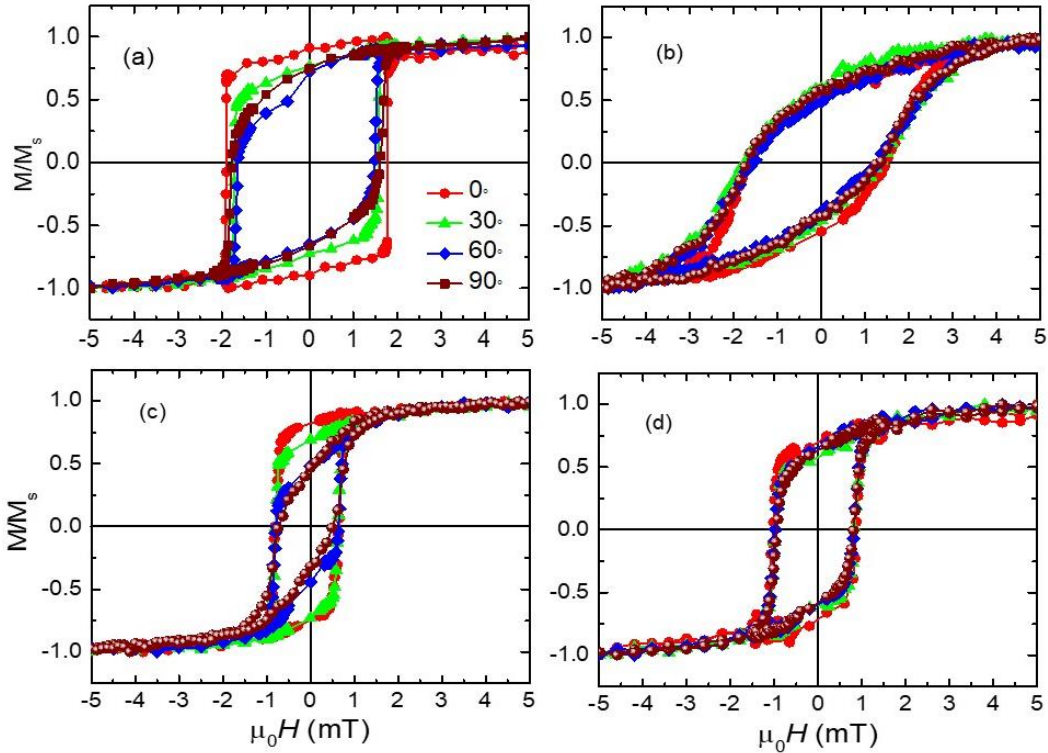


Figure 4.1: (a)-(d) the magnetic hysteresis loops measured using LMOKE at room temperature along $\phi = 0^\circ$ (red curve), 30° (green curve), 60° (blue curve) and 90° (wine curve) for the samples 1-4, respectively.

Magnetic hysteresis loops are measured using LMOKE based magnetometry for the samples 1-4 along $\phi = 0^\circ$, 30° , 60° , and 90° , respectively, which are shown in figure 4.1. In sample 1, the magnetization reversal is by domain wall motion along easy axis (EA) whereas the

magnetization reversal is combination of domain wall motion and partial rotation away from EA. A small change in squareness (M_r/M_s) and coercivity is found with increasing angle away from EA in sample 1. In sample 2, the magnetization reversal is by partial rotation along EA, 30° , 60° w.r.t. EA and hard axis (HA), respectively. No change is found in M_r/M_s and coercivity away from EA indicating that sample 2 is isotropic. In sample 3, the magnetization reversal is by domain wall motion along EA. Along 30° and 60° w.r.t. EA, the magnetization reversal is by domain wall motion and partial rotation whereas along HA, the magnetization reversal is by coherent rotation in sample 3. A change in M_r/M_s is found away from EA but

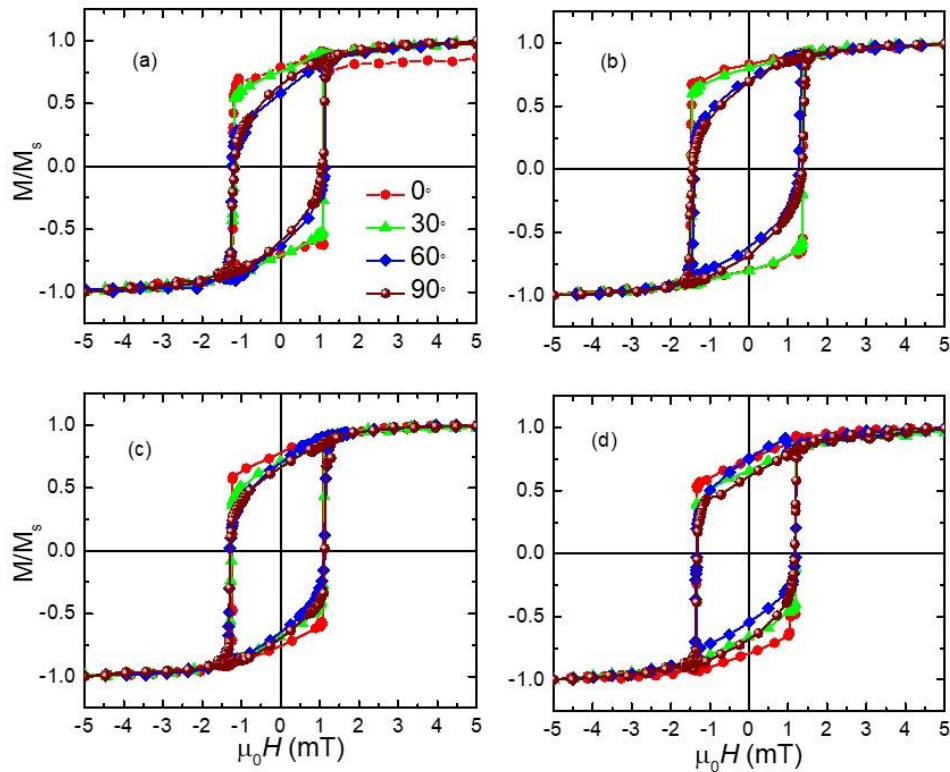


Figure 4.2: (a)-(d) the magnetic hysteresis loops measured using LMOKE at room temperature along $\phi = 0^\circ$ (red curve), 30° (green curve), 60° (blue curve) and 90° (wine curve) for the samples 5-8, respectively.

coercivity remains similar in sample 3. However, sample 4 is completely isotropic with similar M_r/M_s and coercivities along EA, 30° and 60° w.r.t. EA and HA. Magnetization reversal is by

domain wall motion and partial rotation along EA, 30 and 60° w.r.t. EA and HA in sample 4. Thus, it is found that the single layer magnetic samples (Co and CoFeB) becomes isotropic by increasing deposition pressure due to development of inner (compressive or tensile) stress in the materials. It is also found that the coercivity of CoFeB (sample 3 and 4) is less than Co (sample 1 and 2). Thus, Co is relatively harder than CoFeB. Previously, it has been reported that CoFeB is relatively hard than Co⁹⁶. In this study, rotation of the substrate at 20 rpm speed has been performed to overcome the growth induced magnetic anisotropy. By rotating the substrate, the modification of microstructure might be a reason for relative hardness of Co in comparison to CoFeB.

Magnetic hysteresis loops are measured by LMOKE based magnetometry for the samples 5-8 along $\phi = 0^\circ, 30^\circ, 60^\circ, \text{ and } 90^\circ$, respectively which are shown in figure 4.2. In bilayer samples, there is a small change in squareness (M_r/M_s) away from EA. Thus, in these magnetic bilayers, deposition pressure and Ta seed layer have no effect on the anisotropy nature. Therefore, small change in M_r/M_s is found in these bilayers whereas coercivity values remain similar. Co is deposited on top of CoFeB which results into the modification of microstructure of Co and also interfacial exchange coupling. These might be the reasons for the small change in M_r/M_s away from EA in magnetic bilayers although isotropic films are found by depositing single magnetic layers in 50 sccm of Ar gas flow. The coercive field (H_C) of magnetic bilayers is higher than the single CoFeB magnetic layer and less than single Co magnetic layer indicating the hardness of Co might be a reason for the enhancement of H_C in the magnetic bilayers. The deposition of Ta seed layer in the magnetic bilayer has no effect on H_C . All the magnetic bilayers are inverted films as the H_C and anisotropy field H_K are equal. Due to rotation of the substrate during deposition, less H_C and H_K values are observed in all the samples. High H_C value has been reported in some of our studies for the single magnetic layers deposited in 0 rpm substrate speed¹²⁶.

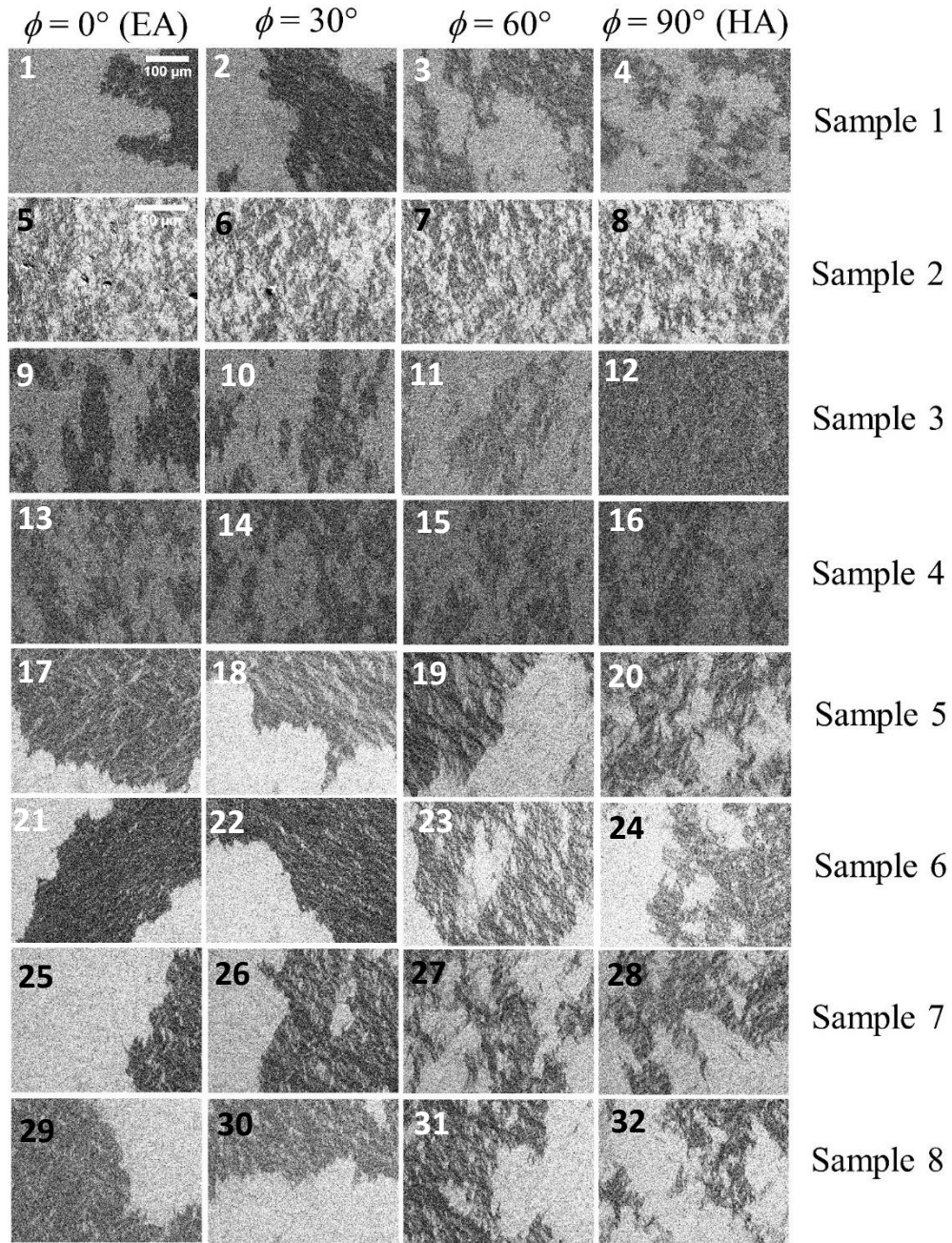


Figure 4.3: Magnetic domain images of samples 1-8 recorded using LMOKE based microscopy along $\phi = 0^\circ$, 30° , 60° and 90° , respectively. Domain images of sample 2 is recorded using 50X objective whereas 20 X objective is used for all other samples.

Figure 4.3 shows the magnetic domain images of all samples along $\phi = 0^\circ$ (EA), 30° , 60° and 90° (HA), respectively. In sample 1, big branch domains are found along EA whereas branch and patch like domains are found along 30° , 60° and 90° w.r.t. EA, respectively. In sample 2,

small ripple domains are found along EA, 30, 60 and 90° w.r.t. EA. In sample 3, branch and patch like domains are found along EA, 30 and 60° w.r.t. EA, respectively. In sample 3, along HA, the reversal is found by coherent rotation without any magnetic domains. In sample 4, patch like domains are found along $\phi = 0^\circ, 30^\circ, 60^\circ$ and 90° . Thus, by varying the deposition pressure one can tune the domain structure. In the magnetic bilayers, we found the presence of ripple and labyrinth domains due to the dispersion in local grain anisotropy⁷⁷. Thus, the interfacial exchange coupling between Co and CoFeB and also the structure modification of Co by depositing on top of CoFeB might be the reasons for presence of the ripple and labyrinth domains. In sample 5, the presence of big branch domains and small ripple domains are found along EA. In sample 5, labyrinth and big branch domains are found along 30 and 60° w.r.t. EA due to anisotropy dispersion whereas labyrinth and patch like domains are found along HA⁷⁷. The small ripple or labyrinth domains, that are nucleated, are always present during the magnetization reversal and due to domain wall motion, big branch domains are also present along EA, 30 and 60° w.r.t. EA in sample 5. In sample 6, big branch domains and ripple domains are found along EA and 30° w.r.t. EA whereas labyrinth and branch domains are found along 60° w.r.t. EA. Big branch and patch like domains are found along HA in sample 6. It is found that by putting Ta as seed layer in the magnetic bilayers (samples 7 and 8), no change in domain structure is observed whereas there was a change in samples 5 and 6 by varying the deposition pressure. In sample 5, due to high anisotropy dispersion, magnetic domains near remanence are found⁷⁷ whereas magnetic domains are observed near nucleation in sample 6 along EA, 30 and 60 and 90° w.r.t. EA. Thus, magnetic domains near remanence are observed in sample 5 by depositing this bilayer in low deposition pressure ($\sim 8 \times 10^{-4}$ mbar). The anisotropy field (H_K) is the saturation field along HA which can be obtained from Kerr microscopy measurements. The saturation magnetization (M_S) is obtained from SQUID magnetometer. The anisotropy energy is calculated by using the relation $K_U = \frac{H_K M_S}{2}$. M_S value

is found to decrease with increase in the Ar gas flow amount from 10 to 50 sccm. The results indicate that the anisotropy energy of Co is higher than CoFeB. Due to direct exchange coupling between Co and CoFeB, higher anisotropy energy in the magnetic bilayers is found than the CoFeB single magnetic layer⁹⁶. However, depositing Ta as seed layer in samples 7 and 8, similar values of M_S has been found. In the magnetic bilayers, the magnetization values are intermediate of Co and CoFeB. Thus, the direct exchange coupling of Co and CoFeB magnetic layers may be responsible for the enhancement of M_S in the magnetic bilayers.

Table 4.2: Sample name, H_C along EA, H_K in mT, saturation magnetization (M_S) in emu/cc and anisotropy energy (K_U) in J/m³ for all the samples.

Sample name	H_C along EA in mT	H_K in mT	M_S (emu/cc)	$K_U \times 10^3$ (J/m ³)
Sample 1	1.839±0.007	1.85±0.50	1698.08±0.86	1.57±0.68
Sample 2	1.575±0.073	4.00±0.13	1441.16±0.56	2.88±0.35
Sample 3	0.724±0.027	1.70±0.13	844.82±0.57	0.72±0.35
Sample 4	0.942±0.032	2.00±0.39	740.33±0.51	0.74±0.45
Sample 5	1.154±0.003	1.60±0.60	1220.32±0.51	0.98±0.55
Sample 6	1.434±0.010	1.70±0.71	1140.39±0.42	0.97±0.57
Sample 7	1.152±0.004	1.90±0.52	1224.26±0.39	1.16±0.45
Sample 8	1.266±0.009	1.80±0.48	1250.78±0.44	1.12±0.46

4.4: Damping properties study:

Figure 4.4 shows the FMR frequency (f_{FMR}) vs H_{res} and line width (ΔH), respectively. The effective demagnetization field ($4\pi M_{eff}$), effective anisotropy field (H_K) and the gyromagnetic ratio $\gamma = \frac{g\mu_B}{\hbar}$ values have been extracted by fitting experimental data (Fig. 4.4

(a)) using the following Kittel equation⁶²:

$$f_{FMR} = \frac{\gamma}{2\pi} \sqrt{(4\pi M_{eff} + H_{res} + H_K)(H_{res} + H_K)} \quad \dots\dots\dots (4.1)$$

Similarly, the Gilbert damping constant value α is obtained by fitting the line width (ΔH) versus f_{FMR} (Fig. 4.4(b)) using the following equation;

$$\Delta H = \Delta H_0 + \frac{4\pi\alpha f_{FMR}}{\gamma} \quad \dots\dots\dots (4.2)$$

Where, ΔH_0 is the inhomogeneous linewidth broadening.

The effective demagnetization field ($4\pi M_{eff}$) is not equal to saturation magnetization ($4\pi M_S$) due to the below relation;

$$4\pi M_{eff} = 4\pi M_S + \frac{2K_S}{M_S t_{FM}} \dots\dots\dots (4.3)$$

Where, K_S is perpendicular surface anisotropy constant and t_{FM} is the ferromagnetic layer thickness.

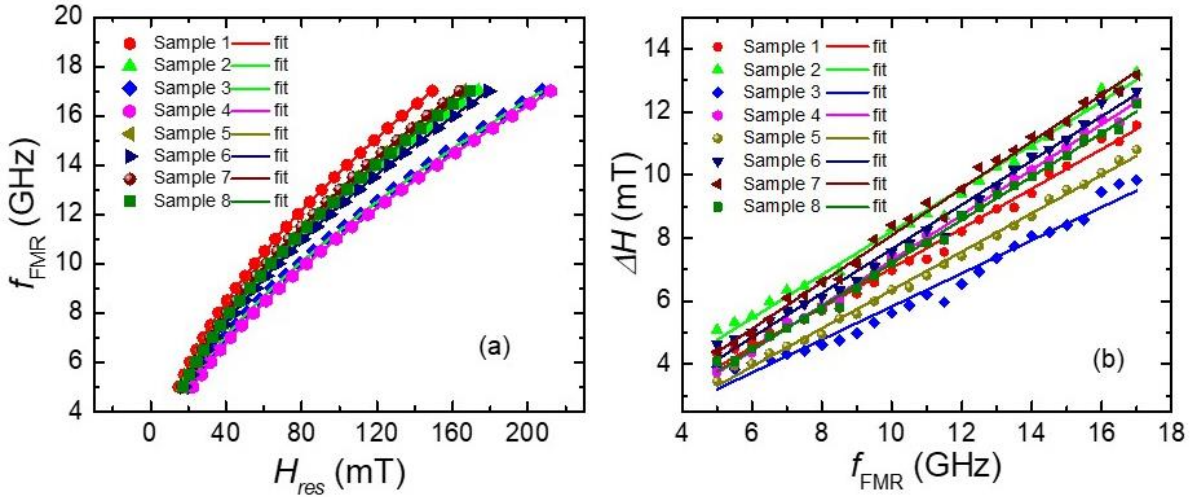


Figure 4.4: (a) Resonance field (H_{res}) vs f_{FMR} and (b) linewidth (ΔH) vs f_{FMR} plots for all the samples.

α of samples 1 and 3 are found to be 0.0105 ± 0.0002 and 0.0086 ± 0.0003 , respectively,, which are deposited in 10 sccm of Ar gas flow. The presence of higher uniaxial magnetic anisotropy¹²⁷ in sample 1 might be a reason for the higher value of α in comparison to sample 2. Sample 1 has higher α than sample 2 and sample 4 has higher α than sample 3. Thus, by increasing the deposition pressure from 10 to 50 sccm, the damping constant is getting enhanced. This is due to increase in deposition pressure which generates inner (compressive or tensile) stress in thin films and that enhances the Gilbert damping constant α ¹¹⁶. It is reported in literature that the increase in deposition pressure enhances damping constant α ¹²⁰. In sample 5, by depositing CoFeB as underlayer of Co, the damping constant α is higher than CoFeB but

similar to Co. Thus, direct exchange coupling between magnetic Co and CoFeB magnetic layers in the sample 5 might be a reason for the enhancement of damping constant α ¹²¹.

Table 4.3: Details of extracted values of α , ΔH_0 , g-factor, $4\pi M_{\text{eff}}$, H_{Keff} and K_S obtained by fitting eq. (4.1), (4.2) and (4.3).

Sample name	α	ΔH_0 (mT)	g-factor	$4\pi M_{\text{eff}}$ (mT)	H_{Keff} (mT)	K_S (erg/cm ²)
Sample 1	0.0105±0.0002	0.76 ± 0.16	2.39 ± 0.02	1578.88± 32.99	-0.90±0.04	-0.188±0.011
Sample 2	0.0119±0.0002	1.34 ± 0.14	2.49 ± 0.02	1197.53± 26.21	-0.44±0.08	-0.175±0.007
Sample 3	0.0086±0.0003	0.58 ± 0.20	2.34±0.008	1075.86± 8.87	1.47±0.05	0.003±0.001
Sample 4	0.0120±0.0001	0.12 ± 0.09	2.40 ± 0.01	997.88± 14.39	-0.73±0.09	0.010±0.002
Sample 5	0.0102±0.0001	0.27 ± 0.09	2.40 ± 0.02	1402.77± 26.64	-1.29±0.05	-0.062±0.012
Sample 6	0.0116±0.0002	0.64 ± 0.18	2.38 ± 0.01	1276.05± 19.58	-0.78±0.05	-0.071±0.009
Sample 7	0.0125±0.0002	0.67 ± 0.14	2.41 ± 0.03	1391.63± 42.48	-1.42±0.08	-0.071±0.020
Sample 8	0.0119±0.0001	0.33 ± 0.10	2.47 ± 0.01	1259.66± 20.66	-0.99±0.05	-0.154±0.010

However, sample 6 has the damping constant α of 0.0116± 0.0002 similar to Co and CoFeB prepared in 50 sccm of Ar gas flow. This is due to the variation in exchange coupling between Co and CoFeB in sample 5 and 6 deposited in dissimilar deposition pressure. In sample 7, by putting Ta as underlayer due to extrinsic contribution of damping such as spin pumping, α is getting enhanced¹²³. However, sample 8 (deposited in 50 sccm of Ar flow) has α value similar to sample 7 (deposited in 10 sccm of Ar flow). Thus, Ta underlayer has no effect on α in sample 8 and this may be due to variation of exchange coupling between Co and CoFeB layers developed by increasing deposition pressure. Above all, spin pumping might be responsible for the enhancement of damping constant α as Ta of 1.5 nm is deposited as capping layer in all the magnetic samples and also as seed layer (samples 7 and 8) which is a high spin-orbit

coupling material¹²⁸.

During gyromagnetic precession, the orbital motion of electrons is quenched by the crystal field which is observed in a symmetric crystal lattice. Thus, the orbital angular momentum is zero but the orbital contribution to the magnetic moment is non-zero giving rise to the value of g always greater than 2.

In this case the g-factor follows the relation below¹²⁹;

$$g = 2\left(1 + \frac{\mu_L}{\mu_S}\right) \dots\dots\dots (4.4)$$

In this study, all the samples have g-factor greater than 2. Thus, orbital contribution of magnetic moment is higher in all the samples. It is found that in magnetic single layers, the g-factor increases with increase in sputtering pressure. In the bilayer samples 5 and 6, the g-factor is almost similar. By putting Ta as underlayer, in samples 7 and 8, g-factor increases with increase in sputtering pressure. It should be noted that P. Neilinger et al., have also reported large values of g-factor in Pt/Co/Pt multilayers¹³⁰. In their case, the g-factor values are in the range of 2.35 to 2.46¹³⁰.

In this study, it is observed that M_S value increases with decrease in deposition pressure. Similarly, $4\pi M_{\text{eff}}$ values are also increasing with the decrease in deposition pressure in all the sample. Thus, the tuning of magnetization can be achieved by deposition pressure. The magnitude of effective anisotropy field H_{Keff} obtained from FMR method are small values. This is due to the rotation of the substrate at 20 rpm speed during deposition which overcomes the growth induced magnetic anisotropy. The reduction of H_{Keff} is observed with increase in sputtering pressure. Thus, deposition pressure has significant effect on H_{Keff} .

The positive value of perpendicular surface anisotropy constant K_S is found in samples 3 and 4 whereas all other samples have negative value of K_S . The tuning of K_S is observed by deposition pressure.

4.5: Conclusions:

All the magnetic samples are deposited by dc magnetron sputtering on Si (100) substrate. The different deposition methodologies such as rotating the substrate at 20 rpm speed and varying the deposition pressure are used during deposition. Magnetic single layers and bilayers (except samples 7 and 8) have been deposited on Si (100) substrate without any buffer layer. Similar coercivity values are observed in all the magnetic sample away from EA whereas variation in M_r/M_S values are found away from EA in some samples. Due to anisotropy dispersion, ripple and labyrinth domains are found in the magnetic bilayers. Near remanence, magnetic domains are found in sample 5 due to high anisotropy dispersion. It is found that Co is relatively hard than CoFeB. The magnetic hardness of Co, in comparison to CoFeB, is due to the change in microstructure generated by substrate rotation. Due to exchange coupling between Co and CoFeB in the magnetic bilayers, the enhancement of H_C and M_S is observed in comparison to the single CoFeB magnetic layer. A very low value of α of 0.0086 is evaluated in CoFeB single layer deposited in 10 sccm of Ar gas flow due to its lower uniaxial magnetic anisotropy. The tuning of α is possible by the deposition pressure, presence of direct exchange coupling in the magnetic bilayers etc. Tuning of g-factor, $H_{K\text{eff}}$ and $4\pi M_{\text{eff}}$ is found by deposition pressure due to development of inner (compressive or tensile) stress in the magnetic thin films.

Chapter 5: Effect of interfaces on magnetic properties in Fe/NiFe bilayers of alternating order.

5.1: Introduction:

It is well known that materials with large magnetic anisotropy (K_U), coercive field (H_C), magnetization (M_S) have several technological applications^{4,5,8-10,82}. Various deposition methodologies have been employed to optimize the energy product value. It is reported in literature that controlling of the microstructure of the soft layer by post deposition annealing is necessary to optimize the exchange coupling between the hard and soft magnetic layers⁶. Materials such as crystallographically textured grown nanocomposites provide high energy product $(BH)_{max}$ value⁷. By depositing an optimum thickness of Cu in-between Sm-Co and Fe, an increase in coercivity is found which enhances the energy product $(BH)_{max}$ value⁷. Also, interfacial conditions affect the exchange coupling among the soft and hard magnetic layers⁷. Literature study reveals that a graded interface is more helpful than the sharp interfaces which results into the increase of the nucleation field of the soft phase and decreases the switching field of the hard phase¹¹³. It is provided in literature that by adding an artificially intermixed layer of structure Cr (20 nm)/Sm-Co (20 nm)/Sm-Co-Fe (t_{mix})/Fe (20 nm- t_{mix})/Cr (5nm) enhances the effective exchange coupling and thereby the energy product value is increased¹³¹. Si *et al.* reported the deterioration of coercivity due to atomic diffusion using OOMMF¹³². To prevent atomic diffusion, Cui *et al.* deposited Ta layer in-between Nd_2Fe_4B and FeCo for achieving high coercivity¹³². High temperature annealing results into large change in the magnetic properties of hard (CoPt)/soft (Co) bilayer due to interdiffusion¹³³. It is also found that postannealing can lead to diffusion in FeAu/FePt system¹³⁴. Increase in coercivity is found using OOMMF in $Nd_2Fe_{14}B/\alpha''-(FeCo)_{16}N_2$ bilayers by inserting nonmagnetic spacer layer

due to its diffusion effect¹³⁵. The reduction of coercivity by increasing the soft layer thickness in FePt (hard)/Fe (soft) bilayer is not only due to increase in exchange coupling but also due to diffusion¹³⁶. Navas *et al.* reported that the deviation of magnetization value obtained from polarized neutron reflectivity (PNR) from its saturation magnetization (obtained from M-H measurements), is due to large lattice mismatch and interdiffusion¹³⁷. It is found from PNR that the interfacial exchange coupling is proportional to the interface area and is significant at remanence also¹³⁷. From PNR, uniform direction of magnetic moment is found in CoPt soft and hard layers whereas the interface between them is divided into various layers with the formation of interfacial domain wall¹³⁸. Also from PNR, the formation of multidomain state of the magnetic layers is found due to the discrepancy of the fitted (from PNR) and saturated magnetizations¹³⁸. The presence of interfacial diffusion is found in hard (FePt)/soft (Fe and Co/Fe) multilayers by Conversion Electron Mössbauer Spectroscopy (CEMS)¹³⁹. Electron microscopy and synchrotron X-ray scattering has confirmed interfacial mixing in high temperature deposited epitaxial Sm-Co/Fe bilayers¹⁴⁰. Depth and element resolved X-ray resonant magnetic scattering (XRMS) measurements provide the evidence of diffusion of Co into Fe in Sm-Co/Fe bilayers¹⁴¹.

In this study, the influence of the interface on the magnetic properties is reported by alternating order of magnetic layer. Different values of interdiffusion layer thickness and magnetic moment are observed by the polarized neutron reflectivity (PNR) method. Static and dynamic magnetic properties have also been studied in these samples.

5.2: Experimental details:

All the magnetic layers are deposited by dc magnetron sputtering on Si (100) substrate, which are shown in Table 5.1. A 3 nm thick Au layer was deposited by using e-beam evaporation to

avoid oxidation. The substrate is annealed before deposition for 2 hours at temperature of 150 °C. Then, the deposition of the magnetic and the capping layers were performed at 150 °C. The base pressure for the sample's fabrication was $\sim 6 \times 10^{-8}$ mbar. The Ar working pressure for dc sputtering was kept at $\sim 5 \times 10^{-3}$ mbar. The deposition pressure during e-beam evaporation of Au was $\sim 5.0 \times 10^{-7}$ mbar. The rate of deposition of Fe, NiFe and Au are kept at 0.22, 0.17 and 0.1 Å/sec, respectively. Polarized neutron reflectivity (PNR) experiment was performed at room temperature using POLREF neutron reflectometer at Rutherford Appleton Laboratory, UK. The magnetic field was applied along EA and the PNR measurement was performed at saturation and near to coercive field of the bilayer samples. In this PNR measurement, the wavelength of the neutron beam λ is kept fixed and the angle of incidence (same as angle of reflection) θ is varied. We plot the neutron reflectivity vs perpendicular scattering vector $Q_Z = 4\pi \sin\theta/\lambda$. Q_Z is the component of momentum transfer which is perpendicular to the sample surface thus giving sample's layer by layer information^{142,143}. Q_Z is the variable conjugate of depth d from the sample surface therefore structural and magnetic information is found for different layers of the sample^{142,143}. Two scattering cross sections namely R^{++} and R^{--} were measured where the neutron magnetic moment interacts with sample magnetization which is placed in a magnetic field^{142,143}. In the scattering cross section R^{++} (up-up), the first + sign is for the up spin polarization of incident neutron beam and second + sign is for up spin polarization of reflected neutron beam after interacting with the sample surface. Similarly, for the scattering cross section R^{--} (down-down). This scattering cross sections are termed as non-spin flip (NSF) scattering cross section. Dynamic magnetic properties are studied using ferromagnetic resonance (FMR) setup developed by Nano Osc. X-ray reflectivity (XRR) measurements were performed to find the thickness and roughness of each individual layers by using X-ray diffractometer from Rigaku with $\text{CuK}\alpha$ radiation. The data were fitted using GenX software¹⁴⁴.

Table 5.1: Details of sample structure.

Sample name	Sample structure
Sample A	Si (100)/NiFe (10 nm)/Au (3 nm)
Sample B	Si (100)/Fe (5 nm)/Au (3 nm)
Sample C	Si (100)/Fe (5 nm)/NiFe (10 nm)/Au (3 nm)
Sample D	Si (100)/NiFe (10 nm)/Fe (5 nm)/Au (3 nm)

5.3: Structural properties:

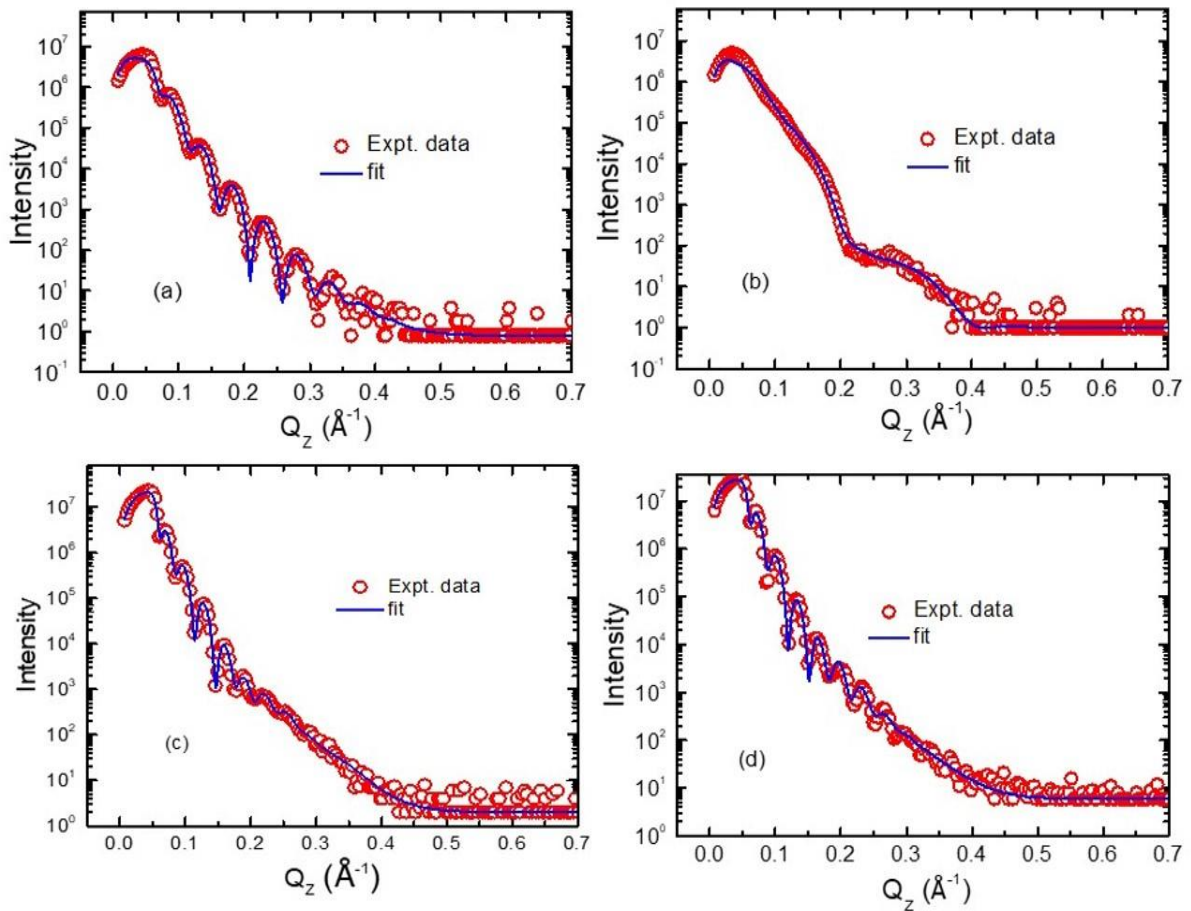


Figure 5.1: (a)-(d) show the XRR experimental data (red open circles) along with the fitted GenX simulated patterns (blue solid line) of samples A-D, respectively.

From the XRR measurements, thickness, density and roughness of all the thin film layers are evaluated. It is concluded from the XRR data (table 5.2) that the roughness of NiFe and Fe is more in sample D than C. Figure 5.1 represents the XRR experimental data (open circles) and its best fit (solid line) of the samples A-D, respectively.

Table 5.2: Shows the structural parameters such as thickness, roughness obtained from X-ray reflectivity (XRR) data fitting using Genx software. Here, D and σ denote the thickness and roughness of thin film layers.

aSample name	Au-D	NiFe-D	Fe-D	Au- σ	NiFe- σ	Fe- σ
Sample A	3.26	9.27	-	0.84	1.71	-
Sample B	2.99	-	3.61	0.85	-	0.60
Sample C	3.66	9.98	4.99	1.24	1.05	0.76
Sample D	3.94	9.42	4.51	1.11	1.60	1.08

5.4: Magnetic hysteresis loops and domain images:

Magnetic hysteresis loops are measured by LMOKE based magnetometry for all the samples along $\phi = 0^\circ, 30^\circ, 60^\circ,$ and 90° , respectively, which are shown in figure 5.2. Square shaped

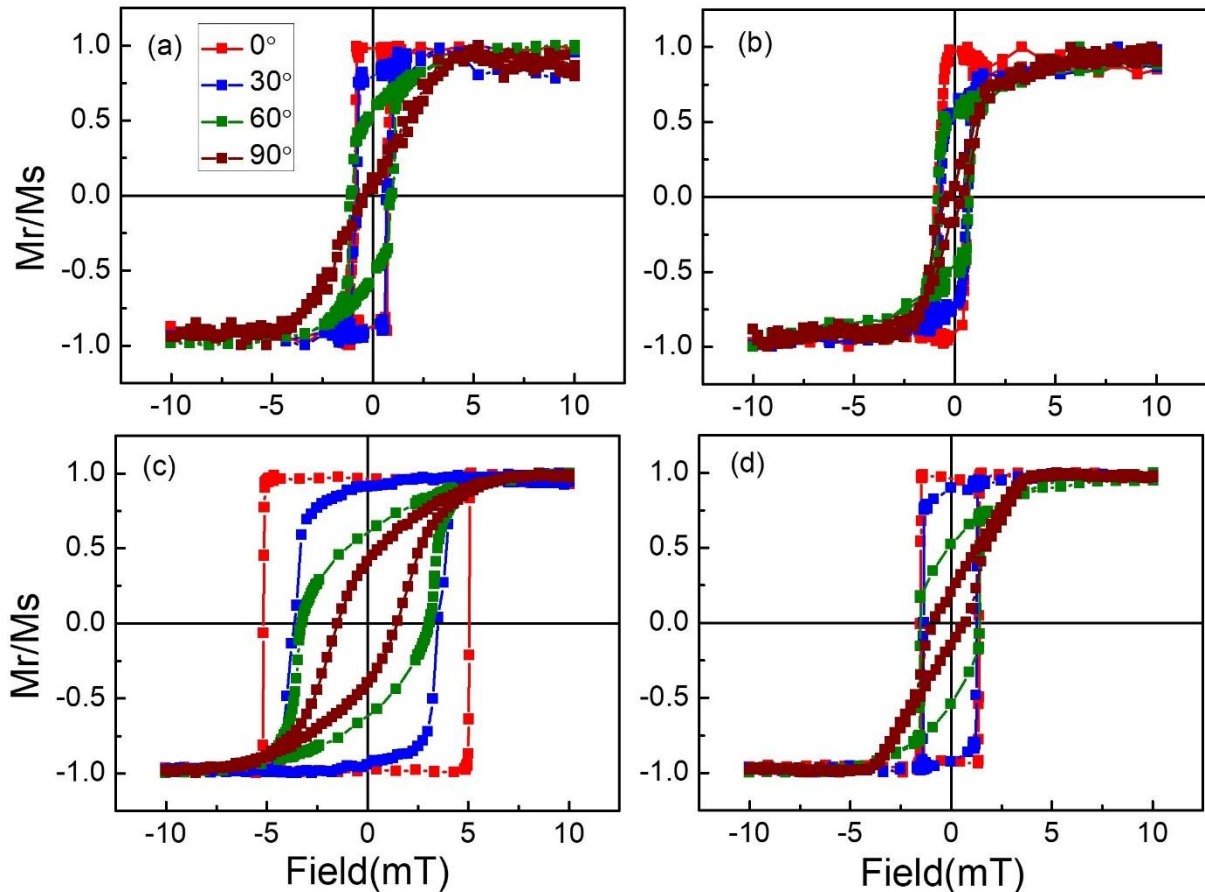


Figure 5.2: (a)-(d) magnetic hysteresis loops measured by LMOKE at room temperature along $\phi = 0^\circ, 30^\circ, 60^\circ,$ and 90° for samples A-D.

loops are found along easy axis (EA) and s-shaped loops are found along hard axis (HA). Thus, the magnetization reversal likely occurs through domain wall motion along the EA and by coherent rotation along the HA. This also indicates the presence of uniaxial magnetic anisotropy in all the samples.

Table 5.3. H_C along EA and HA and H_K for all the samples.

Sample name	H_C (EA) (mT)	H_C (HA) (mT)	H_K (mT)
Sample A	0.80	0.38	4.28
Sample B	0.74	0.32	2.44
Sample C	5.10	1.47	7.10
Sample D	1.45	0.79	4.00

Table 5.3 shows the list of sample names, their H_C along EA and HA and H_K values, respectively. The anisotropy field H_K is the saturation field along HA which is obtained from Kerr microscopy. The H_C values of samples A and B are nearly equal to each other whereas the H_K value of sample A is higher than sample B. But, the thickness of sample A is twice than sample B. The H_C and H_K values of sample C are much higher than other samples. This indicates that exchange coupling among the individual layers may be the possible reason for the enhancement of the H_C and H_K values¹¹¹. Again, by interchanging the order of magnetic layers a large change in H_C is observed.

Figure 5.3 shows the magnetic domain images of sample A ((a)-(d)), sample B ((e)-(h)), sample C ((i)-(l)), and sample D ((m)-(p)) along $\phi = 0^\circ$ (EA), 30° , 60° and 90° (HA), respectively. Big branch domains are observed along EA in all the samples. Big domains are found away from EA in samples A, B, and D due to anisotropy inhomogeneity. However, small domains are found away from EA in sample C due to high uniaxial magnetic anisotropy. The absence of magnetic domains along HA indicates that the magnetization reversal occurs through coherent rotation.

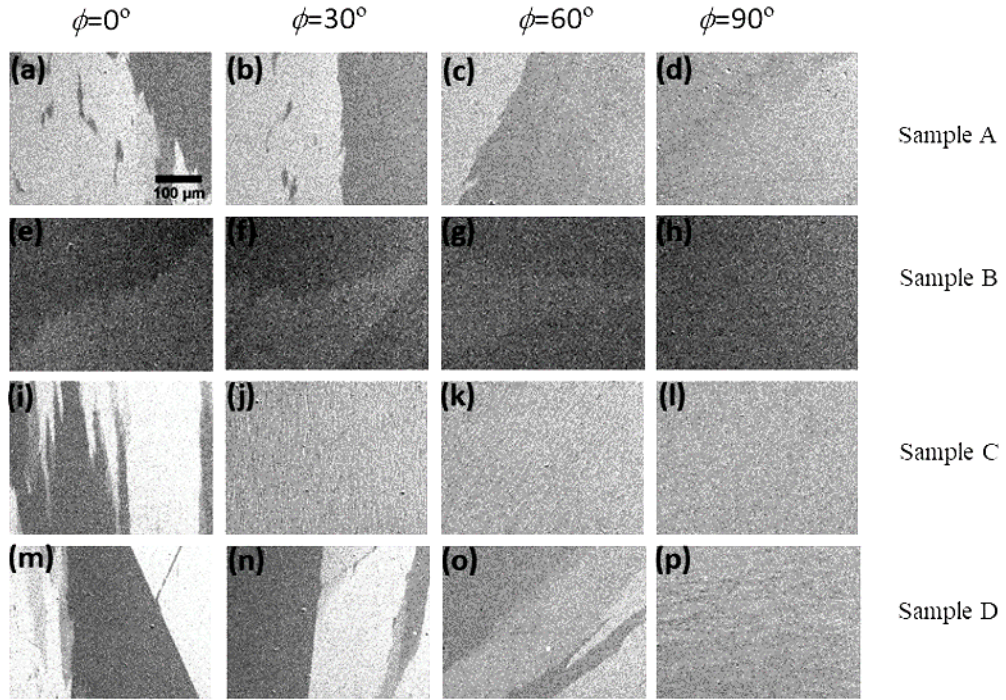


Figure 5.3: Magnetic domain images of sample A-D along $\phi=0^\circ$ (EA), 30° , 60° and 90° (HA) recorded in LMOKE based microscopy at room temperature.

5.5: Dynamic magnetic properties:

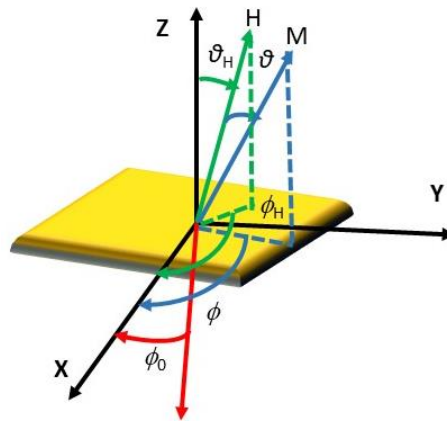


Figure 5.4: A schematic of the directions of magnetization M , applied field H and EA wrt the sample plane which are used for FMR angle dependent study.

The resonance magnetic field (H_{res}) is measured by varying the in-plane angle ϕ with an interval of 10° . In-plane angle dependent study is performed and therefore the out of plane magnetic field H direction θ_H and magnetization M direction θ wrt z axis are equal to zero.

The magnetic free energy density can be written as^{112,145};

$$E = HM_S[\sin \theta_H \sin \theta \cos(\varphi - \varphi_H) + \cos \theta_H \cos \theta] - 2\pi M_S^2 \sin^2 \theta + K_P \sin^2 \theta + K_{in} \sin^2 \theta \sin^2(\varphi - \varphi_0) \dots \dots \dots (5.1)$$

Where, K_P is the perpendicular uniaxial anisotropy constant, K_{in} is the in-plane two-fold uniaxial anisotropy constant. θ_H and θ are the angles of applied magnetic field H and saturation magnetization M_S wrt z-axis, respectively. φ_H is the angle of projection of M_S in x-y plane wrt x-axis. φ is the angle of the projection of H in the x-y plane wrt x-axis. φ_0 is the two-fold EA direction wrt the x-axis. The directions of M_S , H and the two-fold EA direction φ_0 are given in figure 5.4.

The angle dependent H_{res} fields are fitted with the following dispersion relation to obtain the value of H_K and h_u ¹¹².

$$\left(\frac{\omega}{\gamma}\right)^2 = [H_{res} \cos(\varphi - \varphi_H) - h_u + H_K \sin^2(\varphi - \varphi_0)] [H_{res} \cos(\varphi - \varphi_H) + H_K + 2H_K \sin^2(\varphi - \varphi_0)] \dots \dots \dots (5.2)$$

Where, $h_u = \frac{2K_P}{M_S} - 4\pi M_S$ and $H_K = 2K_{in}/M_S$.

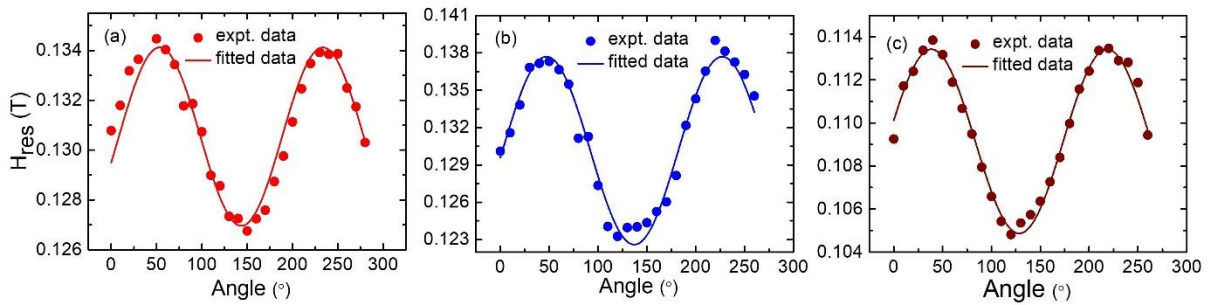


Figure 5.5: (a)-(c) the plot of resonance magnetic field (H_{res}) vs in-plane angle φ for samples A, C and D, respectively. Solid symbols are the experimental data while solid lines are the best fit using equation (5.2).

In-plane angle dependent FMR measurements are performed at a fixed frequency of 9 GHz. Uniaxial magnetic anisotropy is found in all the magnetic samples, which may be due to

oblique angle of deposition. The plots of H_{res} vs φ are shown in figure 5.5. The solid symbols are the experimental data and the solid line is the fitted data.

The evaluated values of H_K by fitting experimental data to the equation (5.2) (Fig. 5.5) for samples A, C and D are 0.0036 T, 0.0082 T and 0.0041 T, respectively.

Figure 5.6 shows the FMR frequency (f_{FMR}) vs H_{res} and line width (ΔH), respectively. The effective demagnetization field ($4\pi M_{eff}$), effective anisotropy field (H_{Keff}) and the gyromagnetic ratio $\gamma = \frac{g\mu_B}{\hbar}$ values have been extracted by fitting experimental data (Fig. 5.6 (a)) using the following Kittel equation⁶²:

$$f_{FMR} = \frac{\gamma}{2\pi} \sqrt{(4\pi M_{eff} + H_{res} + H_K)(H_{res} + H_K)} \quad \dots\dots\dots (5.3)$$

Similarly, the Gilbert damping constant value α is obtained by fitting the line width (ΔH) versus f_{FMR} (Fig. 5.6(b)) using the following equation;

$$\Delta H = \Delta H_0 + \frac{4\pi\alpha f_{FMR}}{\gamma} \quad \dots\dots\dots (5.4)$$

Where, ΔH_0 is the inhomogeneous linewidth broadening.

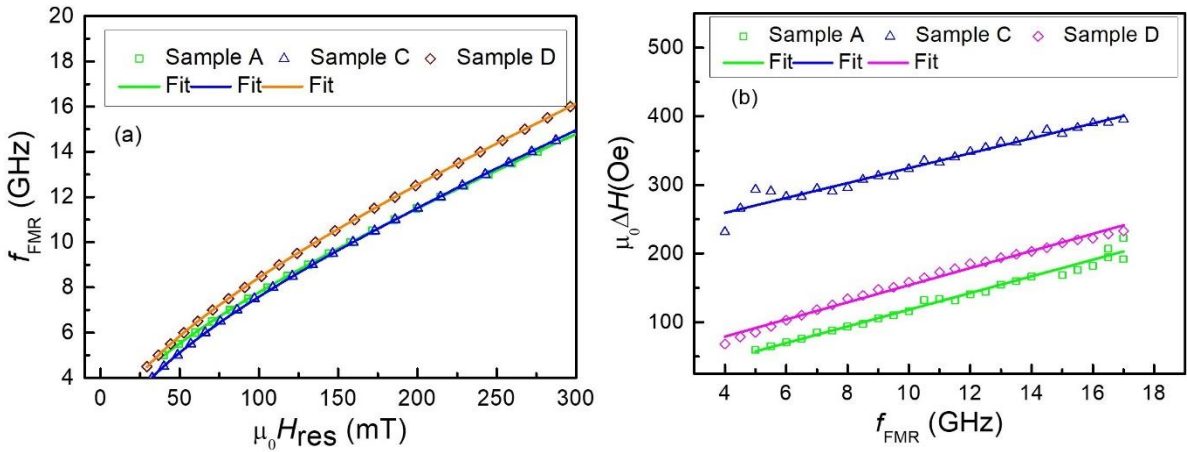


Figure 5.6: (a) H_{res} , (b) ΔH versus f_{FMR} plot for the samples A, C and D.

It is noted here that FMR spectra could not be recorded of sample B due to the large linewidth broadening. Therefore, the H_{res} and ΔH values have not been extracted for the sample B. As discussed previously, due to direct exchange coupling between the two ferromagnetic layers

the H_{res} value is just higher in sample D than sample A. It is found from literature theoretically that the ΔH value also depends on the anisotropy field H_K and the interlayer coupling strength of two ferromagnetic layers separated by a non-magnetic layer¹⁰³. Therefore, due to difference of magnetic coupling at the interface of samples C and D, we have obtained a difference value of ΔH . The ΔH value of the magnetic bilayer is higher than the single layer sample A.

Previously it has been reported that due to direct exchange coupling between Co and CoFeB magnetic layers an increase in the α value is observed⁹⁶. However, in this study, α value in the magnetic bilayers is similar to the single layer sample A. It is good for application due to high H_C and less α in these bilayers.

Table 5.4. List of values of the magnetic parameters g , $4\pi M_{eff}$, H_{Keff} , α , ΔH_0 obtained from the fitting of equations 5.3 and 5.4, perpendicular surface anisotropy constant K_S found from eq. 5.7, and saturation magnetization M_S for all the samples.

Sample name	g	$\mu_0 4\pi M_{eff}$ (mT)	$\mu_0 H_{Keff}$ (mT)	α	$\mu_0 \Delta H_0$ (mT)	M_S (emu/cc)	K_S (erg/cm ²)
Sample A	1.956±0.007	636.25±8.69	8.44±0.34	0.0160±0.0005	0.31±0.41	639	-0.042±0.002
Sample B	-	-	-	-	-	860	--
Sample C	2.032±0.016	630.47±15.83	2.35±0.47	0.0150±0.0006	21.59±0.48	762	-0.148±0.007
Sample D	2.060±0.002	731.63±2.73	2.43±0.05	0.0180±0.0003	2.92±0.28	636	-0.025±0.001

Table 5.4 shows the list of values of g , $4\pi M_{eff}$, H_{Keff} , α , ΔH_0 , K_S , M_S of all the samples.

For a crystalline material, due to symmetric in crystal lattice, the orbital contribution of electron angular momentum is zero whereas the orbital contribution of magnetic moment (μ_L) is non-zero as a result the g-factor is greater than 2 following the below equation¹²⁹.

$$g = 2\left(1 + \frac{\mu_L}{\mu_S}\right) \dots\dots\dots(5.5)$$

As the interface breaks inversion symmetry, the surfaces and interfaces result the crystal field no longer symmetric. Therefore, g-factor follows the below relation¹²⁹ giving g-value less than

2;

$$g \approx 2 \left(1 - \frac{\mu_L}{\mu_S} \right) \dots\dots\dots(5.6)$$

All the bilayer samples have g value greater than 2 which is due to symmetry in crystal lattice whereas sample A has g value less than 2 due to breaking of inversion symmetry. Sample D has high value of g -factor than sample C.

The frequency independent part of ΔH , the inhomogeneous line broadening ΔH_0 is highest for sample C and lowest for sample A.

The effective demagnetization fields ($4\pi M_{eff}$) is not equal to saturation magnetization ($4\pi M_S$) due to the below relation;

$$4\pi M_{eff} = 4\pi M_S + \frac{2K_S}{M_S t_{FM}} \dots\dots\dots (5.7)$$

Where, K_S is perpendicular surface anisotropy constant and t_{FM} is the ferromagnetic layer thickness.

Highest value of K_S is observed in sample C which has also highest M_S as compared to samples A and D.

5.6. Polarized neutron reflectivity (PNR) study:

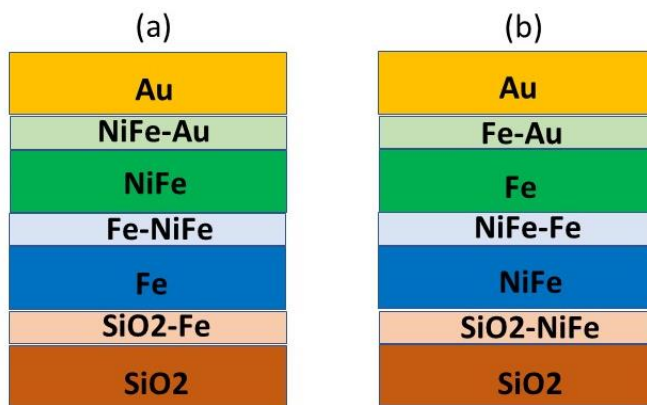


Figure 5.7: Schematic of all the interfaces and thin film layers in (a) sample C and (b) sample D.

Different interface models are considered to find the best figure of merit (FOM). The interfaces SiO₂-Fe, Fe-NiFe, and NiFe-Au for sample C are incorporated as shown in fig. 5.7. Similarly, for sample D the interfaces are SiO₂-NiFe, NiFe-Fe, and Fe-Au. With the above three interface model, the best FOM is found. In case of sample C, 1.57 μ_B /atom of magnetic moment for Fe and 0.79 μ_B /atom of magnetic moment for NiFe are found. The interface between Fe and NiFe has a magnetic moment of 0.90 μ_B /atom which is intermediate value of the former two and the interdiffusion layer of thickness 2.3 nm in sample C. The exchange coupling between Fe and NiFe gives the intermediate value of magnetic moment at the interface. The interface layer (between SiO₂ and Fe) has lesser magnetic moment of 1.00 μ_B /atom than Fe itself due to large lattice mismatch and interdiffusion in sample C¹⁴⁶.

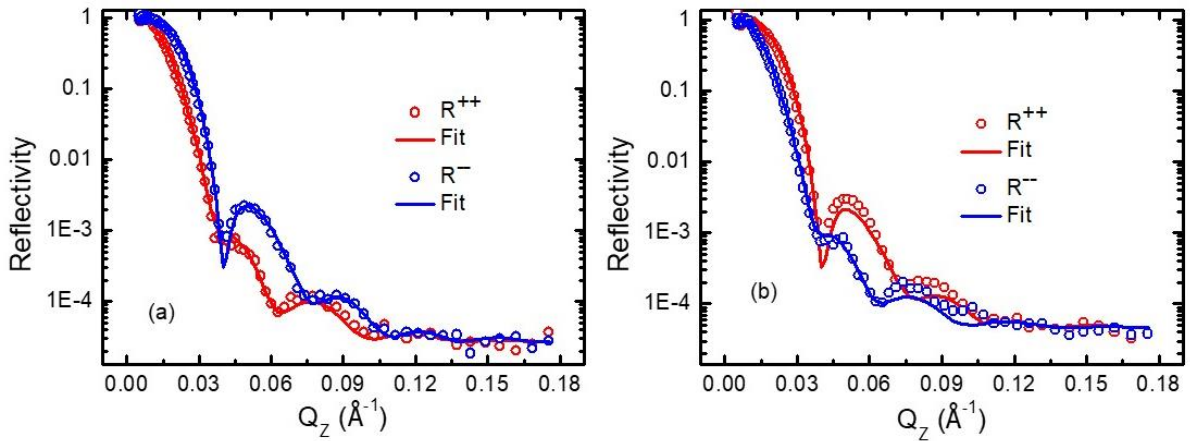


Figure 5.8: Polarized neutron reflectivity (PNR) data for sample C at room temperature with saturation magnetic field of -50 mT (a) and -4 mT (b) are applied along easy axis. The open circles are the experimental data points and the solid lines are fitted data for the non-spin flip (NSF) reflectivities R^{++} (red colour), R^{--} (blue colour), respectively.

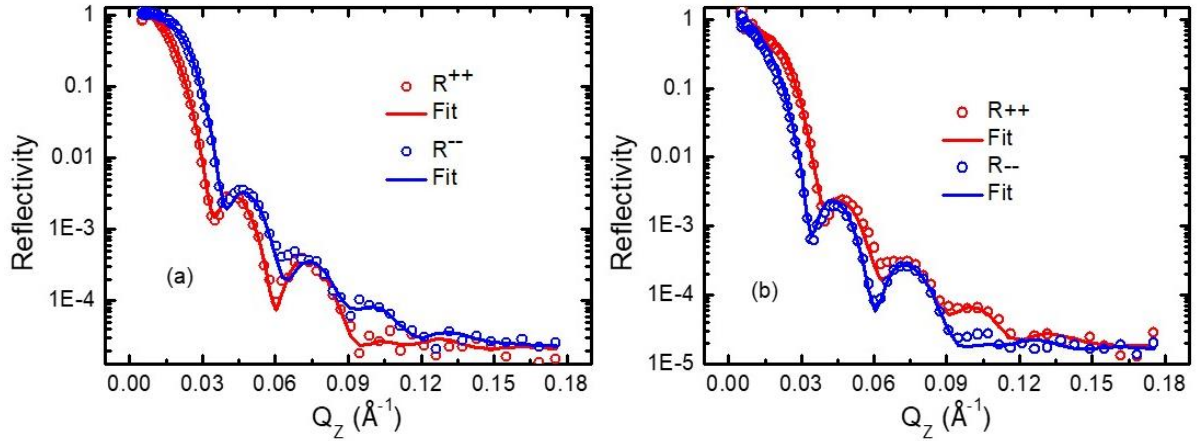


Figure 5.9: Polarized neutron reflectivity (PNR) data for sample D at room temperature measured at saturation magnetic field of -50 mT (a) and -1.2 mT of magnetic field near to coercivity (b) along easy axis. The open circles are the experimental data points and the solid lines are fitted data for the non-spin flip (NSF) reflectivities R^{++} (red colour), R^{--} (blue colour), respectively.

Also, due to lattice mismatch and interdiffusion, magnetic moment of $0.10 \mu_B/\text{atom}$ at the NiFe and Au interface in sample C is found. In case of sample D, $1.26 \mu_B/\text{atom}$ magnetic moment for Fe and $0.75 \mu_B/\text{atom}$ of magnetic moment for NiFe are found. Thus, the magnetic moment of sample C is more than sample D. Similarly, in SQUID measurements more magnetization is found in sample C than sample D. Due to exchange coupling between Fe and NiFe, an intermediate value of magnetic moment are found at the interface of the former two in sample D. In sample D, the interface between Au and Fe has a magnetic moment of $0.52 \mu_B/\text{atom}$ which is less than Fe magnetic moment due to development of strain because of lattice mismatch and interdiffusion. But, the interface between SiO₂ and NiFe has same magnetic moment as NiFe. Near to coercive field (4 mT) of sample C, except the interface of Au-NiFe and Fe-NiFe all other interfaces magnetic moment are reversed in opposite direction completely. 88 % of the interface magnetic moment of Fe-NiFe interface in sample C is reversed near to coercive field (4 mT) from saturation state. In sample D, 92 % of magnetic

moment of Fe has reversed their direction near to coercive field (1.2 mT) from saturation state. Again, 38 % of the magnetic moment at the Fe-Au interface has reversed direction in sample D whereas all other layers magnetic moment has reversed completely.

Comparing samples C and D, it is found that the interdiffusion layer thickness in all the interfaces is more in sample C than sample D. Again, the interface between Fe and NiFe has higher magnetic moment in sample C than D. The presence of high exchange coupling may be the possible reason for the higher value of coercivity and anisotropy field H_K in sample C than sample D.

5.7. Conclusions:

Bilayers of Fe and NiFe were deposited by alternating the order of magnetic layers. An enhancement in coercivity is observed in the case of the bilayer with Fe as bottom layer in comparison to the case of NiFe as a bottom layer. Bilayer sample with high anisotropy field H_K has smaller domains away from easy axis indicating the presence of high uniaxial magnetic anisotropy in this sample. In-plane angle dependent FMR study reveal the presence of uniaxial magnetic anisotropy in all the samples. Magnetic anisotropy was increased in bilayer samples, however, damping constant α remains similar to the single NiFe layer. This is good for application as we found low damping constant and higher anisotropy field. From PNR measurement, higher interdiffusion layer thickness and magnetic moment are found at the Fe-NiFe interface of 0.9 and 0.8 μ_B /atom at saturation and remanence in the magnetic bilayer with high coercive and anisotropy field whereas 0.76 μ_B /atom of magnetic moment is observed at the Fe-NiFe interface for saturation and remanence in sample D. This indicating the presence of high exchange coupling is responsible for the enhancement of coercive field H_C .

Chapter 6: A study of exchange bias and spin glass behavior in Fe/IrMn system.

6.1: Introduction:

In previous chapters, the static and dynamic magnetic properties of hard/soft ferromagnetic bilayers have been discussed. Hard/soft magnetic bilayers provide high H_C and M_S values compared to the constituent layers due to interface exchange coupling. Such exchange coupling between FM and AFM systems¹⁵ can sometime lead to the exchange bias effects. When field cooling the FM/AFM system below the Néel temperature (T_N) of the AFM layer, an anisotropy can be induced at the interface of a FM/AFM bilayer system. This anisotropy is unique in FM/AFM or similar bimagnetic system and known as unidirectional anisotropy^{12,13,147}. This anisotropy was first discovered by Meiklejohn and Bean in 1956 in field cooled Co particle covered by CoO¹². This unidirectional anisotropy gives loop shift¹⁴⁸ and coercivity enhancement¹⁴⁹. It is well known that the exchange bias effects are due to an interfacial exchange interaction between a FM and an AFM but the microscopic mechanism behind this effect is not well established. There are a number of parameters which affect the exchange bias and these include magnetic anisotropy¹⁵⁰, magnetic domains¹⁵¹, interface roughness¹⁵⁰, crystal structure^{152,153}. The interface of the FM and AFM systems can have spin glass like frustration¹⁶ and uncompensated AFM order² etc. The spin glass like disorder at the interface is due to interface roughness², structural disorder¹⁶ and chemical intermixing² etc. The exchange bias effect as an interfacial interaction between the FM and AFM system are mostly studied^{29,150} but the ‘bulk’ AFM spins contribution to exchange bias is not fully explored¹⁵⁴. Also, exchange bias effects have technological importance in constructing spintronic devices such as spin valves, magnetic random-access memories (MRAMs) etc^{16,154-157}. The variation of the exchange bias field with the thickness of the AFM¹⁵⁸⁻¹⁶³ indicates the contribution of ‘bulk’ part of AFM to the exchange bias¹⁵⁶. Exchange bias depends on the

presence of defects not only at the interface but also at the ‘bulk’ part of the AFM¹⁶⁴. Different theoretical models have been proposed to explain the mechanism of exchange bias.

Meiklejohn and Bean model says that EB field is a result of competition between Zeeman and exchange energies of an ideal, smooth and uncompensated FM/AFM interface^{2,150}. In this approach, the exchange bias field is generally found to be two orders of magnitude larger than the experimental value¹⁵⁰. In domain state model nonmagnetic impurities are thought to be present in the AFM ‘bulk’ that gives similar exchange bias field as experiments². In another model known as spin glass model, the interface between FM and AFM is considered to have spin glass like frustration. The frozen uncompensated spins at the interface give rise to exchange bias field and low anisotropy rotatable spins are responsible for enhanced coercivity².

Before describing the exchange bias effects in Fe/IrMn system, the fundamental properties of Fe and IrMn will be described first. Fe is a ferromagnet with Curie temperature (T_C) of 1043 K in the bulk form¹⁶⁵ and IrMn is an AFM with Néel temperature (T_N) of 690 K in bulk¹⁶⁶. Fe has a cubic crystal structure with lattice parameters $a = b = c = 3.76 \text{ \AA}$ ¹⁶⁷. IrMn also crystallizes in a cubic structure with lattice parameters $a = b = c = 3.78 \text{ \AA}$ ¹⁶⁷. The relatively, higher Néel temperature (T_N) of IrMn can be tuned to obtain blocking temperature of AFM near room temperature by exploiting finite size effect¹⁶⁸. IrMn can be crystallized in disordered γ -IrMn₃ and ordered L1₂-IrMn₃ spin structures¹⁶⁹.

It has been found that IrMn exhibits spin glass behavior^{16,160,170–172} and sometimes acts as an AFM¹⁵⁰ in some of the reported bilayers. The presence of spin glass like interface has been investigated from the temperature^{16,149,170} and cooling field dependence of exchange bias field¹⁷³. An exponential decay of $\mu_0 H_{EB}$, and $\mu_0 H_C$ with temperature and a decrease of $\mu_0 H_{EB}$ with $\mu_0 H_{FC}$ are found. The training effect data are fitted with a model considering frozen and rotatable spins at the interface and spin configurational relaxation model¹⁵⁵. The exchange bias

field was found to vary with the thickness of the AFM layer indicating contribution of ‘bulk’ part of the AFM to exchange bias.

6.2: Experimental details:

All the Fe/IrMn bilayers have been deposited by dc magnetron sputtering on Si (100) substrates. Cu of 10 nm has been deposited on Ta of 1 nm thickness as buffer layer. Cu of 3 nm thickness has been deposited as capping layer to avoid oxidation. All the magnetic measurements have been performed using superconducting quantum interference device (SQUID) based magnetometer. Grazing incidence X-ray diffraction (GIXRD) measurements have been performed by an X-ray diffractometer from Rigaku using $\text{CuK}\alpha$ source. Table 6.1 shows the sample nomenclature and configurations.

Table 6.1: sample nomenclature and configuration of all the samples.

Sample name	Sample configuration
A1	Si (100)/Ta (1 nm)/Cu (10 nm)/IrMn (10 nm)/Fe (10 nm)/Cu (3 nm)
A2	Si (100)/Ta (1 nm)/Cu (10 nm)/IrMn (5 nm)/Fe (10 nm)/Cu (3 nm)
A3	Si (100)/Ta (1 nm)/Cu (10 nm)/IrMn (3 nm)/Fe (10 nm)/Cu (3 nm)

6.3: Structural characterization:

The presence of IrMn and Fe has been verified using GIXRD patterns. Fe (111) and IrMn (111)¹⁷⁴ reflections have been found in the GIXRD patterns indicating oriented growth of IrMn in all the bilayer samples. The X-ray diffraction patterns of all the samples are shown in figure 6.1(a-c). The structure of IrMn is cubic and the composition of alloy is $\text{Ir}_{20}\text{Mn}_{80}$. IrMn can be crystallized in disordered γ -IrMn3 and ordered L_{12} -IrMn3 spin structures. Kohn et al., reported high temperature annealing (above 700 K) is required to get ordered L_{12} -IrMn3 spin structure¹⁶⁹. $\text{Ir}_x\text{Mn}_{1-x}$ with $0.15 < x < 0.25$ are chemically disordered.

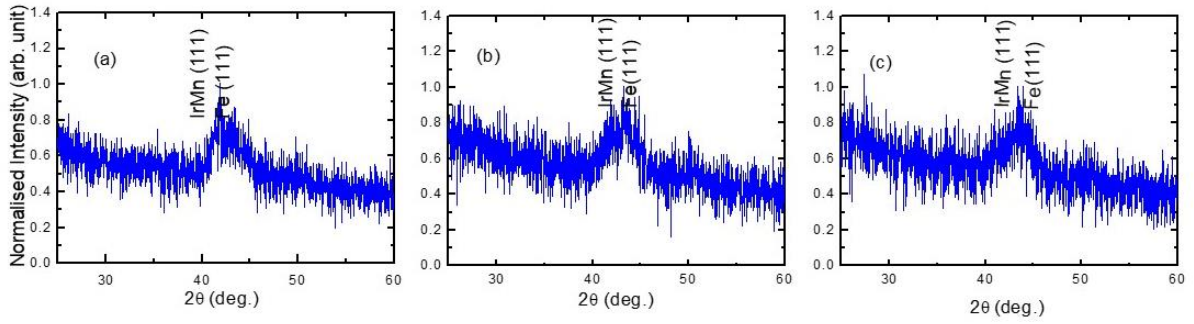


Figure 6.1: (a)-(c) shows the GIXRD patterns of the bilayers A1, A2, and A3, respectively.

6.4: Magnetic characterization: Temperature and cooling field dependent study:

Figures 6.2(a) and (b) show the plot of H_{EB} , H_C vs T of all the samples. All the samples were field cooled from 400 K down to the desired temperature in 1 T field. Exponential decay of H_{EB} , and H_C with temperature is observed. The H_{EB} , and H_C temperature dependence follow similar trend for all the samples. From literature it is found that the maximum in H_{EB} vs T corresponds to a minimum in H_C vs T plots and vice versa for conventional FM/AFM systems¹⁵⁰. The exponential decay of H_{EB} , H_C with temperature is attributed to a spin glass like interface of the present bilayers^{16,149,170,175}. The exchange bias blocking temperature is found as 400 K for all the bilayers. At higher temperatures above ~ 50 K, gradual decrease of both H_{EB} , and H_C , with temperature, is found due to thermal excitations¹⁴⁹. At higher temperatures, the interfacial spins under the polarizing action of the ‘bulk’ AFM spins contribute to loop shift and low anisotropy interfacial spins give rise to coercivity. At low temperatures below ~ 50 K, a sudden rise of H_{EB} is found due to freezing of the spin glass like interfacial spins^{16,149,170}.

Figure 6.3 shows the plot of H_{EB} , and H_C with cooling field. The bilayers were field cooled from 400 to 5 K in presence of various cooling fields (0.05 to 5 T). In conventional FM/AFM system, the exchange bias field increases with an increase of cooling field¹⁷⁶ due to an enhance population of pinned moments along the cooling field direction. However, in a

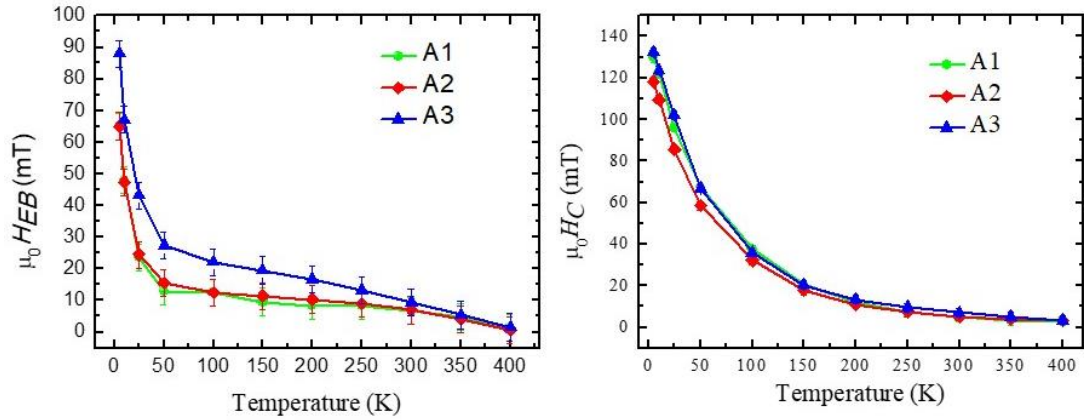


Figure 6.2: (a) H_{EB} vs T and (b) H_C vs T plots of the samples A1-A3.

FM/spin glass system the exchange bias field is found to decrease with increase of cooling field¹⁷³ due to random interface effect¹⁶⁴. The cooling field acts on the ‘bulk’ of the spin glass to induce a net magnetization¹⁶⁴ that results in exchange bias. The decrease of exchange bias field is found with cooling field due to random exchange coupling with the FM layer.

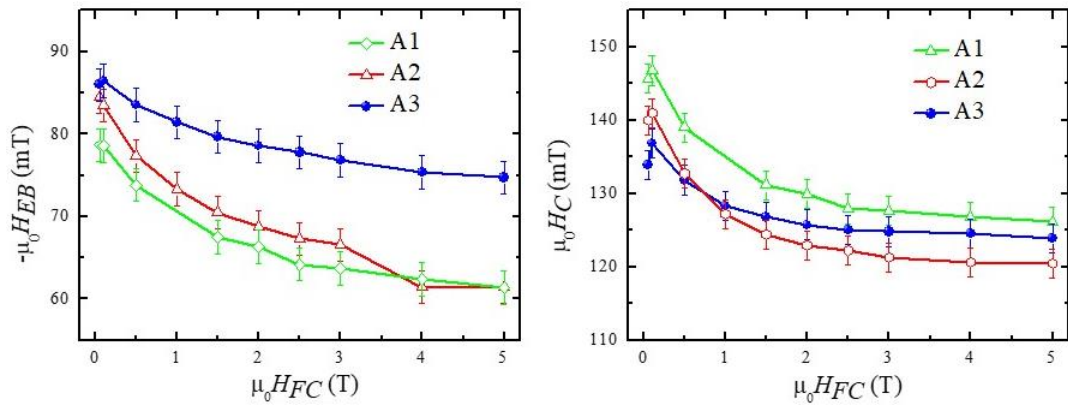


Figure 6.3: Plots of (a) H_{EB} vs H_{FC} and (b) H_C vs H_{FC} for the samples A1-A3.

Figure 6.4 shows the AFM thickness (t_{AFM}) dependence of exchange bias field at various cooling fields (2, 3 and 4 T). The $\mu_0 H_{EB}$ decreases with increasing t_{AFM} from 3 to 5 nm and it levels off thereafter. There is critical thickness of AFM layer where the onset of exchange bias occurs. This AFM thickness dependence of exchange bias is explained in literature by the

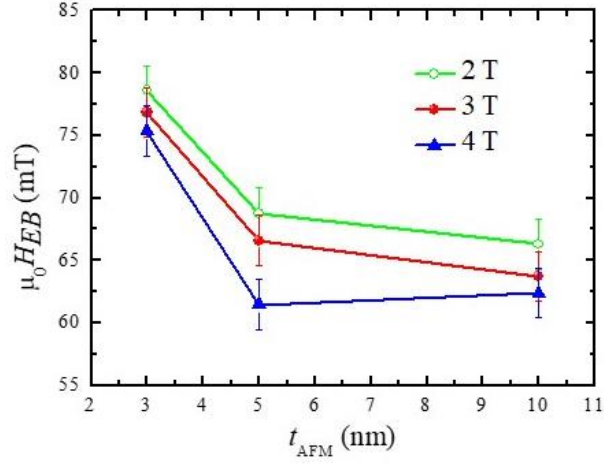


Figure 6.4: The variation of H_{EB} with t_{AFM} at different cooling fields for all the samples.

formation of partial domain wall in the AFM parallel to the interface¹⁵⁰. It can also be explained due to the microstructural changes in the AFM layer²⁹.

6.5: Magnetic characterization: Training effect:

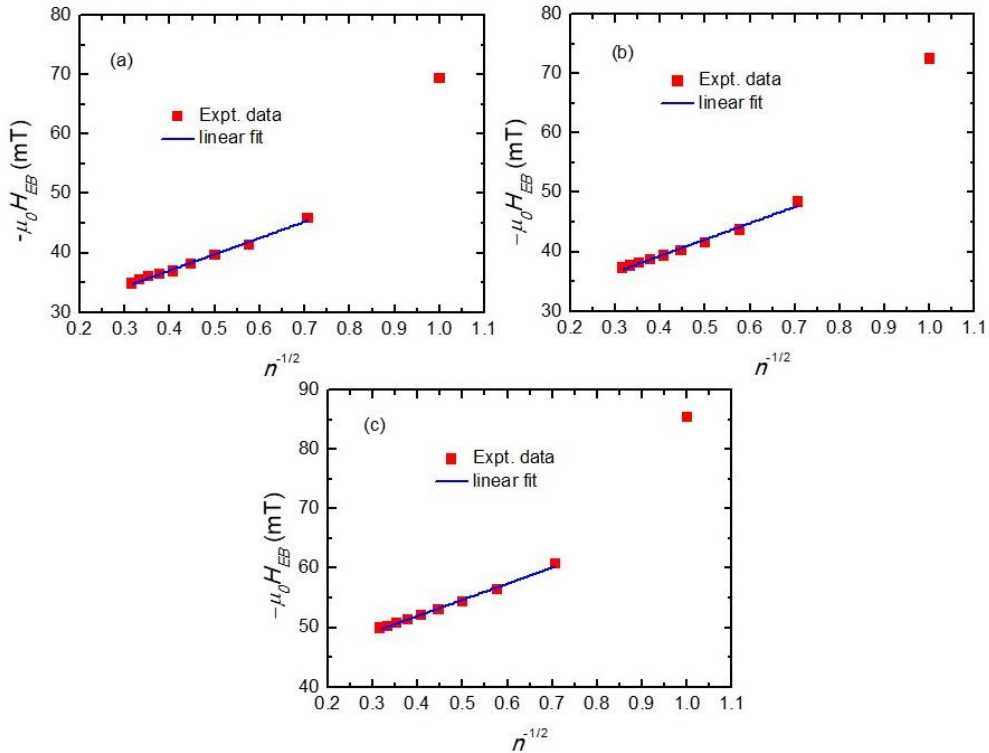


Figure 6.5: (a)-(c) Linear fits of the $\mu_0 H_{EB}$ vs $n^{-1/2}$ data of the samples A1-A3.

The $\mu_0 H_{EB}$ vs $n^{-1/2}$ data (fig. 6.5) is fitted to determine the value of $\mu_0 H_{EB\infty}$ using the equation

below¹⁷⁷;

$$\mu_0 H_{EB}(n) = \mu_0 H_{EB\infty} + \frac{K}{\sqrt{n}} \dots\dots\dots (6.1)$$

Where, $\mu_0 H_{EB}(n)$ is the exchange bias field of the n^{th} loop, $\mu_0 H_{EB\infty}$ is the exchange bias field in the limit of infinite number of loops and K is a system dependent constant.

Figures 6.6 (a)-(c) show the 1st, 2nd and 10th magnetic hysteresis loops obtained from training effect measurements. The training effect data are fitted using recursive relation^{155,178,179} and double exponential decay function^{155,157,178} (figs. 6.6 (d)-(f)). The M-H loop were obtained after field cooling the samples in 1 T field from 400 to 5 K. Both of these models fit the training effect data well. The recursive relation is based on the spin configurational relaxation model and describes the training effect data for many classes of materials including spin glasses. The double exponential decay function is basically the frozen and rotatable spin relaxation model. Both of these models can be used for spin glass like interface. The double exponential decay function gives additional information about the frozen and rotatable interfacial spins. The spin configurational relaxation model is given by the equation below;

$$\mu_0(H_{EB}(n+1) - H_{EB}(n)) = -\gamma_H[\mu_0(H_{EB}(n) - H_{EB\infty})]^3 \dots\dots\dots(6.2)$$

Where, $\mu_0 H_{EB\infty}$ is obtained from the linear fitting of $\mu_0 H_{EB}$ vs $n^{-1/2}$ data (fig. 6.5). γ_H is obtained from the recursive relation given in eq. 6.2. The values of $\mu_0 H_{EB\infty}$ and γ_H are tabulated in table 6.2. Quite similar values of γ_H in all the samples indicate that the relaxation behavior of interfacial spins from non-equilibrium to equilibrium states is similar¹⁷⁸.

Next, spin glass approach is considered containing both frozen and rotatable spins at the interface. The frozen and rotatable spin relaxation model is given by the equation below¹⁵⁷,

$$\mu_0 H_{EB}(n) = \mu_0 H_{EB\infty} + \mu_0 A_f \exp\left(\frac{-n}{P_f}\right) + \mu_0 A_i \exp\left(\frac{-n}{P_i}\right) \dots\dots\dots (6.3)$$

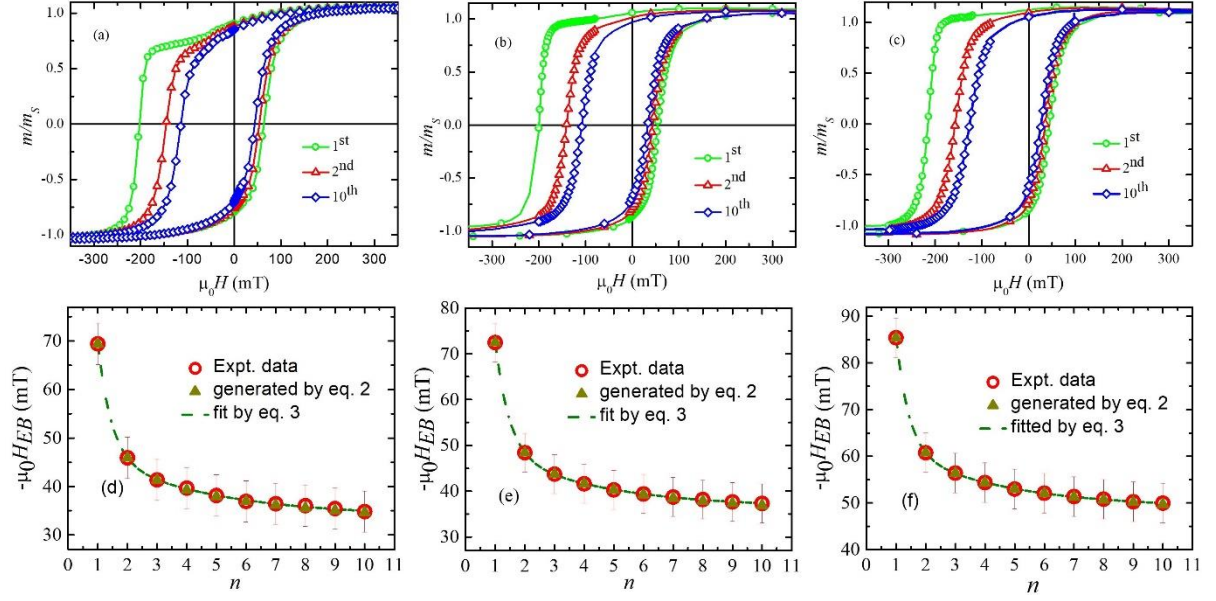


Figure 6.6: (a)-(c) show the 1st, 2nd, and 10th subsequent magnetic hysteresis loops of the samples A1-A3, respectively. (d)-(f): The plots of $\mu_0 H_{EB}$ vs n for the samples A1-A3. The red color open circles are the experimental data points, the olive colored segment line is the fitted data using eq. 6.3 and dark yellow colored triangular data points are generated by eq. 6.2.

Where A_f, P_f are the parameters related to interfacial frozen spins and A_i, P_i are the parameters for the interfacial rotatable spins. A_f and A_i have the dimension of mT. P_f and P_i are the dimensionless quantities. P_f and P_i are the relaxation rates of the interfacial frozen and rotatable spin components, respectively. All the parameters obtained from the fit using equations 6.1, 6.2 and 6.3 are given in table 6.2. The $\mu_0 H_{EB\infty}$ shows a systematic decrease from 48.9 mT to 33.8 mT with increasing thickness of IrMn. The weighing factor $\mu_0 A_f$ shows a systematic decrease with increase in thickness of IrMn except little discrepancy for sample A2. The weighing factor $\mu_0 A_i$ shows a systematic decrease with an increase in the thickness of IrMn.

Table 6.2: Parameters obtained from the fitting of the training effect data using equation 6.1, 6.2, and 6.3.

Name	Eq. (6.2) parameters		Eq. (6.3) parameters					
	$\mu_0 H_{EB\infty}$ (mT) from eq. (6.1)	γ_H (10^{-4} mT^{-2})	$\mu_0 H_{EB\infty}$ (mT)	$\mu_0 A_f$ (mT)	P_f	$\mu_0 A_i$ (mT)	P_i	P_i/P_f
A1	26.10±0.42	5.85	33.8±0.6	206.4 ±34.3	0.46±0.04	15.8 ±1.6	3.93 ±0.7	8.54
A2	28.26±0.51	5.73	36.4±0.2	199.5 ±11.5	0.47±0.02	16.0 ±0.8	3.56 ±0.2	7.57
A3	41.09±0.38	5.73	48.9±0.2	243.5 ±16.6	0.43±0.02	16.5 ±0.7	3.58 ±0.2	8.33

The relaxation rates of interfacial frozen and rotatable components P_f and P_i are almost constant in all the magnetic bilayers. The higher value $\mu_0 A_f$ compared to $\mu_0 A_i$ indicates that the training effect is mainly due to the frozen spin components¹⁵⁵. The ratio P_i/P_f is approx. 8 for all the bilayers.

In a FM/AFM system the relaxation of the interfacial spins can occur due to thermal or athermal effects¹⁵⁵. In thermal training effect, gradual decrease of $\mu_0 H_{EB}$ is found with loop number n due to relaxation of uncompensated interfacial spins from non-equilibrium configuration¹⁵⁵. However, in athermal training effect, there is large reduction of $\mu_0 H_{EB}$ between $n=1^{\text{st}}$ and 2^{nd} magnetic hysteresis loops. A gradual decrease of $\mu_0 H_{EB}$ is found thereafter due to relaxation of metastable frozen spin glass like interfacial spins¹⁵⁵.

6.6: Conclusions:

The training effect, temperature and cooling field dependence of exchange bias in Fe/IrMn bilayers have been studied. Exponential decay of both H_{EB} and H_C is found in all the samples indicating the presence of spin glass like interface. In contrast with conventional FM/AFM systems, the decrease of exchange bias field with cooling field is found showing the existence of spin glass like interface. The variation of exchange bias field with the thickness of AFM indicates that the ‘bulk’ part of the AFM contributes to the observed exchange bias. The

training effect data is fitted using recursive relation and frozen and rotatable spin relaxation model. The interfacial rotatable spins are found to relax 8 times faster than the frozen spins.

Chapter 7: Exchange bias in Ni₅₀Mn₅₀/Co₄₀Fe₄₀B₂₀ system.

7.1: Introduction:

The main requirements of the exchange biased spintronic devices are good thermal stability and reasonably strong exchange coupling¹⁸⁰. The following classes of AFM materials have been studied widely. Oxide AFMs, viz. CoO^{26,181}, NiO^{182,183}, and Co_{1-x}Ni_xO^{182,183} are one kind, which do not have high H_{EB} ¹⁸⁰. Other kind of AFM are Mn based, namely FeMn, IrMn, NiMn, PdMn and PtMn^{184,185} and these materials have relatively good thermal stability and high H_{EB} ¹⁸⁶. Mn based AFMs have attracted considerable research interest due to their high T_N e.g. T_N of Ni₅₀Mn₅₀ is ~1070 K^{187,188}. However, interdiffusion is the main problem in Mn based AFM when it is subjected to heat^{180,189,190}.

One can control the microstructure by selecting a proper seed layer and hence the magnetic properties¹⁸⁰. Structural orientations affect the exchange anisotropy of coupled FM and AFM systems¹⁹¹. Structural orientations can be modified by proper selection of substrate, buffer layer and growth conditions¹⁹¹. As grown NiMn is paramagnetic with face centred cubic (FCC) structure whereas post deposition annealing gives rise to antiferromagnetism with face centred tetragonal (FCT) structure¹⁹². The lattice constants of FCT NiMn are $a=b=3.74 \text{ \AA}$ and $c=3.52 \text{ \AA}$ ¹⁹². It's also reported that by choosing proper seed layer one can induce AFM order¹⁸⁷. EB properties have been found in Co/NiMn system deposited on top of Cu (001) substrate¹⁹³. EB has also been investigated in some of the AFMs namely NiMn, IrMn, Cr₂O₃ etc. grown on Pt buffer layer^{194,195}.

Fundamental understanding of surfaces and interfaces of FM/AFM system is required apart from exploring its potential application^{12,29}. EB has been studied widely in core-shell nanoparticles, layered films, and inhomogeneous materials^{196,197}. One of the important aspects is the role of disorder and frustration on EB in the case of compensated or uncompensated

interface^{198–203}. FM/SG systems are most appropriate to study the role of frustration on exchange bias¹⁹⁶. AgMn and CuMn systems have been reported to exhibit spin glass behaviour¹⁹⁶. Various disordered systems such as nanogranular Fe/FeO system, Fe₃O₄ nanoparticles, [Co₂MnGe/Au]_n, [Co₂MnGe/Cr]_n, [Co₂MnGe/Cu₂MnAl]_n etc. are also modelled as FM/SG composite¹⁹⁶.

In this chapter, temperature and cooling field (H_{FC}) dependence of exchange bias have been performed in NiMn/CoFeB systems. Training effect study is also carried out in these thin films. Sign change of exchange bias is found in some of the NiMn/CoFeB systems below the blocking temperature (T_b) such sign reversal of EB may be explained by considering indirect exchange interaction from the spins deep inside the spin glass layer and near to the interface^{196,197} or the SG to AFM transition driven by temperature²⁰⁴. AC susceptibility measurements have been performed to determine if the system is non-interacting like superparamagnets or interacting like spin glasses.

7.2: Experimental details:

Deposition of NiMn/CoFeB bilayers on Si (100) substrates has been performed by dc magnetron sputtering at RT. Pt of 2.5 nm thickness has been deposited on top of Ta of 3 nm thickness as seed layer. Ta of 3 nm thickness has been deposited as capping layer to avoid oxidation. The substrate was rotated at 20 rotation per minute (rpm) speed during deposition of all the magnetic layers to avoid growth induced uniaxial magnetic anisotropy. All the static magnetic measurements have been performed using a Quantum Design SQUID magnetometer. We found amorphous growth of NiMn in the studied bilayers from GIXRD measurements.

Table 7.1: Details of sample nomenclature and configuration.

Sample name	Configuration
A5	Si(100)/Ta(3 nm)/Pt(2.5 nm)/NiMn (5 nm)/CoFeB(5 nm)/Ta (3 nm)
A10	Si(100)/Ta(3 nm)/Pt(2.5 nm)/NiMn (10 nm)/CoFeB(5 nm)/Ta (3 nm)
A15	Si(100)/Ta(3 nm)/Pt(2.5 nm)/NiMn (15 nm)/CoFeB(5 nm)/Ta (3 nm)

7.3: Study of static magnetic properties:

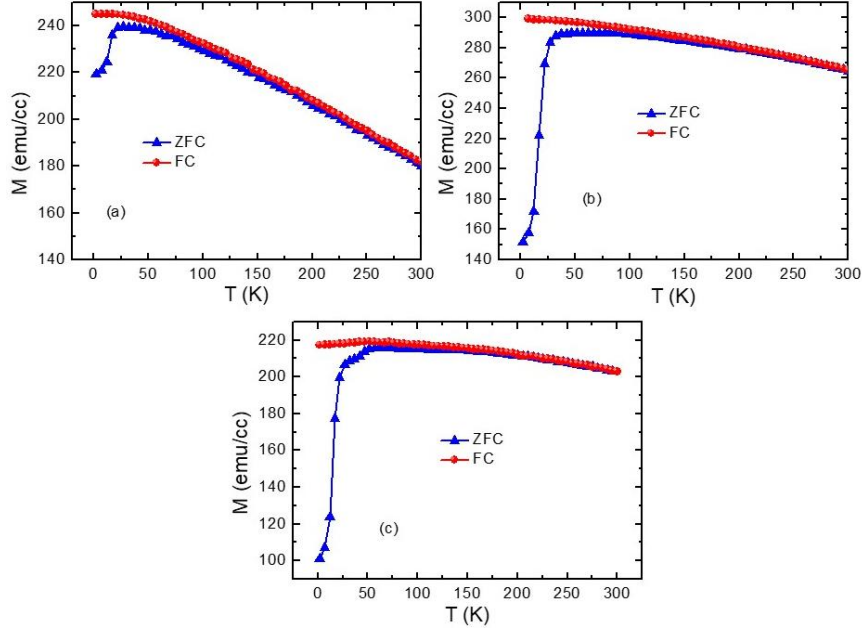


Figure 7.1: Zero field cooled (ZFC)-field cooled (FC) magnetization (M) vs temperature (T) curves of the samples (a) A5 (b) A10 and (c) A15.

M - T measurements have been carried out by field cooling (FC) and zero field cooling (ZFC) the samples from 300 to 2 K in presence of 100 Oe field. Figures 7.1(a)-(c) show the ZFC-FC MT curves of the samples A5, A10 and A15, respectively. The peak temperatures (T_P) of 22, 33, and 47 K have been found in samples A5, A10 and A15, respectively. Thus, T_P has increased from 22 to 47 K by increasing the thickness of NiMn from 5 to 15 nm. The peak temperature T_P has broadened with the increase in thickness of NiMn due to the enhancement of interaction between NiMn and CoFeB layers²⁰⁵. The temperature at which ZFC and FC magnetization bifurcates is known as irreversibility temperature T_{irr} . $T_{irr} > T_P$ in samples A5 and A10 whereas in sample A15, T_{irr} and T_P are similar. The FC magnetization below T_P is constant.

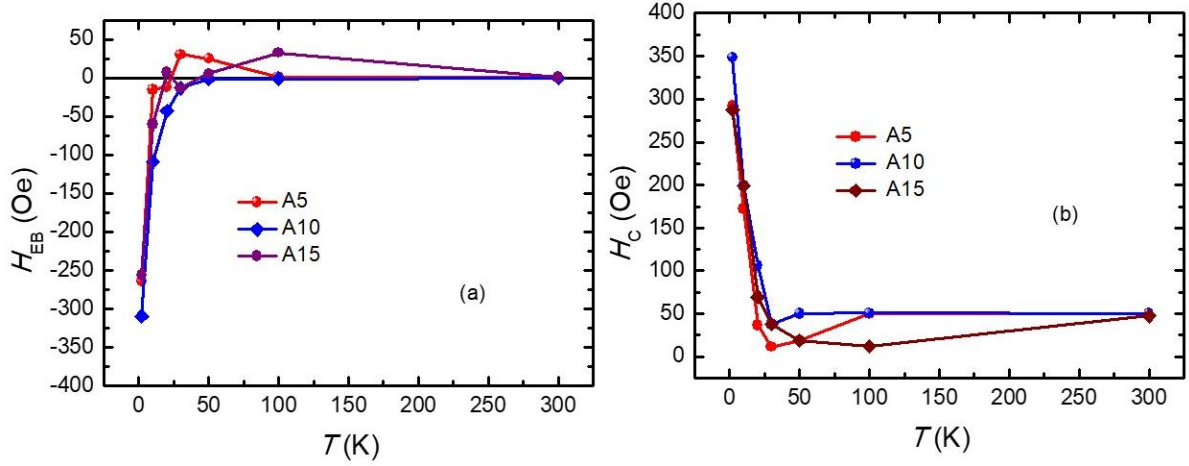


Figure 7.2: The plots of (a) H_{EB} (b) H_C vs temperature (T) for all the samples.

Figure 7.2 shows the plots of H_{EB} (a) and H_C (b) vs T of all the samples. To study the temperature dependence of EB, field cooling from 400 K to the desired temperature (2, 10, 20, 30, 50, 100 and 300 K) were performed in presence of 2 kOe field. An exponential decay of H_C , with temperature, has been found in all the magnetic bilayers. Exponential decay of H_{EB} is found in sample A10. In samples A5 and A15, the exponential decay of H_{EB} with T is found till the compensation temperature T_0 , the temperature where the sign change of exchange bias is observed. A sudden rise of H_{EB} and H_C is found below ~ 20 K which may be due to the spin glass nature of NiMn^{206,207}. In particular, the contribution of low anisotropy rotatable spins^{206,207} which may develop from the disorder and frustration in NiMn spin glass phase and interface can contribute to such a low-temperature rise of H_C . At higher temperatures, above ~ 20 K, the interfacial spins which are under the polarizing action of the ‘bulk’ of the NiMn layer give rise to loop shift and the low anisotropy interfacial spins contribute to the H_C . Due to thermal excitations, at higher temperatures, H_C vs temperature (T) plot deviates from exponential decay behavior²⁰⁸. Sign change of EB has been found in samples A5 and A15, thus, EB is NiMn thickness dependent. Similar, sign change of exchange bias has been reported in FM/spin glass

system^{196,197} which has been explained by considering indirect exchange coupling between the interface and ‘bulk’ NiMn spins^{196,197}. Below 20 K, the indirect exchange coupling of the ‘bulk’ NiMn spins with the interfacial FM spins is independent of temperature. This indirect exchange coupling vanishes at 20 K and at T_0 , the coupling changes sign. The highest blocking temperature has been found in sample A15.

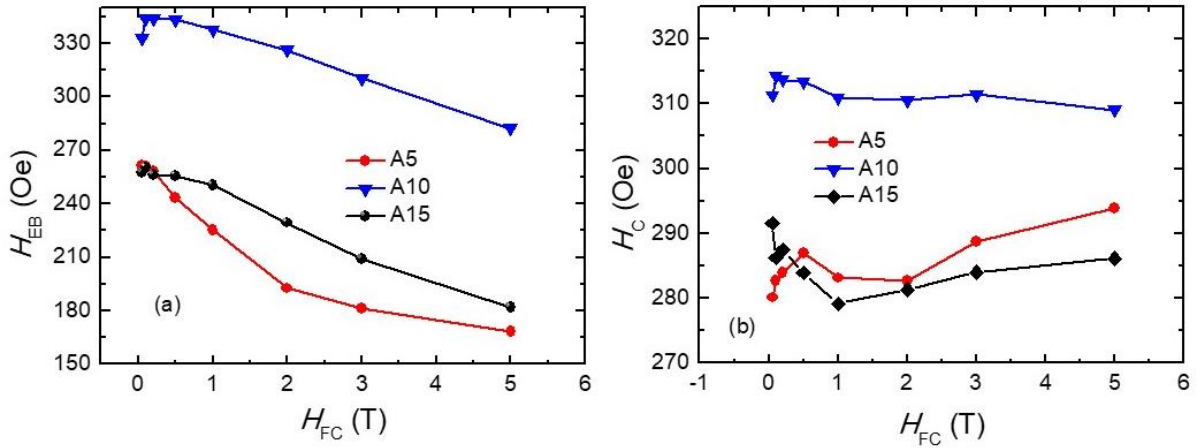


Figure 7.3: Cooling field dependence of (a) H_{EB} and (b) H_C for all the samples.

Figure 7.3 shows the variation of H_{EB} and H_C with H_{FC} for the samples A5, A10 and A15. To perform the cooling field dependence of EB, the samples were field cooled from 400 to 2 K in presence of various magnetic fields (0.05, 0.1, 0.2, 0.5, 1, 2, 3 and 5 T). A decrease of H_{EB} with cooling field, H_{FC} is found, whereas H_C remains almost constant. This type of behavior of H_{EB} with H_{FC} has been observed in FM/spin glass system¹⁷³. In conventional FM/AFM system, H_{EB} increases with increasing H_{FC} due to increase in the population of pinned moments along the cooling field direction. However, due to random interface effect, H_{EB} is found to decrease with cooling field in FM/spin glass system¹⁶⁴. In FM/spin glass system, the coupling of the spin glass with the FM layer is random resulting into a decrease of H_{EB} with H_{FC} ¹⁶⁴. Therefore, the spin glass state of NiMn might be a reason for this decrease of the H_{EB} with H_{FC} .

The highest H_{EB} has been found in sample A10. The variation of H_{EB} with the thickness of NiMn indicates that not only the interface but also the ‘bulk’ part of the NiMn contributes to EB.

7.4: Training effect:

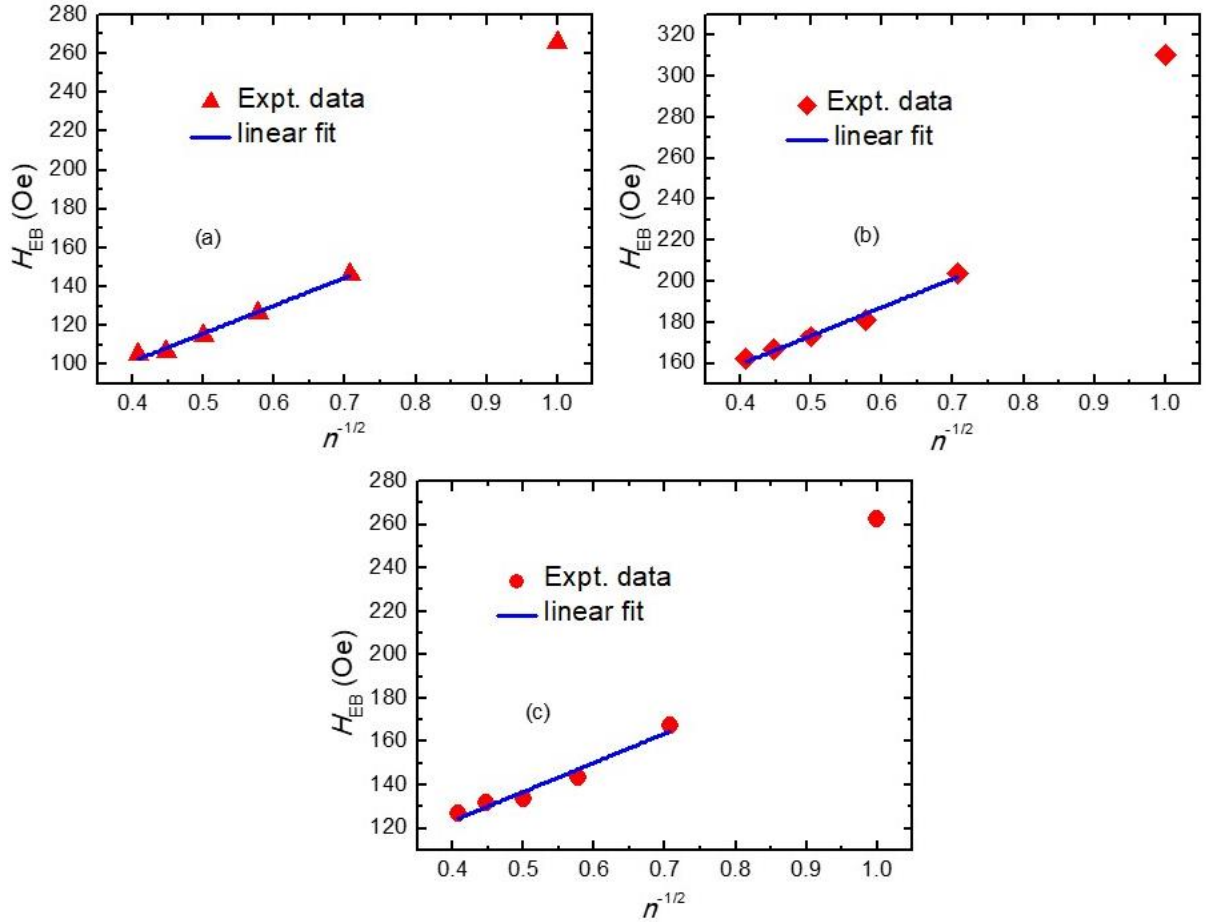


Figure 7.4: The linear fits of H_{EB} vs $n^{-1/2}$ experimental data using eq. (7.1) for samples (a) A5 (b) A10, and (c) A15.

To determine the value of $H_{EB\infty}$, the H_{EB} vs $n^{-1/2}$ data have been fitted (fig. 7.4) using the equation below¹⁷⁷;

$$H_{EB}(n) = H_{EB\infty} + \frac{k}{\sqrt{n}} \dots\dots\dots (7.1)$$

Where k is a system dependent constant, $H_{EB}(n)$ is the exchange bias field of the n^{th} loop, and $H_{EB\infty}$ is the exchange bias field in the limit of infinite number of loops. The values of $H_{EB\infty}$

determined from the fit are given in table 7.2. $H_{EB\infty}$ follows the trend similar to H_{EB} .

The 1st, 2nd, 6th M - H loops of the samples A5, A10 and A15 obtained from training effect measurements are shown in figures 7.5(a)-(c). The fitted results are also shown in figures 7.5(d)-(f). The films were field cooled from 400 to 5 K in presence of 500 Oe field to measure the first loop and then the subsequent M-H loops are measured.

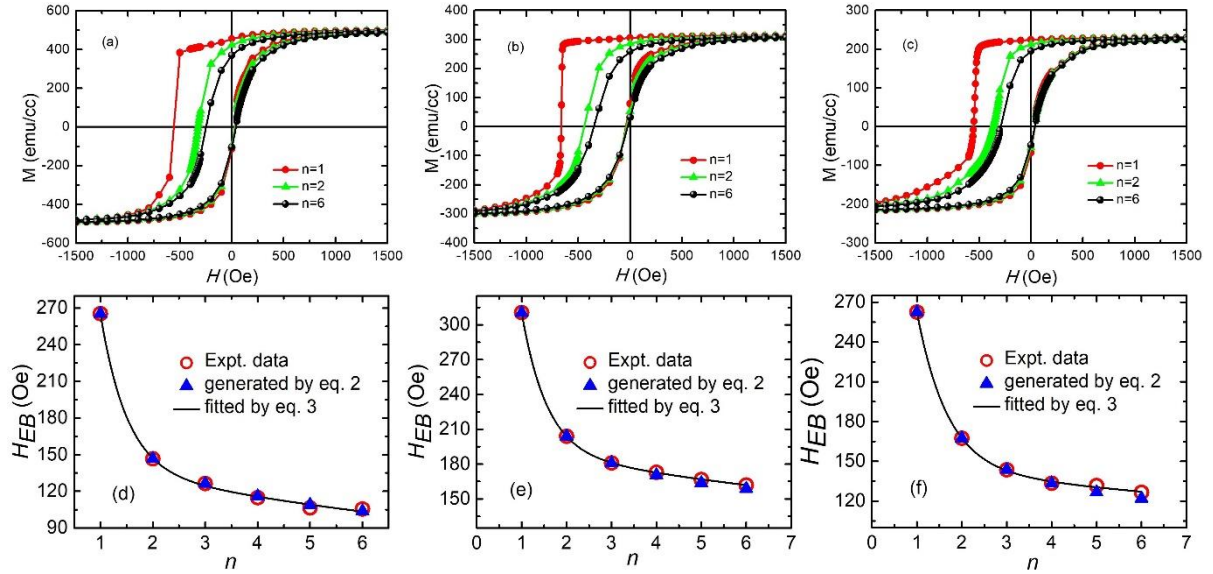


Figure 7.5: 1st, 2nd, 6th subsequent magnetic hysteresis loops of samples (a) A5 (b) A10 and (c) A15. (d)-(f): show the plot of H_{EB} vs n of the samples A5, A10 and A15, respectively. The open red circles are the experimental data points, blue triangular data points are generated from eq. 7.2 and black solid line is the fitted data using eq. 7.3.

$H_{EB\infty}$ values, obtained from eq. 7.1, are used in eq. 7.2 and 7.3. γ_H values are obtained from eq. 7.2 and given in table 7.2.

The training effect data is fitted using the recursive relation (eq. 7.2) which may be used for spin glass like frustrated system^{178,179};

$$H_{EB}(n + 1) - H_{EB}(n) = -\gamma_H(H_{EB}(n) - H_{EB\infty})^3 \quad \dots\dots\dots (7.2)$$

Where, $H_{EB}(n)$, $H_{EB}(n + 1)$ and $H_{EB\infty}$ are the exchange bias fields of the n^{th} , $(n+1)^{\text{th}}$ and in the limit of infinite number of loops, respectively. γ_H is the characteristic decay rate of the

training effect. The small value of γ_H indicates large deviation from equilibrium steady state and hence large training effect which is according to relaxation theory¹⁷⁸.

Table 7.2: The fitting parameters obtained using eq. 7.1, 7.2 and 7.3.

Sample	$H_{EB\infty}$ (Oe)	γ_H (10^{-5} Oe ⁻²)	A_f (Oe)	A_i (Oe)	P_f	P_i	P_i/P_f
A5	44.17 ± 4.88	1.88	934.83 ± 31.30	102.73 ± 4.78	0.50 \pm 0.08	10.88 \pm 1.36	21.76
A10	104.29 ± 5.15	2.32	722.96 ± 19.53	94.00 ± 1.35	0.55 \pm 0.01	12.26 \pm 0.44	22.29
A15	69.76 ± 8.34	2.55	516.14 ± 45.51	78.47 ± 6.81	0.67 \pm 0.05	19.05 \pm 6.19	28.43

The training effect experimental data is also fitted using double exponential decay function which considers both the rotatable and frozen spins at the interface of NiMn/CoFeB system. The double exponential decay function is given by the equation below¹⁵⁷;

$$H_{EB}(n) = H_{EB\infty} + A_f \exp\left(\frac{-n}{P_f}\right) + A_i \exp\left(\frac{-n}{P_i}\right) \dots\dots\dots (7.3)$$

Where, A_f , P_f are the interfacial frozen spin parameters and A_i , P_i are the interfacial rotatable spin parameters of the NiMn/CoFeB system. P_f and P_i are the relaxation rates of interfacial frozen and rotatable spins, respectively. P_f and P_i are dimensionless. A_f and A_i have the dimension of Oe. The weighing factors A_f and A_i show a continuous decrease with increase in thickness of NiMn from 5 to 15 nm. In all samples, the weighing factor A_f has higher value than A_i indicating that the frozen components contributes more for the training effect. P_f is almost constant for all the samples. But P_i increases as NiMn becomes thicker leading to an increment of P_i/P_f . Thus, the relaxation rate of interfacial rotatable spins P_i is higher than the frozen spins P_f . All the parameters obtained after the fittings of equations 7.1, 7.2 and 7.3 are given in table 7.2.

In the M-H loops of training effect (fig. 7.5), the magnitude of H_{EB} reduces in the descending part of the loop whereas the magnitude remains constant in the ascending part of the loop

similar to FM/AFM systems. The training effect is due to the irreversible movement of domain wall in the AFM or spin glass.

7.5: Study of dynamic magnetic properties:

To confirm that NiMn is a spin glass in the NiMn/CoFeB bilayer, ac susceptibility measurements were performed at different frequencies w.r.t. temperature in presence of an ac field of 3 Oe. The peak temperature T_f , obtained from the real part of the ac susceptibility (χ') vs temperature (T) plot, is found to shift towards higher temperature indicating the presence of spin glass phase.

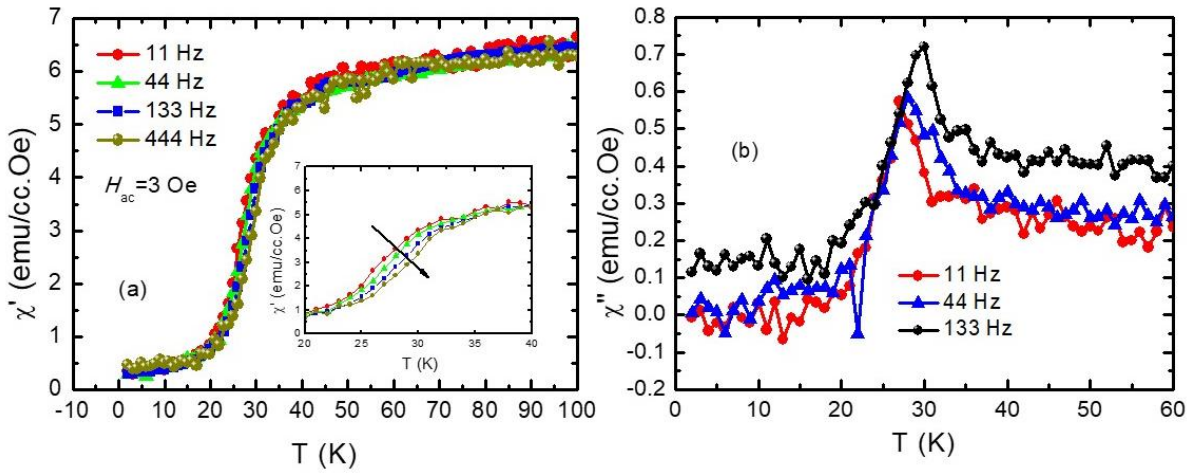


Figure 7.6: The real χ' (a) and imaginary χ'' (b) component of ac susceptibility vs temperature (T) plots at different frequencies of sample A5.

In ac-susceptibility measurements, there are two measured quantities, (i) the magnitude of the susceptibility χ and (ii) the phase shift ϕ . In other words, one can say the presence of in-phase or real component of ac susceptibility χ' and out of phase or imaginary component of ac susceptibility χ'' . One can thus write the expressions of χ' and χ'' as²⁰⁹;

$$\chi' = \chi \cos \phi,$$

$$\chi'' = \chi \sin \phi$$

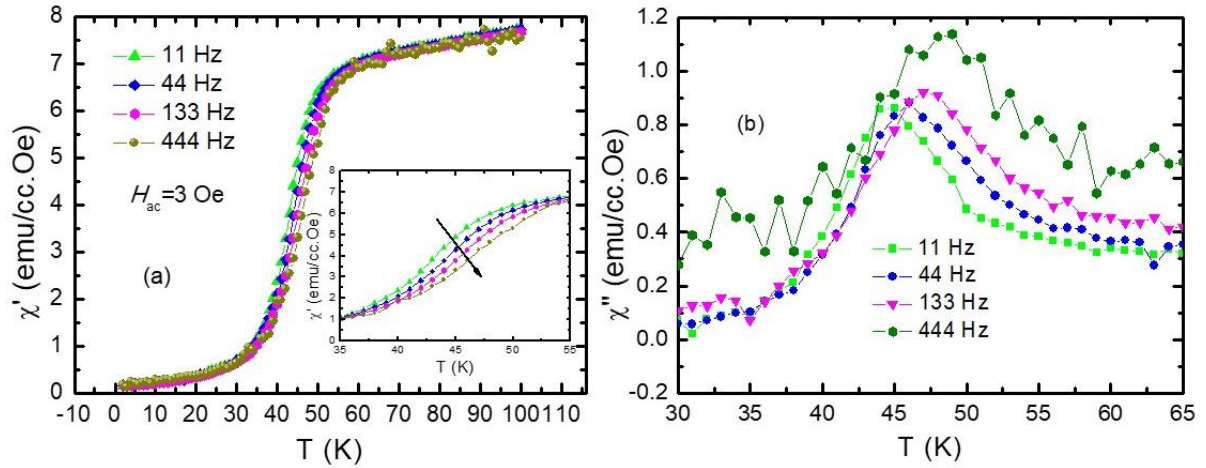


Figure 7.7: The real χ' (a) and imaginary χ'' (b) component of ac susceptibility vs temperature (T) plots at different frequencies of sample A10.

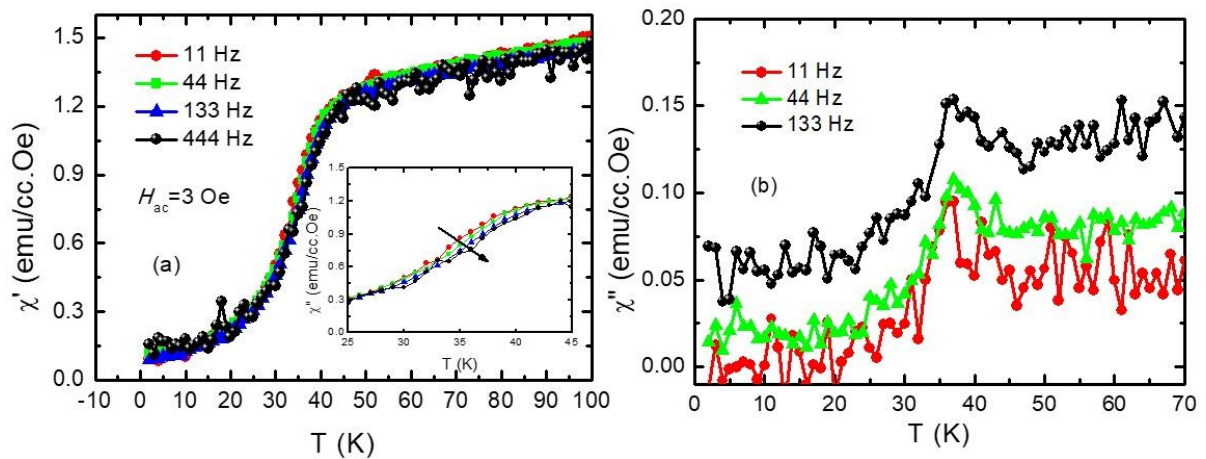


Figure 7.8: The real χ' (a) and imaginary χ'' (b) component of ac susceptibility vs temperature (T) plots at different frequencies of sample A15.

T_f has shifted from ~ 26 K at 11 Hz frequency to ~ 30 K at 444 Hz frequency in sample A5. In sample A10, T_f shifts from ~ 43 K at 11 Hz frequency to ~ 46 K at 444 Hz frequency. In sample A15, T_f gets shifted from ~ 34 K at 11 Hz frequency to ~ 37 K at 444 Hz frequency. Thus, T_f shifts to a higher temperature with increase in frequency.

In case of non-interacting systems such as superparamagnets (SPM), one can use Néel-

Arrhenius (N-A) model to determine the relaxation of SPMs. The N-A model is described by the equation below²¹⁰;

$$\nu = \nu_0 \exp(-E_a/k_B T) \quad \dots\dots\dots (7.4)$$

Where, ν is the rate of flipping of magnetization between the two lowest energy states, an attempt frequency is defined as ν_0 whose value for superparamagnets lies between 10^8 to 10^{12} Hz^{210,211}. k_B is the Boltzmann constant.

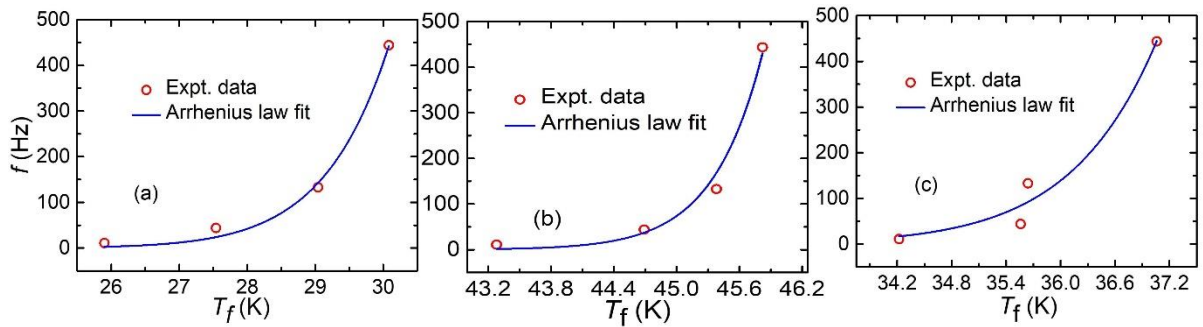


Figure 7.9: (a)-(c) the red open circles are the experimental data points and blue solid line is the fitted data using Néel-Arrhenius (N-A) law of the samples A5, A10 and A15, respectively.

The values of ν_0 are found to be larger than the ν_0 values of the superparamagnets. E_a/k_B values indicate the existence of spin-glass phase²¹⁰. To find the nature of the interaction, the T_f vs f data are fitted using Vogel-Fulcher (V-F) model.

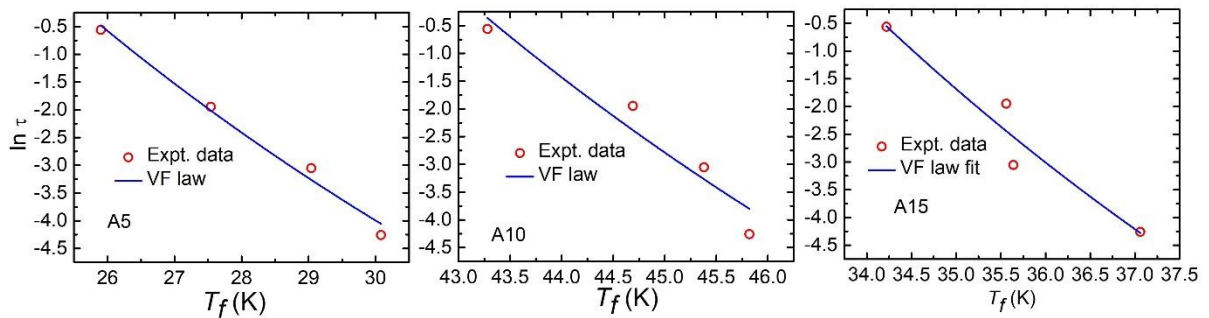


Figure 7.10: (a)-(c) the plots of T_f vs $\ln \tau$ of the samples A5, A10 and A15, respectively. The red open circles are the experimental data points and blue solid line is the fitted data using V-F law.

Vogel-Fulcher (V-F) model is generally considered for exploring the collective nature of the spins in a magnetic system and is given as²¹²⁻²¹⁴;

$$\tau = \tau_0 \exp\left(\frac{E_{VF}}{k_B(T_f - T_{VF})}\right) \dots\dots\dots (7.5)$$

Where, E_{VF} is the activation energy and Vogel-Fulcher temperature, T_{VF} , is a measure of the interaction strength.

The value of τ_0 for a spin glass or cluster spin glass system lies in-between 10^{-12} to 10^{-14} s²¹².

Figure 7.10 shows the fit of T_f vs $\ln \tau$.

The value of τ_0 obtained (table 7.3) from V-F law is similar to spin glass systems. Further, we have observed the memory effect in the zero field cooled magnetization which clearly evidence the spin glass state in the sample. Therefore, the existence of superparamagnetic behaviour is excluded.

All the parameters obtained after fitting equations 7.4, and 7.5 are given in table 7.3.

Table 7.3: Fitting parameters obtained using equations 7.4, and 7.5 of all the samples.

Samples	N-A Model		V-F law		
	ν_0 (Hz)	E_a/k_B (K)	τ_0 (s)	E_{VF}/k_B (K)	T_{VF} (K)
A5	$2.44 \times 10^{16} \pm 7.22 \times 10^{14}$	951.88 ± 111.90	4.66×10^{-12} $\pm 6.91 \times 10^{-13}$	657.73 ± 53.12	0.20 ± 0.10
A10	$4.17 \times 10^{44} \pm 2.06 \times 10^{43}$	4429.30 ± 439.71	9.61×10^{-13} $\pm 9.35 \times 10^{-14}$	479.93 ± 90.07	25.71 ± 1.73
A15	$5.88 \times 10^{19} \pm 4.22 \times 10^{18}$	1461.04 ± 2.92	3.19×10^{-12} $\pm 3.26 \times 10^{-13}$	438.74 ± 83.32	17.29 ± 1.71

7.6: Conclusions:

We found that the peak temperature (T_P), obtained from ZFC MT plot, increases with increase in thickness of NiMn layer. Temperature and cooling field dependence of EB indicates the presence of a spin glass phase. Sign change of exchange bias has been observed for some thickness of NiMn which is mainly due to indirect exchange coupling between the ‘bulk’

NiMn and interface spins. The training effect data is fitted using spin configurational relaxation model, and frozen and rotatable spin relaxation model. The presence of spin glass phase is confirmed from the fitting of the ac susceptibility data using V-F model. The variation of H_{EB} with the thickness of NiMn indicates the contribution of 'bulk' part of the AFM to EB in NiMn/Co₄₀Fe₄₀B₂₀ films.

Chapter 8: Summary and outlook:

The motivation in this thesis was to study the static and dynamic magnetic properties of ferromagnetic hard/soft and ferromagnetic/antiferromagnetic bilayers. Various fabrication methodologies have been utilized to tune the magnetic properties of hard/soft ferromagnetic layers. The exchange coupling at the interface of ferromagnetic layers has the important role tuning the magnetic properties. In the later part of this study of exchange bias in FM/AFM bilayers, we found that disorder and frustration plays a very important role in tuning the magnetic properties.

The dc magnetron sputtering method is used to fabricate Co (soft), CoFeB (hard) ferromagnetic single layers and Co/CoFeB bilayers. MOKE based microscopy, and FMR spectroscopy are the mostly used characterization techniques to study the soft and hard ferromagnetic bilayers. The magnetic bilayers are deposited in parallel (\parallel) and perpendicular (\perp) configuration. The Co/CoFeB bilayers have the magnetic domains which is the combined effect of single layers due to the exchange coupling between them. The H_C of the magnetic bilayers is higher than single Co layer whereas lesser than single CoFeB layer. Thus, the magnetic hardness of CoFeB is responsible for the enhancement of coercivity in the magnetic bilayers. The tuning of coercivity is achieved by using different deposition methodologies such as \parallel and \perp configuration. It is also found that α of the magnetic bilayer is higher than the single layers. Thus, the exchange coupling between the magnetic layers and the high magnetic anisotropy of hard magnetic layer are responsible for the enhancement of damping constant α . Magnetic bilayer deposited in \parallel configuration has lower value of α than the magnetic bilayer deposited in \perp configuration due to its higher interface roughness.

Co/CoFeB magnetic bilayers are fabricated with various thicknesses and alternate the order of magnetic layers to investigate the static and dynamic magnetic properties. The magnetic anisotropy energy (K_U) is relatively high for the magnetic bilayers with higher thickness of

Co. The interfacial exchange coupling is responsible for the tuning of the magnetic anisotropy energy (K_U). The saturation magnetization (M_S) is also higher by increasing the thickness of soft Co magnetic layer. It is found that the magnetic domains type and size have been modified by increasing the thickness of Co and also in the magnetic bilayers where CoFeB is at the bottom. Different values of coercivity are found by using this deposition methodologies. Due to the increase in interfacial exchange coupling, the coercivity is higher in magnetic bilayer with larger thickness of Co and for the bilayer in which CoFeB is at the bottom. Uniaxial anisotropy is found in some samples and combination of uniaxial and six-fold anisotropies in some samples due to the oblique angle of deposition in our sputtering system. The increased interfacial exchange coupling is also responsible for the enhancement in the value of damping constant. The correlation between the inhomogeneous linewidth broadening ΔH_0 and damping constant α is also found. Perpendicular surface anisotropy constant K_S values have been calculated using the magnetization values obtained from SQUID and FMR for all the samples and different values of K_S have been found for all the samples.

The static and dynamic magnetic properties of Co, CoFeB single magnetic layers and bilayers have been studied which are deposited without seed layer, at 20 rpm speed of substrate and in different deposition pressures. With these above deposition conditions, it is found that Co is relatively harder than CoFeB layer due to change in microstructure. Labyrinth and ripple types of magnetic domains have been found in the bilayers due to the interfacial exchange coupling between the single layers. The magnetic bilayers have H_C , M_S and K_U values higher than CoFeB but lesser than Co single layer due to exchange coupling between them and magnetic hardness of Co is also responsible for the enhancement of H_C in the bilayers. Decrease in M_S has been found with increase in deposition pressure. The increase in deposition pressure results inner (compressive or tensile) stress in the magnetic thin films that tunes the magnetic dynamic properties. The tuning of α , H_{Keff} , g-factor and $4\pi M_{eff}$ values is found with the deposition

pressure. The tuning of α , $H_{K\text{eff}}$ and $4\pi M_{\text{eff}}$ values is also found by direct exchange coupling between the magnetic Co and CoFeB single layers. Thus, we found that the interfacial exchange coupling and deposition pressure have the effect on static and dynamic magnetic properties.

The soft (NiFe) and hard (Fe) magnetic bilayers are also fabricated by dc magnetron sputtering method. The Kerr magnetometry revealed the large change of coercivity and H_K values by alternating the order of magnetic layers. Smaller magnetic domains away from easy axis is found in the bilayer with higher uniaxial magnetic anisotropy. FMR angle dependent measurement revealed the presence of uniaxial magnetic anisotropy in all the samples. It has been previously reported that high exchange coupling leads to an increase in damping constant α but in the present study of these Fe/NiFe samples, the damping constant α is similar to the single layers. From PNR measurement, the high value of inter-diffusion layer thickness and magnetic moment are found at the Fe-NiFe interface of the magnetic bilayer with high value of H_C . The high exchange coupling between the magnetic layers might be a reason for the enhancement of coercivity and anisotropy field H_K .

In the last two chapters, the static and dynamic magnetic properties of FM/AFM bilayers were studied. The exchange coupling between the FM and AFM develops unidirectional anisotropy at the interface which gives exchange bias effect. Temperature and cooling field dependence of exchange bias have been performed to investigate the magnetic nature of the interface. The exponential decay of H_{EB} and H_C with temperature indicates the presence of spin glass state at the interface. Sharp rise of H_{EB} is found below 50 K in the temperature dependent study due to contribution of frozen spin glass. Further, H_{EB} decreases with the increase in cooling field similar to a FM/SG system. The training effect data are fitted using spin configurational relaxation model and frozen and rotatable spin relaxation model to confirm the presence of spin glass like interface. The variation of exchange bias field is found to increase in IrMn

thickness indicating the contribution of ‘bulk’ part of AFM to exchange bias.

Exchange bias in NiMn/CoFeB systems have also been studied. In these systems, Ta/Pt is deposited as buffer layer to induce AFM order without doing post deposition annealing. The sign change of exchange bias is observed, in some of the bilayers, near to the compensation temperature T_0 due to the indirect exchange coupling between the ‘bulk’ NiMn and interface spins. The exponential decay of coercivity is found in all the samples. The decrease of exchange bias field H_{EB} is found with increase in cooling field H_{FC} whereas coercivity remains constant which is generally observed in FM/SG system. The training effect data have been fitted with spin configurational relaxation model and frozen and rotatable spin relaxation model confirming the presence of spin glass like interface. For further confirmation of the presence of spin glass phase, ac susceptibility measurements have been performed. The peak temperature T_f (obtained from ac susceptibility measurements) vs frequency f data are fitted using Neel-Arrhenius (N-A) model and Vogel-Fulcher (V-F) law to know if the system is non-interacting like superparamagnets or interacting like spin glass system.

One can also study the magnetic properties of the discussed soft/hard bilayers by placing very thin Cu layer of various thicknesses at the interface such that the interfacial exchange coupling gets modified. One can do post deposition annealing at various temperatures in the Co/CoFeB bilayers to tune the interfacial exchange coupling and hence the energy product $(BH)_{max}$ value. Also, one can systematically increase the thickness of soft and hard magnetic layers in the above soft/hard bilayers to investigate the effect of it on the magnetic properties. It would be interesting to systematically increase the deposition pressure from ultra-low pressure to high pressure to study the effect on static and dynamic properties.

In this thesis work, the Fe/IrMn samples are prepared with 0 rpm rotation speed of substrate which gives growth induced uniaxial magnetic anisotropy in all the bilayers. One can compare the exchange bias results obtained using 0 and 20 rpm speed of the substrate. Also, one can

insert an interface layer such as Cu of different thicknesses in between the FM and AFM layers to study the effect of the modification of interfacial exchange coupling on the EB.

Understanding of these aspects will have significant impact for future spintronic based application.

References:

1. Schmid, I. The role of uncompensated spins in exchange biased systems. (University_of_Basel, 2008).
2. Radu, F. Fundamental aspects of exchange bias effect in AF/F bilayers and multilayers. (2005).
3. Fullerton, E. E., Jiang, J. S. & Bader, S. D. Hard/soft magnetic heterostructures: model exchange-spring magnets. *J. Magn. Mater.* **200**, 392–404 (1999).
4. Jiang, J. S., Fullerton, E. E., Grimsditch, M., Sowers, C. H. & Bader, S. D. Exchange-spring behavior in epitaxial hard/soft magnetic bilayer films. *J. Appl. Phys.* **83**, 6238 (1998).
5. Fullerton, E. E., Jiang, J. S., Grimsditch, M., Sowers, C. H. & Bader, S. D. Exchange-spring behavior in epitaxial hard/soft magnetic bilayers. *Phys. Rev. B* **58**, 12193–12200 (1998).
6. Kim, J., Barmak, K., De Graef, M., Lewis, L. H. & Crew, D. C. Effect of annealing on magnetic exchange coupling in CoPt/Co bilayer thin films. *J. Appl. Phys.* **87**, 6140–6142 (2000).
7. Zhang, J., Takahashi, Y. K., Gopalan, R. & Hono, K. Sm(Co,Cu)5Fe exchange spring multilayer films with high energy product. *Appl. Phys. Lett.* **86**, 122509 (2005).
8. Davies, J. E. *et al.* Anisotropy dependence of irreversible switching in FeSmCo and FeNiFePt exchange spring magnet films. *Appl. Phys. Lett.* **86**, 262503 (2005).
9. Fullerton, E. E., Jiang, J. S., Sowers, C. H., Pearson, J. E. & Bader, S. D. Structure and magnetic properties of exchange-spring Sm–Co/Co superlattices. *Appl. Phys. Lett.* **72**, 380–382 (1998).
10. Hellwig, O., Kortright, J. B., Takano, K. & Fullerton, E. E. Switching behavior of Fe-Pt/Ni-Fe exchange-spring films studied by resonant soft-x-ray magneto-optical Kerr effect. *Phys. Rev. B* **62**, 11694–11698 (2000).
11. Conca, A. *et al.* Low spin-wave damping in amorphous Co₄₀Fe₄₀B₂₀ thin films. *J. Appl. Phys.* **113**, 213909 (2013).
12. Berkowitz, A. E. & Takano, K. Exchange anisotropy — a review. *J. Magn. Mater.* **200**, 552–570 (1999).
13. Stamps, R. L. Mechanisms for exchange bias. *J. Phys. Appl. Phys.* **33**, R247–R268 (2000).
14. Radu, F. & Zabel, H. Exchange Bias Effect of Ferro-/Antiferromagnetic Heterostructures. in

- Magnetic Heterostructures: Advances and Perspectives in Spinstructures and Spintransport* (eds. Zabel, H. & Bader, S. D.) 97–184 (Springer, 2008). doi:10.1007/978-3-540-73462-8_3.
15. Nogués, J. *et al.* Exchange bias in nanostructures. *Phys. Rep.* **422**, 65–117 (2005).
 16. Spizzo, F., Tamisari, M., Chinni, F., Bonfiglioli, E. & Del Bianco, L. Interface adjustment and exchange coupling in the IrMn/NiFe system. *J. Magn. Magn. Mater.* **421**, 234–240 (2017).
 17. Exchange interaction.
[https://physweb.bgu.ac.il/COURSES/LAB_C/Susc/EXCHANGE_INTERACTION\[1\].doc](https://physweb.bgu.ac.il/COURSES/LAB_C/Susc/EXCHANGE_INTERACTION[1].doc).
 18. *Mathias Getzlaff, Fundamentals of Magnetism.*
 19. Hubert, A. & Schäfer, R. Domain Theory. in *Magnetic Domains: The Analysis of Magnetic Microstructures* (eds. Hubert, A. & Schäfer, R.) 99–335 (Springer, 1998). doi:10.1007/978-3-540-85054-0_3.
 20. 1.1.4.1 Uniaxial anisotropy, http://wpage.unina.it/mdaquino/PhD_thesis/main/node12.html.
http://wpage.unina.it/mdaquino/PhD_thesis/main/node12.html.
 21. Cullity, B. D. & Graham, C. D. *Introduction to Magnetic Materials*. (John Wiley & Sons, 2011).
 22. Maciej Urbaniak, Magnetic anisotropy,
http://www.ifmpan.poznan.pl/~urbaniak/Wyklady2012/urbifmpan2012lect5_03.pdf.
 23. Magnetic domains, <https://www.phase-trans.msm.cam.ac.uk/2003/Vicky.Yardley/Chapter03.pdf>.
 24. Guimarães, A. P. *Principles of Nanomagnetism*. (Springer-Verlag, 2009). doi:10.1007/978-3-642-01482-6.
 25. 4.3.6 Hard and Soft Magnets, https://www.tf.uni-kiel.de/matwis/amat/elmat_en/kap_4/backbone/r4_3_6.html. https://www.tf.uni-kiel.de/matwis/amat/elmat_en/kap_4/backbone/r4_3_6.html.
 26. Meiklejohn, W. H. & Bean, C. P. New Magnetic Anisotropy. *Phys. Rev.* **102**, 1413–1414 (1956).
 27. Meiklejohn, W. H. & Bean, C. P. New Magnetic Anisotropy. *Phys. Rev.* **105**, 904–913 (1957).

28. Meiklejohn, W. H. Exchange Anisotropy—A Review. *J. Appl. Phys.* **33**, 1328–1335 (1962).
29. Nogués, J. & Schuller, I. K. Exchange bias. *J. Magn. Magn. Mater.* **192**, 203–232 (1999).
30. R. Coehoorn, Lecture Notes Eindhoven University of Technology (2000-2001).
31. Miltényi, P. *et al.* Diluted Antiferromagnets in Exchange Bias: Proof of the Domain State Model. *Phys. Rev. Lett.* **84**, 4224–4227 (2000).
32. Beckmann, B., Nowak, U. & Usadel, K. D. Asymmetric Reversal Modes in Ferromagnetic/Antiferromagnetic Multilayers. *Phys. Rev. Lett.* **91**, 187201 (2003).
33. Nowak, U., Misra, A. & Usadel, K. D. Domain state model for exchange bias. *J. Appl. Phys.* **89**, 7269–7271 (2001).
34. Nowak, U. *et al.* Domain state model for exchange bias. I. Theory. *Phys. Rev. B* **66**, 014430 (2002).
35. Misra, A., Nowak, U. & Usadel, K. D. Control of exchange bias by diluting the antiferromagnetic layer. *J. Appl. Phys.* **93**, 6593–6595 (2003).
36. Misra, A., Nowak, U. & Usadel, K. D. Structure of domains in an exchange-bias model. *J. Appl. Phys.* **95**, 1357–1363 (2004).
37. Binder, K. & Young, A. P. Spin glasses: Experimental facts, theoretical concepts, and open questions. *Rev. Mod. Phys.* **58**, 801–976 (1986).
38. Radu, F., Westphalen, A., Theis-Bröhl, K. & Zabel, H. Quantitative description of the azimuthal dependence of the exchange bias effect. *J. Phys. Condens. Matter* **18**, L29–L36 (2005).
39. Swann, S. Magnetron sputtering. *Phys. Technol.* **19**, 67–75 (1988).
40. Thin Film Deposition, https://www.ndsu.edu/pubweb/~qifzhang/Tech_Sputter-01.pdf.
41. Fatin Fatimah Binti Zahari, Electron Beam Evaporation, <https://missinglilo.files.wordpress.com/2012/04/een3106.pdf>.
42. http://users.wfu.edu/ucerkb/Nan242/L07-Sputtering_a.pdf.
43. Kelly, P. J. & Arnell, R. D. Magnetron sputtering: a review of recent developments and applications. *Vacuum* **56**, 159–172 (2000).
44. Andreea, M. *Crystallization: Science and Technology*. (BoD – Books on Demand, 2012).
45. Mantis deposition system, <https://www.mantisdeposition.com/systems/view/info/qprep->

series.html.

46. Bouroushian, M. & Kosanovic, T. Characterization of thin films by low incidence X-ray diffraction. *Cryst Struct Theory Appl* **1**, 35–39 (2012).
47. Parratt, L. G. Surface Studies of Solids by Total Reflection of X-Rays. *Phys. Rev.* **95**, 359–369 (1954).
48. Névot, L. & Croce, P. Caractérisation des surfaces par réflexion rasante de rayons X. Application à l'étude du polissage de quelques verres silicates. *Rev. Phys. Appliquée* **15**, 761–779 (1980).
49. Fujii, Y., Nakayama, T. & Yoshida, K. Roughness Estimation of Polycrystalline Iron Surface under High Temperature by Small Glancing Angle X-ray Scattering. *ISIJ Int.* **44**, 1549–1553 (2004).
50. Fujii, Y., Komai, T. & Ikeda, K. Depth profiling of polycrystalline layers under a surface using x-ray diffraction at small glancing angle of incidence. *Surf. Interface Anal.* **37**, 190–193 (2005).
51. Fujii, Y. Influence of surface roughness on near-surface depth analysis from X-ray reflectivity measurements. *Surf. Interface Anal.* **42**, 1642–1645 (2010).
52. Fujii, Y. Comparison of Surface Roughness Estimations by X-ray Reflectivity Measurements and TEM observations. *IOP Conf. Ser. Mater. Sci. Eng.* **24**, 012008 (2011).
53. Holy, V., Pietsch, U., and Baumbach, T. (Eds.), 1999, *High-Resolution X-ray Scattering from Thin Films and Multilayers* (Berlin Springer).
54. Holy, V., Kuběna, J., Ohlídal, I., Lischka, K. & Plotz, W. X-ray reflection from rough layered systems. *Phys. Rev. B* **47**, 15896–15903 (1993).
55. Yasaka, M. X-ray thin-film measurement techniques V . X-ray reflectivity measurement. in (2010).
56. Good Diffraction Practice Webinar Series, Bruker AXS, https://www.bruker.com/fileadmin/user_upload/webinars/XRD/presentations/Bruker_AXS_Good_Diffraction_Practice_II_-_Two-Dimensional_XRD.pdf.
57. Zabel, H. X-ray and neutron reflectivity analysis of thin films and superlattices. *Appl. Phys.*

- A **58**, 159–168 (1994).
58. Reflectometry with X-rays and Neutrons, T. Gutberlet LNS, PSI & ETHZ, Villigen, <https://www.psi.ch/sites/default/files/import/sinq/amor/ManualsEN/Zuoz2006.pdf>.
 59. Gilbert, T. L. A phenomenological theory of damping in ferromagnetic materials. *IEEE Trans. Magn.* **40**, 3443–3449 (2004).
 60. Woltersdorf, G. & Heinrich, B. Two-magnon scattering in a self-assembled nanoscale network of misfit dislocations. *Phys. Rev. B* **69**, 184417 (2004).
 61. Chapter 8, Magnetic Resonance, <https://www.tcd.ie/Physics/research/groups/magnetism/files/lectures/5006/5006-9.pdf>.
 62. Kittel, C. On the Theory of Ferromagnetic Resonance Absorption. *Phys. Rev.* **73**, 155–161 (1948).
 63. FMR Spectrometer NanoOsc, <https://www.qdusa.com/products/nanosc-fmr-spectrometers.html>.
 64. Fagaly, R. L. Superconducting quantum interference device instruments and applications. *Rev. Sci. Instrum.* **77**, 101101 (2006).
 65. Bedanta, S. Supermagnetism in magnetic nanoparticle systems. (2007).
 66. Bedanta, S., Petravic, O., Aderholz, M. & Kleemann, W. A sample holder design for high temperature measurements in superconducting quantum interference device magnetometers. *Rev. Sci. Instrum.* **76**, 083910 (2005).
 67. SQUID Magnetometer and Josephson Junctions, <http://hyperphysics.phy-astr.gsu.edu/hbase/Solids/Squid.html>. <http://hyperphysics.phy-astr.gsu.edu/hbase/Solids/Squid.html>.
 68. Kraft, A., Rupprecht, C. & Yam, Y.-C. *Superconducting Quantum Interference Device (SQUID)*. (PHYSICS, 2017).
 69. SQUID Quantum Design, <https://www.qdusa.com/company/index.html>.
 70. Haider, T. A review of magneto-optic effects and its application. *Int. J. Electromagn. Appl.* **7**, 17–24 (2017).
 71. Lacheisserie, E. D. T. de, Fourier, U. J., Gignoux, D. & Schlenker, M. *Magnetism*. (Springer

Science & Business Media, 2005).

72. Magneto-optical microscopy (incl. time-resolved), J. McCord (abstract in cooperation with R. Schäfer), IFW Dresden - Institute for Metallic Materials, <http://magnetism.eu/esm/2005-constant/abs/mccord-abs.pdf>.
73. Kerr Microscope Evico Magnetics, <http://www.evico-magnetics.de/>.
74. Roger Pynn, Neutron Reflectometry, Indiana University and the Spallation Neutron Source, <https://cpb-us-w2.wpmucdn.com/sites.udel.edu/dist/4/1563/files/2014/03/Reflectometry-2cpzs6j.pdf>.
75. J.R.P.Webster, Introduction to Neutron Reflectivity, ISIS Facility, Rutherford Appleton Laboratory, <https://www.isis.stfc.ac.uk/Pages/neutron-reflectivity---introduction12224.pdf>.
76. Ankner, J. F. & Felcher, G. P. Polarized-neutron reflectometry. *J. Magn. Magn. Mater.* **200**, 741–754 (1999).
77. Chowdhury, N. & Bedanta, S. Controlling the anisotropy and domain structure with oblique deposition and substrate rotation. *AIP Adv.* **4**, 027104 (2014).
78. Fang, Y.-P. *et al.* Surface morphology and magnetic anisotropy of obliquely deposited Co/Si(111) films. *Appl. Phys. Lett.* **97**, 022507 (2010).
79. Smith, D. O., Cohen, M. S. & Weiss, G. P. Oblique-Incidence Anisotropy in Evaporated Permalloy Films. *J. Appl. Phys.* **31**, 1755–1762 (1960).
80. Knorr, T. G. & Hoffman, R. W. Dependence of Geometric Magnetic Anisotropy in Thin Iron Films. *Phys. Rev.* **113**, 1039–1046 (1959).
81. Hoshi, Y., Suzuki, E. & Naoe, M. Uniaxial magnetic anisotropy of iron thin films deposited by oblique incidence of deposition particles. *J. Appl. Phys.* **79**, 4945–4947 (1996).
82. Fukuma, Y. *et al.* Strong uniaxial magnetic anisotropy in CoFe films on obliquely sputtered Ru underlayer. *J. Appl. Phys.* **106**, 076101 (2009).
83. Takahashi, M. & Kōno, T. Magnetic Annealing of Co and Co–Ni Alloys. *J. Phys. Soc. Jpn.* **15**, 936–937 (1960).
84. Park, E. B., Jang, S.-U., Kim, J.-H. & Kwon, S.-J. Induced magnetic anisotropy and strain in permalloy films deposited under magnetic field. *Thin Solid Films* **520**, 5981–5984 (2012).

85. Bedanta, S. *et al.* Overcoming the Dipolar Disorder in Dense CoFe Nanoparticle Ensembles: Superferromagnetism. *Phys. Rev. Lett.* **98**, 176601 (2007).
86. Chuang, D. S., Ballentine, C. A. & O'Handley, R. C. Surface and step magnetic anisotropy. *Phys. Rev. B* **49**, 15084–15095 (1994).
87. Wu, Y. Z., Won, C. & Qiu, Z. Q. Magnetic uniaxial anisotropy of Fe films grown on vicinal Ag(001). *Phys. Rev. B* **65**, 184419 (2002).
88. Bertelli, T. P. *et al.* Magnetic anisotropy of Co thin films: Playing with the shadowing effect, magnetic field and substrate spinning. *J. Magn. Magn. Mater.* **426**, 636–640 (2017).
89. Phuoc, N. N. & Ong, C. K. Anomalous Temperature Dependence of Magnetic Anisotropy in Gradient-Composition Sputtered Thin Films. *Adv. Mater.* **25**, 980–984 (2013).
90. Umlor, M. T. Uniaxial magnetic anisotropy in cobalt films induced by oblique deposition of an ultrathin cobalt underlayer. *Appl. Phys. Lett.* **87**, 082505 (2005).
91. Song, H.-S. *et al.* Relationship between Gilbert damping and magneto-crystalline anisotropy in a Ti-buffered Co/Ni multilayer system. *Appl. Phys. Lett.* **103**, 022406 (2013).
92. Xu, F., Huang, Q., Liao, Z., Li, S. & Ong, C. K. Tuning of magnetization dynamics in sputtered CoFeB thin film by gas pressure. *J. Appl. Phys.* **111**, 07A304 (2012).
93. Phuoc, N. N., Xu, F. & Ong, C. K. Tuning magnetization dynamic properties of Fe–SiO₂ multilayers by oblique deposition. *J. Appl. Phys.* **105**, 113926 (2009).
94. Omelchenko, P., Montoya, E. A., Coutts, C., Heinrich, B. & Girt, E. Tunable magnetization and damping of sputter-deposited, exchange coupled Py|Fe bilayers. *Sci. Rep.* **7**, 1–8 (2017).
95. Tang, M. *et al.* Magnetic damping and perpendicular magnetic anisotropy in Pd-buffered [Co/Ni]₅ and [Ni/Co]₅ multilayers. *RSC Adv.* **7**, 5315–5321 (2017).
96. Nayak, S., Mallick, S., Singh, B. B. & Bedanta, S. Effect of sputtered flux direction on damping properties in magnetic bilayers. *J. Phys. Appl. Phys.* **51**, 055008 (2018).
97. Singh, B. B., Jena, S. K. & Bedanta, S. Study of spin pumping in Co thin film vis-à-vis seed and capping layers using ferromagnetic resonance spectroscopy. *J. Phys. Appl. Phys.* **50**, 345001 (2017).
98. Heinrich, B. *et al.* Ferromagnetic-resonance study of ultrathin bcc Fe(100) films grown

- epitaxially on fcc Ag(100) substrates. *Phys. Rev. Lett.* **59**, 1756–1759 (1987).
99. Bilzer, C. *et al.* Study of the dynamic magnetic properties of soft CoFeB films. *J. Appl. Phys.* **100**, 053903 (2006).
100. Zhang, D. *et al.* Extremely Large Magnetization and Gilbert Damping Modulation in NiFe/GeBi Bilayers. *ACS Appl. Electron. Mater.* (2020) doi:10.1021/acsaelm.9b00735.
101. Conca, A. *et al.* Annealing influence on the Gilbert damping parameter and the exchange constant of CoFeB thin films. *Appl. Phys. Lett.* **104**, 182407 (2014).
102. Oogane, M. *et al.* Magnetic Damping in Ferromagnetic Thin Films. *Jpn. J. Appl. Phys.* **45**, 3889 (2006).
103. Layadi, A. A theoretical investigation of Ferromagnetic Resonance Linewidth and damping constants in coupled trilayer and spin valve systems. *AIP Adv.* **5**, 057113 (2015).
104. Lindner, J., Kollonitsch, Z., Kosubek, E., Farle, M. & Baberschke, K. In situ detection of two ferromagnetic resonance modes in coupled Ni/Cu/Co/Cu(001) trilayer structures. *Phys. Rev. B* **63**, 094413 (2001).
105. Rementer, C. R. *et al.* Tuning static and dynamic properties of FeGa/NiFe heterostructures. *Appl. Phys. Lett.* **110**, 242403 (2017).
106. Liu, W. *et al.* Structure and magnetic properties of sputtered hard/soft multilayer magnets. *J. Appl. Phys.* **93**, 8131–8133 (2003).
107. Liu, W. *et al.* The effects of the thickness of magnetically hard- and soft-phase layers on magnetic properties and exchange coupling in multilayer magnets. *J. Appl. Phys.* **97**, 10K303 (2005).
108. Haldar, A., Banerjee, C., Laha, P. & Barman, A. Brillouin light scattering study of spin waves in NiFe/Co exchange spring bilayer films. *J. Appl. Phys.* **115**, 133901 (2014).
109. Jain, S. K., Chittari, B. L. & Kumar, V. Optimum thickness of soft magnetic phase in FePt/FeCo permanent magnet superlattices with high energy product and large magnetic anisotropy energy. *AIP Adv.* **6**, 025027 (2016).
110. Wang, W., Chai, G. & Xue, D. Thickness dependent optical mode ferromagnetic resonance in Co/FeNi bilayer. *J. Phys. Appl. Phys.* **50**, 365003 (2017).

111. Lavorato, G., Winkler, E., Rivas-Murias, B. & Rivadulla, F. Thickness dependence of exchange coupling in epitaxial $\text{Fe}_3\text{O}_4/\text{CoFe}_2\text{O}_3$ soft/hard magnetic bilayers. *Phys. Rev. B* **94**, 054405 (2016).
112. Mallick, S. *et al.* Tuning the anisotropy and domain structure of Co films by variable growth conditions and seed layers. *J. Phys. Appl. Phys.* **51**, 275003 (2018).
113. Liu, Y. *et al.* Magnetic structure in Fe/Sm-Co exchange spring bilayers with intermixed interfaces. *Phys. Rev. B* **83**, 174418 (2011).
114. Lenz, K. *et al.* Two-magnon scattering and viscous Gilbert damping in ultrathin ferromagnets. *Phys. Rev. B* **73**, 144424 (2006).
115. Rantschler, J. O. *et al.* Surface anisotropy of permalloy in NM/NiFe/NM multilayers. *J. Appl. Phys.* **97**, 10J113 (2005).
116. Xu, F., Huang, Q., Liao, Z., Li, S. & Ong, C. K. Tuning of magnetization dynamics in sputtered CoFeB thin film by gas pressure. *J. Appl. Phys.* **111**, 07A304 (2012).
117. Liu, B. *et al.* The effect of growth sequence on magnetization damping in Ta/CoFeB/MgO structures. *J. Magn. Magn. Mater.* **450**, 65–69 (2018).
118. Jhajhria, D., Pandya, D. K. & Chaudhary, S. Influence of the thickness of an antiferromagnetic IrMn layer on the static and dynamic magnetization of weakly coupled CoFeB/IrMn/CoFeB trilayers. *Beilstein J. Nanotechnol.* **9**, 2198–2208 (2018).
119. Tang, M. *et al.* Ferromagnet structural tuning of interfacial symmetry breaking and spin Hall angle in ferromagnet/heavy metal bilayers. *Appl. Phys. Lett.* **113**, 222406 (2018).
120. Tang, X. *et al.* Improving the high-frequency magnetic properties of as-deposited CoFe films by ultra-low gas pressure. *J. Mater. Sci.* **53**, 3573–3580 (2018).
121. Wang, H., Du, C., Chris Hammel, P. & Yang, F. Spin current and inverse spin Hall effect in ferromagnetic metals probed by Y₃Fe₅O₁₂-based spin pumping. *Appl. Phys. Lett.* **104**, 202405 (2014).
122. Xu, F. *et al.* Tuning of the magnetization dynamics in as-sputtered FeCoSiN thin films by various sputtering gas pressures. *J. Appl. Phys.* **104**, 093903 (2008).

123. Xu, F., Liao, Z., Huang, Q., Ong, C. K. & Li, S. Influence of Sputtering Gas Pressure on High-Frequency Soft Magnetic Properties of FeCoN Thin Film. *IEEE Trans. Magn.* **47**, 3921–3923 (2011).
124. Jung, H. S., Doyle, W. D., Wittig, J. E., Al-Sharab, J. F. & Bentley, J. Soft anisotropic high magnetization Cu/FeCo films. *Appl. Phys. Lett.* **81**, 2415–2417 (2002).
125. Fu, Y., Cheng, X. & Yang, Z. Soft magnetic properties and microstructure of Fe₆₅Co₃₅ thin films with different underlayers. *Phys. Status Solidi A* **203**, 963–969 (2006).
126. Nayak, S., Singh, B. B., Mallick, S. & Bedanta, S. Tuning of magnetic properties by alternating the order of hard/soft bilayers with various thicknesses. *J. Phys. Appl. Phys.* **52**, 305301 (2019).
127. Tu, H. Q. *et al.* Gilbert damping in CoFeB/GaAs(001) film with enhanced in-plane uniaxial magnetic anisotropy. *Sci. Rep.* **7**, 43971 (2017).
128. Yu, R. *et al.* Determination of spin Hall angle and spin diffusion length in β -phase-dominated tantalum. *Phys. Rev. Mater.* **2**, 074406 (2018).
129. Nibarger, J. P., Lopusnik, R., Celinski, Z. & Silva, T. J. Variation of magnetization and the Landé g factor with thickness in Ni–Fe films. *Appl. Phys. Lett.* **83**, 93–95 (2003).
130. Neilinger, P. *et al.* Ferromagnetic resonance study of sputtered Pt/Co/Pt multilayers. *Appl. Surf. Sci.* **461**, 202–205 (2018).
131. Choi, Y. *et al.* Controlled interface profile in Sm–Co/Fe exchange-spring magnets. *Appl. Phys. Lett.* **91**, 072509 (2007).
132. Si, W. *et al.* Deterioration of the coercivity due to the diffusion induced interface layer in hard/soft multilayers. *Sci. Rep.* **5**, 1–9 (2015).
133. Crew, D. C., Kim, J., Lewis, L. H. & Barmak, K. Interdiffusion in bilayer CoPt/Co films: potential for tailoring the magnetic exchange spring. *J. Magn. Magn. Mater.* **233**, 257–273 (2001).
134. Wang, F., Xu, X., Liang, Y., Zhang, J. & Wu, H. FeAu/FePt exchange-spring media fabricated by magnetron sputtering and postannealing. *Appl. Phys. Lett.* **95**, 022516 (2009).
135. Fan, J. *et al.* Inserting a nonmagnetic spacer layer in Nd₂Fe₁₄B/ α' -(FeCo)₁₆N₂ bilayers significantly improves their coercivity. *Appl. Phys. A* **125**, 111 (2019).

136. Wang, J. *et al.* Structural and magnetic properties of L10-FePt/Fe exchange coupled nanocomposite thin films with high energy product. *J. Magn. Magn. Mater.* **345**, 165–170 (2013).
137. Navas, D. *et al.* Magnetization reversal and exchange bias effects in hard/soft ferromagnetic bilayers with orthogonal anisotropies. *New J. Phys.* **14**, 113001 (2012).
138. Alexandrakis, V., Niarchos, D., Wolff, M. & Panagiotopoulos, I. Magnetization reversal in CoPt(111) hard/soft bilayers. *J. Appl. Phys.* **105**, 063908 (2009).
139. Raghavendra Reddy, V., Crisan, O., Gupta, A., Banerjee, A. & Kuncser, V. Tuning exchange spring effects in FePt/Fe(Co) magnetic bilayers. *Thin Solid Films* **520**, 2184–2189 (2012).
140. Jiang, J. S. *et al.* Improving exchange-spring nanocomposite permanent magnets. *Appl. Phys. Lett.* **85**, 5293–5295 (2004).
141. Choi, Y. *et al.* Role of diffused Co atoms in improving effective exchange coupling in Sm-Co-Fe spring magnets. *Phys. Rev. B* **75**, 104432 (2007).
142. Mallik, S. *et al.* Tuning spinterface properties in iron/fullerene thin films. *Nanotechnology* **30**, 435705 (2019).
143. Mallik, S., Mattauch, S., Dalai, M. K., Brückel, T. & Bedanta, S. Effect of magnetic fullerene on magnetization reversal created at the Fe/C 60 interface. *Sci. Rep.* **8**, 1–9 (2018).
144. <https://genx.sourceforge.io/index.html>.
145. Mallik, S. & Bedanta, S. Study of anisotropy, magnetization reversal and damping in ultrathin Co films on MgO (001) substrate. *J. Magn. Magn. Mater.* **446**, 270–275 (2018).
146. Singh, S., Basu, S., Gupta, M., Vedpathakz, M. & Kodama, R. H. Investigation of interface magnetic moment of Fe/Ge multilayer: A neutron reflectivity study. *J. Appl. Phys.* **101**, 033913 (2007).
147. Kiwi, M. Exchange bias theory. *J. Magn. Magn. Mater.* **234**, 584–595 (2001).
148. Ohldag, H. *et al.* Correlation between Exchange Bias and Pinned Interfacial Spins. *Phys. Rev. Lett.* **91**, 017203 (2003).
149. Fulara, H., Chaudhary, S., Kashyap, S. C. & Granville, S. Enhancement of exchange bias and training effect in ion-beam sputtered Fe₄₆Mn₅₄/Ni₈₁Fe₁₉ bilayers. *J. Appl. Phys.* **115**, 043910

- (2014).
150. Ali, M. *et al.* Antiferromagnetic layer thickness dependence of the IrMn/Co exchange-bias system. *Phys. Rev. B* **68**, 214420 (2003).
 151. Scholl, A. *et al.* Exploring the microscopic origin of exchange bias with photoelectron emission microscopy (invited). *J. Appl. Phys.* **89**, 7266 (2001).
 152. Takano, K., Kodama, R. H., Berkowitz, A. E., Cao, W. & Thomas, G. Interfacial Uncompensated Antiferromagnetic Spins: Role in Unidirectional Anisotropy in Polycrystalline $\text{Ni}_{81}\text{Fe}_{19}/\text{CoO}$ Bilayers. *Phys. Rev. Lett.* **79**, 1130–1133 (1997).
 153. Stiles, M. D. & McMichael, R. D. Model for exchange bias in polycrystalline ferromagnet-antiferromagnet bilayers. *Phys. Rev. B* **59**, 3722–3733 (1999).
 154. Basaran, A. C. *et al.* Exchange bias: The antiferromagnetic bulk matters. *Appl. Phys. Lett.* **105**, 072403 (2014).
 155. Muhammed Shameem, P. V. & Senthil Kumar, M. Training effect of the exchange bias in sputter deposited Fe₃O₄ thin films with varying thickness. *J. Magn. Magn. Mater.* **458**, 241–252 (2018).
 156. Nam, D. N. H. *et al.* Propagation of exchange bias in CoFe/FeMn/CoFe trilayers. *Appl. Phys. Lett.* **93**, 152504 (2008).
 157. Mishra, S. K., Radu, F., Dürr, H. A. & Eberhardt, W. Training-Induced Positive Exchange Bias in NiFe/IrMn Bilayers. *Phys. Rev. Lett.* **102**, 177208 (2009).
 158. Lai, C., Matsuyama, H., White, R. L., Anthony, T. C. & Bush, G. G. Exploration of magnetization reversal and coercivity of epitaxial NiO {111}/NiFe films. *J. Appl. Phys.* **79**, 6389–6391 (1996).
 159. McCord, J. & Mangin, S. Separation of low- and high-temperature contributions to the exchange bias in $\text{Ni}_{81}\text{Fe}_{19}$ -NiO thin films. *Phys. Rev. B* **88**, 014416 (2013).
 160. McCord, J., Hamann, C., Schäfer, R., Schultz, L. & Mattheis, R. Nonlinear exchange coupling and magnetic domain asymmetry in ferromagnetic/IrMn thin films. *Phys. Rev. B* **78**, 094419 (2008).

161. Ambrose, T. & Chien, C. L. Dependence of exchange coupling on antiferromagnetic layer thickness in NiFe/CoO bilayers. *J. Appl. Phys.* **83**, 6822–6824 (1998).
162. Sang, H., Du, Y. W. & Chien, C. L. Exchange coupling in Fe₅₀Mn₅₀/Ni₈₁Fe₁₉ bilayer: Dependence on antiferromagnetic layer thickness. *J. Appl. Phys.* **85**, 4931–4933 (1999).
163. Li, H. Y., Chen, L. Y. & Zhou, S. M. Thermal stability of exchange coupling in permalloy/FeMn bilayers and its dependence on the antiferromagnetic layer thickness. *J. Appl. Phys.* **91**, 2243–2246 (2002).
164. Usadel, K. D. & Nowak, U. Exchange bias for a ferromagnetic film coupled to a spin glass. *Phys. Rev. B* **80**, 014418 (2009).
165. O’Handley, R. C. *Modern magnetic materials: principles and applications*. (Wiley, 2000).
166. Lacour, D. *et al.* Field sensing using the magnetoresistance of IrMn exchange-biased tunnel junctions. *J. Appl. Phys.* **91**, 4655–4658 (2002).
167. Pearson’s Crystal Data. <http://www.crystalimpact.com/pcd/>.
168. Weschke, E. *et al.* Finite-Size Effect on Magnetic Ordering Temperatures in Long-Period Antiferromagnets: Holmium Thin Films. *Phys. Rev. Lett.* **93**, 157204 (2004).
169. Kohn, A. *et al.* The antiferromagnetic structures of IrMn₃ and their influence on exchange-bias. *Sci. Rep.* **3**, 2412 (2013).
170. Spizzo, F., Tamisari, M., Bonfiglioli, E. & Bianco, L. D. Detection of the dynamic magnetic behavior of the antiferromagnet in exchange-coupled NiFe/IrMn bilayers. *J. Phys. Condens. Matter* **25**, 386001 (2013).
171. Cheng, S.-F. & Lubitz, P. Structural and magnetic studies of exchange bias films of Ir(20)Mn(80). *J. Appl. Phys.* **87**, 4927–4929 (2000).
172. Mishra, S. K. *et al.* Dual behavior of antiferromagnetic uncompensated spins in NiFe/IrMn exchange biased bilayers. *Phys. Rev. B* **81**, 212404 (2010).
173. Rui, W. B. *et al.* Cooling field and temperature dependent exchange bias in spin glass/ferromagnet bilayers. *Sci. Rep.* **5**, 13640 (2015).
174. Anandakumar, S., Rani, V. S., Oh, S. & Kim, C. Positive and negative exchange bias in IrMn/NiFe bilayers. *Thin Solid Films* **519**, 1020–1024 (2010).

175. Wang, C. *et al.* Exchange bias in spin-glass-like NiFe₂O₄/BiFeO₃ heterojunction at room temperature. *J. Magn. Magn. Mater.* **449**, 372–377 (2018).
176. Del Bianco, L., Spizzo, F., Tamisari, M. & Laureti, S. Dependence of exchange bias on the field-cooled remanent magnetic state in Ni/NiO nanogranular samples. *Solid State Commun.* **151**, 351–353 (2011).
177. Paccard, D., Schlenker, C., Massenet, O., Montmory, R. & Yelon, A. A New Property of Ferromagnetic-Antiferromagnetic Coupling. *Phys. Status Solidi B* **16**, 301–311 (1966).
178. Wang, L. G., Zhu, C. M., Bao, D. L. G. C., Tian, Z. M. & Yuan, S. L. Giant exchange bias behavior and training effect in spin-glass-like NiCr₂O₄/NiO ceramics. *J. Mater. Sci.* **50**, 5904–5911 (2015).
179. Binek, C. Training of the exchange-bias effect: A simple analytic approach. *Phys. Rev. B* **70**, 014421 (2004).
180. Dai, B., Cai, J. W. & Lai, W. Y. Structural and magnetic properties of NiFe/NiMn bilayers with different seed and cap layers. *J. Magn. Magn. Mater.* **257**, 190–194 (2003).
181. Ambrose, T. & Chien, C. L. Magnetic properties of exchange coupled NiFe/CoO/NiFe trilayers. *Appl. Phys. Lett.* **65**, 1967–1969 (1994).
182. Carey, M. J. & Berkowitz, A. E. Exchange anisotropy in coupled films of Ni₈₁Fe₁₉ with NiO and Co_xNi_{1-x}O. *Appl. Phys. Lett.* **60**, 3060–3062 (1992).
183. Yamane, H. & Kobayashi, M. Differential type giant magnetoresistive memory using spin-valve film with a NiO pinning layer. *J. Appl. Phys.* **83**, 4862–4868 (1998).
184. Lin, T. *et al.* Improved exchange coupling between ferromagnetic Ni-Fe and antiferromagnetic Ni-Mn-based films. *Appl. Phys. Lett.* **65**, 1183–1185 (1994).
185. Mao, S., Amin, N. & Murdock, E. Temperature dependence of giant magnetoresistance properties of NiMn pinned spin valves. *J. Appl. Phys.* **83**, 6807–6809 (1998).
186. Nozières, J. P. *et al.* Blocking temperature distribution and long-term stability of spin-valve structures with Mn-based antiferromagnets. *J. Appl. Phys.* **87**, 3920–3925 (2000).
187. Akbulut, A., Akbulut, S. & Yildiz, F. Origin of spontaneous exchange bias in Co/NiMn bilayer structure. *J. Magn. Magn. Mater.* **417**, 230–236 (2016).

188. Kasper, J. S. & Kouvel, J. S. The antiferromagnetic structure of NiMn. *J. Phys. Chem. Solids* **11**, 231–238 (1959).
189. Toney, M. F., Tsang, C. & Kent Howard, J. Thermal annealing study of exchange-biased NiFe-FeMn films. *J. Appl. Phys.* **70**, 6227–6229 (1991).
190. Lee, J. H. *et al.* Interdiffusion in antiferromagnetic/ferromagnetic exchange coupled NiFe/IrMn/CoFe multilayer. *J. Appl. Phys.* **91**, 1431–1435 (2002).
191. Lai, C.-H., Wang, Y.-H. & Huang, R. T. Effects of orientation transition on exchange anisotropy of CoNiMn films by biorientation epitaxial Cu/Au/Cu underlayers. *Appl. Phys. Lett.* **85**, 2298–2300 (2004).
192. Groudeva-Zotova, S., Elefant, D., Kaltofen, R., Thomas, J. & Schneider, C. M. NiMn/FeNi exchange biasing systems—magnetic and structural characteristics after short annealing close to the phase transition point of the AFM layer. *J. Magn. Magn. Mater.* **278**, 379–391 (2004).
193. Tieg, C., Kuch, W., Wang, S. G. & Kirschner, J. Growth, structure, and magnetism of single-crystalline $\text{Ni}_x\text{Mn}_{100-x}$ films and $\text{Ni}/\text{Mn}/\text{Co}$ bilayers on Cu(001). *Phys. Rev. B* **74**, 094420 (2006).
194. Ashida, T., Sato, Y., Nozaki, T. & Sahashi, M. Effect of the Pt buffer layer on perpendicular exchange bias based on collinear/non-collinear coupling in a Cr₂O₃/Co₃Pt interface. *J. Appl. Phys.* **113**, 17D711 (2013).
195. Tsai, C. Y., Hsu, J.-H., Saravanan, P. & Lin, K. F. Study on the occurrence of spontaneously established perpendicular exchange bias in Co₄₉Pt₅₁/IrMn bilayers. *J. Appl. Phys.* **115**, 17D726 (2014).
196. Ali, M. *et al.* Exchange bias using a spin glass. *Nat. Mater.* **6**, 70–75 (2007).
197. Yuan, F.-T., Lin, J.-K., Yao, Y. D. & Lee, S.-F. Exchange bias in spin glass (FeAu)/NiFe thin films. *Appl. Phys. Lett.* **96**, 162502 (2010).
198. Malozemoff, A. P. Random-field model of exchange anisotropy at rough ferromagnetic-antiferromagnetic interfaces. *Phys. Rev. B* **35**, 3679–3682 (1987).
199. Malozemoff, A. P. Mechanisms of exchange anisotropy (invited). *J. Appl. Phys.* **63**, 3874–3879 (1988).

200. Mauri, D., Siegmann, H. C., Bagus, P. S. & Kay, E. Simple model for thin ferromagnetic films exchange coupled to an antiferromagnetic substrate. *J. Appl. Phys.* **62**, 3047–3049 (1987).
201. Wee, L., Stamps, R. L. & Camley, R. E. Temperature dependence of domain-wall bias and coercivity. *J. Appl. Phys.* **89**, 6913–6915 (2001).
202. Koon, N. C. Calculations of Exchange Bias in Thin Films with Ferromagnetic/Antiferromagnetic Interfaces. *Phys. Rev. Lett.* **78**, 4865–4868 (1997).
203. Schulthess, T. C. & Butler, W. H. Consequences of Spin-Flop Coupling in Exchange Biased Films. *Phys. Rev. Lett.* **81**, 4516–4519 (1998).
204. Ali, S. R. *et al.* Role of interface alloying in the exchange bias of Fe/Cr bilayers. *Phys. Rev. B* **82**, 020402 (2010).
205. Kumar, P. A. *et al.* Superspin glass state and exchange bias in amorphous Fe/Fe-O core/shell nanoparticles. *Mater. Res. Express* **1**, 036103 (2014).
206. Zhu, C., Tian, Z., Wang, L. & Yuan, S. Exchange bias effect in spin glass CoCr₂O₄ nanoparticles. *J. Magn. Magn. Mater.* **393**, 116–120 (2015).
207. Chandra, S. *et al.* Spin dynamics and criteria for onset of exchange bias in superspin glass Fe/ γ -Fe₂O₃ core-shell nanoparticles. *Phys. Rev. B* **86**, 014426 (2012).
208. Ding, J. F. *et al.* Interfacial spin glass state and exchange bias in manganite bilayers with competing magnetic orders. *Phys. Rev. B* **87**, 054428 (2013).
209. Martien, D. Introduction to AC Susceptibility. 4.
210. Tiwari, S. D. & Rajeev, K. P. Signatures of spin-glass freezing in NiO nanoparticles. *Phys. Rev. B* **72**, 104433 (2005).
211. Labarta, A., Iglesias, O., Balcells, Ll. & Badia, F. Magnetic relaxation in small-particle systems: $\ln(t/\tau_0)$ scaling. *Phys. Rev. B* **48**, 10240–10246 (1993).
212. Chandrasekhar, K. D., Das, A. K. & Venimadhav, A. Spin glass behaviour and extrinsic origin of magnetodielectric effect in non-multiferroic La₂NiMnO₆ nanoparticles. *J. Phys. Condens. Matter* **24**, 376003 (2012).

213. Bedanta, S. & Kleemann, W. Supermagnetism. *J. Phys. Appl. Phys.* **42**, 013001 (2008).
214. Slimani, Y., Baykal, A. & Manikandan, A. Effect of Cr³⁺ substitution on AC susceptibility of Ba hexaferrite nanoparticles. *J. Magn. Magn. Mater.* **458**, 204–212 (2018).

List of Figures

Figure 1.1: The antiparallel alignment of spins which is observed for small distance of the atoms.....	6
Figure 1.2: The parallel alignment of spins in which distance of the atoms is large.....	6
Figure 1.3: The direction cosines in spherical polar coordinate.....	8
Figure 1.4: Subdivision into magnetic domains (a) saturated state with a single domain with high demagnetizing energy (b) division into two magnetic domains to reduce demagnetizing energy (c) division into multiple domains to further reduce the demagnetizing energy (d) free poles in the outer surface is eliminated by forming the closure domains.....	13
Figure 1.5: Represents a 180° and 90° domain wall	15
Figure 1.6: Shows the rotation of magnetization in a Bloch wall and Neel wall.....	16
Figure 1.7: The hysteresis loop of a ferromagnetic sample indicating the saturation magnetization (M_S), remanent magnetization (M_r) and coercive field (H_C).....	18
Figure 1.8: The Barkhausen effect in small portion of initial magnetization curve. This figure is taken from the reference 21.....	19
Figure 1.9: The regions of domain wall motion and coherent rotation processes in the initial magnetized curve. This figure is taken from the reference 21.....	20
Figure 1.10: The orientation of saturation magnetization M_S and applied field H wrt easy axis	21
Figure 1.11: Magnetic hysteresis loops of single domain particle with uniaxial anisotropy. This figure is taken from the reference 22	22
Figure 1.12: The hysteresis loops of the ideal and real soft magnets. This figure is taken from the reference 25	23

Figure 1.13: The hysteresis loops of the ideal and real hard magnets. This figure is taken from the reference 25.....23

Figure 1.14: The exchange spring state of soft/hard magnetic phases. This figure is taken from the reference 3.....25

Figure 1.15: (a) The dotted line is the hysteresis loop of Co-CoO particles taken after zero field cooling protocol and the solid line hysteresis loop is measured after cooling down to 77 K in presence of a field of 10 kOe. (b) The plot of torque measured for Co as a function of azimuthal angle at room temperature showing uniaxial anisotropy (c) The torque curve measured at 77 K of Co-CoO particles showing unidirectional anisotropy (d) The torque magnetometer setup. The caption is in accordance with the references. This figure is taken from the reference 2.....26

Figure 1.16: (1) The spin arrangements in a FM/AFM system. Symmetric hysteresis loop like a FM layer is found when the temperature is below T_C but above T_N . (2) The spin configuration of the FM is in positive saturation state. (3) By reversing the magnetic field, the FM layer rotates as a whole in the direction of magnetic field. (4) The spin configuration in the negative field saturation state. (5) The spin configuration during remagnetization where the FM spin rotating with the field direction. By this field cooling method, a shifted hysteresis loop can be found.....28

Figure 1.17: Schematic view of various angles and vectors involved in the Meiklejohn-Bean model. K_{AF} and K_F represent the anisotropy constants of the antiferromagnetic and the ferromagnetic layers. The ferromagnetic magnetization vector M_F makes an angle β wrt the FM anisotropy axis K_F . The external field is applied at an angle θ wrt the cooling field direction. The figure is reproduced from references.....30

Figure 1.18: Schematic view of various angles and vectors involved in the modified Meiklejohn-Bean model. AFM layer is considered to be rigid but a deviation of α is allowed from the initial direction. Sublattice antiferromagnetic layer magnetization is defined as M_{AF} . K_{AF} and K_F are the anisotropies of the antiferromagnetic and ferromagnetic layers. Ferromagnetic magnetization vector M_F is at an angle β wrt the ferromagnetic anisotropy axis K_F . The external field H is applied at an angle θ wrt the cooling field direction.....32

Figure 1.19: Schematic of the domain state model. This figure is taken from the reference 2.....33

Figure 1.20: Phase diagram of a diluted antiferromagnet (DAFF). This figure is taken from the reference 2.....33

Figure 2.1: Schematic of plasma formation region along with ion current density magnitude in conventional, type 1, and type 2 unbalanced magnetron sputtering. This figure is taken from the reference 43.....40

Figure 2.2: Schematic of dc magnetron sputtering system with various components. The light purple colour cone represents the plasma present in the system.....42

Figure 2.3: The image of the UHV multi-deposition system at NISER manufactured by Mantis deposition Ltd. UK.....43

Figure 2.4: Schematic of X-ray diffraction where incident X-ray beam gets diffracted from the atomic planes with constructive interference to give the reflected beam.....45

Figure 2.5: Schematic of the geometry of the Grazing incidence X-ray diffraction (GIXRD) with the detector45

Figure 2.6: The incident beam of wave vector K_i incident on two layers of different refractive indexes from vacuum with incident angle θ which is reflected at the same angle with wave vector K_f . X-ray reflectivity results from the interference of the reflected waves from different interfaces.....47

Figure 2.7: (a) Precession of the magnetic moment with a magnetization vector M towards the effective magnetic field direction due to the presence of damping like torque, (b) the splitting of the energy levels in the presence of magnetic field where the energy difference of the atomic levels at resonance $g\mu_B H_{res}$ is equal to the energy of the microwave power $h\nu$ 50

Figure 2.8: Schematic of CPW-FMR with lock-in amplifier.....52

Figure 2.9: Schematic of the pick-up coils, the sample moves inside it which is inductively coupled to the SQUID via an input transformer placed in the magnetic field generated by superconducting magnet and the theoretical response against the position of the sample in the pick-up coils is also shown. This figure is taken from the reference 65.54

Figure 2.10: The three different geometries of magneto optic Kerr effect (MOKE) are polar, longitudinal and transverse59

Figure 2.11: Schematic of longitudinal Kerr effect. This figure is taken from the reference 71.....61

Figure 2.12: Shows various components of Kerr microscopy. For oblique incidence of light, the iris is deviated from its optical axis... This figure is taken from the reference 71.....62

Figure 2.13: Schematic of neutron refraction from a surface at angle θ_1 and with refractive index n_1 different than incident beam medium with refractive index n_0 and angle θ_065

Figure 2.14: Schematic of the scattering geometry of spin polarized and monochromatic neutron beam. Spin flippers are used before and after the neutron reflection to find spin flip (SF) and non-spin flip (NSF) scattering.....66

Figure 3.1.1: Schematic illustration of (a) perpendicular (\perp) (b) parallel (\parallel) deposition configuration71

Figure 3.1.2: (a)-(d) Show the hysteresis loops measured by longitudinal MOKE based magnetometry for the samples S1 to S4 along $\phi=0^\circ$ (EA), 30° , 60° and 90° (HA), respectively.....73

Figure 3.1.3: $\mu_0 H_C$ vs ϕ plot for all the samples74

Figure 3.1.4: The magnetic domain images recorded by Kerr microscopy along $\phi = 0^\circ$, 30° , 60° and 90° for the samples S1 to S4. The scale bar shown in figure (a) is valid for all the domain images. The insets shown in images (f), (n), (o), and (p) are the zoomed-in view of the square marked areas.....74

Figure 3.1.5: Shows the plot of FMR spectra vs applied magnetic field for all the samples. The open symbols are the experimental data taken at 13 GHz frequency and solid lines generated from the fitting of the experimental data with Lorentzian shape function.....76

Figure 3.1.6: Shows the plot of H_{res} vs frequency (a) and ΔH vs frequency (b) for all the samples.....77

Figure 3.1.7: Anisotropy field (H_K) vs anisotropy energy (K_U) plot for the samples...79

Figure 3.2.1: (a)-(d) Show the magnetic hysteresis loops of samples S1*, S1, S2* and S2, respectively measured using LMOKE based magnetometry at room temperature along $\phi=0^\circ$ (wine curve), 30° (green curve), 60° (red curve) and 90° (dark yellow curve).....82

Figure 3.2.2 : (a)-(d) Magnetic hysteresis loops of samples S10-S13 measured using LMOKE based magnetometry at room temperature along $\phi=0^\circ$ (wine curve), 30° (green curve), 60° (red curve) and 90° (dark yellow curve)83

Figure 3.2.3: Shows the magnetic domain images along $\phi=0^\circ$, 30° , 60° and 90° measured using LMOKE based microscopy at room temperature for samples S10-S13, respectively84

Figure 3.2.4 :(a)-(d) $\mu_0 H_C$ vs ϕ plot for the samples S10-S13.....85

Figure 3.2.5: Represents the plot of (a) ΔH vs frequency (f) (b) H_{res} vs frequency (f) for all the samples86

Figure 4.1 : (a)-(d) The hysteresis loops measured using LMOKE at room temperature along $\phi = 0^\circ$ (red curve), 30° (green curve), 60° (blue curve) and 90° (wine curve) for the samples 1-4, respectively.....92

Figure 4.2 : (a)-(d) The hysteresis loops measured using LMOKE at room temperature along $\phi = 0^\circ$ (red curve), 30° (green curve), 60° (blue curve) and 90° (wine curve) for the samples 5-8, respectively.....93

Figure 4.3: Magnetic domain images of samples 1-8 recorded using LMOKE based microscopy along $\phi = 0^\circ$, 30° , 60° and 90° , respectively. Domain images of sample 2 is recorded using 50X objective whereas 20 X objective is used for all other samples.....95

Figure 4.4: (a) Resonance field (H_{res}) vs f_{FMR} and (b) linewidth (ΔH) vs f_{FMR} plots for all the samples98

Figure 5.1 : (a)-(d) The XRR experimental data (red open circles) along with the fitted GenX simulated patterns (blue solid line) of samples A-D105

Figure 5.2: (a)-(d) Hysteresis loops measured by LMOKE at room temperature along $\phi = 0^\circ, 30^\circ, 60^\circ,$ and 90° for samples A-D106

Figure 5.3: Magnetic domain images of sample A-D along $\phi=0^\circ$ (EA), $30^\circ, 60^\circ$ and 90° (HA) recorded in LMOKE based microscopy at room temperature.....108

Figure 5.4: A schematic of the directions of magnetization M , applied field H and EA w.r.t the sample plane which are used for FMR angle dependent study108

Figure 5.5: (a)-(c) The plot of resonance magnetic field (H_{res}) vs in-plane angle ϕ for samples A, C and D, respectively. Solid symbols are the experimental data while solid lines are the best fit using equation (5.2)109

Figure 5.6: (a) H_{res} , (b) ΔH versus f_{FMR} plot for the samples A, C and D.....110

Figure 5.7: Schematic of all the interfaces and thin film layers in (a) sample C and (b) sample D.....112

Figure 5.8: Polarized neutron reflectivity (PNR) data for sample C at room temperature with saturation magnetic field of -50 mT (a) and -4 mT (b) are applied along easy axis. The open circles are the experimental data points and the solid lines are fitted data for the non-spin flip (NSF) reflectivities R^{++} (red colour), R^- (blue colour), respectively.113

Figure 5.9: Polarized neutron reflectivity (PNR) data for sample D at room temperature measured at saturation magnetic field of -50 mT (a) and -1.2 mT of magnetic field near to coercivity (b) along easy axis. The open circles are the experimental data points and the solid lines are fitted data for the non-spin flip (NSF) reflectivities R^{++} (red colour), R^{-} (blue colour), respectively.....114

Figure 6.1: (a)-(c) Show the GIXRD patterns of the bilayers A1, A2, and A3, respectively.....119

Figure 6.2: (a) H_{EB} vs T and (b) H_C vs T plots of the samples A1-A3.....120

Figure 6.3: Plots of (a) H_{EB} vs H_{FC} and (b) H_C vs H_{FC} for the samples A1-A3.120

Figure 6.4: The variation of H_{EB} with t_{AFM} at different cooling fields for all the samples121

Figure 6.5: (a)-(c) Linear fits of the $\mu_0 H_{EB}$ vs $n^{-1/2}$ data of the samples A1-A3.....121

Figure 6.6 : (a)-(c) Show the 1st, 2nd, and 10th subsequent hysteresis loops of the samples A1-A3, respectively. (d)-(f) the plot of $\mu_0 H_{EB}$ vs n for the samples A1-A3. The red color open circles are the experimental data points, the olive colored segment line is the fitted data using eq. 6.3 and dark yellow colored triangular data points are generated by eq. 6.2.....123

Figure 7.1: Zero field cooled (ZFC)-field cooled (FC) magnetization (M) vs temperature (T) curves of the samples (a) A5 (b) A10 and (c) A15.....128

Figure 7.2: The plots of (a) H_{EB} (b) H_C vs temperature (T) for all the samples.....129

Figure 7.3: Cooling field dependence of (a) H_{EB} (b) H_C for all the samples.....130

Figure 7.4: The linear fits of H_{EB} vs $n^{-1/2}$ experimental data using eq. (7.1) for samples (a) A5 (b) A10, and (c) A15.131

Figure 7.5: 1st, 2nd, 6th subsequent hysteresis loops of samples (a) A5 (b) A10 and (c) A15. (d)-(f): show the plot of H_{EB} vs n of the samples A5, A10 and A15, respectively. The open red circles are the experimental data points, blue triangular data points are generated from eq. 7.2 and black solid line is the fitted data using eq. 7.3.....132

Figure 7.6: The real χ' (a) and imaginary χ'' (b) component of ac susceptibility vs temperature (T) plots at different frequencies of sample A5.....134

Figure 7.7: The real χ' (a) and imaginary χ'' (b) component of ac susceptibility vs temperature (T) plots at different frequencies of sample A10.....135

Figure 7.8: The real χ' (a) and imaginary χ'' (b) component of ac susceptibility vs temperature (T) plots at different frequencies of sample A15.....135

Figure 7.9: (a)-(c) The red open circles are the experimental data points and blue solid line is the fitted data using Néel-Arrhenius (N-A) law of the samples A5, A10 and A15, respectively.....136

Figure 7.10: (a)-(c) The plots of T_f vs $\ln \tau$ of the samples A5, A10 and A15, respectively. The red open circles are the experimental data points and blue solid line is the fitted data using V-F law.....136

List of Tables

Table 3.1.1: The sample nomenclatures, structures, deposition configurations, substrate rotation speed, H_C along easy axis (EA) and hard axis (HA).....	72
Table 3.1.2: Extracted parameters α , ΔH_0 , $4\pi M_{eff}$, H_K , and g-factor evaluated by fitting data of H_{res} vs frequency and ΔH vs frequency using equation (3.1.1) and (3.1.2) for all the samples.....	76
Table 3.2.1: Sample nomenclature, structure, H_C along EA, H_C along HA and H_K in mT for all the samples.....	81
Table 3.2.2: The values of the parameters α , $\mu_0\Delta H_0$, $\mu_04\pi M_{eff}$, μ_0H_{Keff} in mT, g-factor, M_S in emu/cc, K_U in J/m ³ and K_S in erg/cm ² for all the samples.....	86
Table 4.1: Sample nomenclature, structure, and Ar gas flow amount in sccm. The numbers in the brackets are in nm.....	91
Table 4.2: Sample name, H_C along EA, H_K in mT, saturation magnetization (M_S) in emu/cc and anisotropy energy (K_U) in J/m ³ for all the samples.....	97
Table 4.3: Details of extracted values of α , ΔH_0 , g-factor, $4\pi M_{eff}$, H_{Keff} and K_S obtained by fitting eq. (4.1), (4.2) and (4.3).....	99
Table 5.1: Details of sample structure.....	105
Table 5.2: Shows the structural parameters such as thickness, roughness obtained from X-ray reflectivity (XRR) data fitting using Genx software. Here, D and σ denote the thickness and roughness of thin film layers.	106
Table 5.3. H_C along EA and HA and H_K for all the samples.....	107
Table 5.4. List of values of the magnetic parameters g, $4\pi M_{eff}$, H_{Keff} , α , ΔH_0 obtained from the fitting of equations 5.3 and 5.4, perpendicular surface anisotropy constant K_S found from eq. 5.7, and saturation magnetization M_S for all the samples.....	111

Table 6.1: Sample nomenclature and configuration of all the samples.....	118
Table 6.2: Parameters obtained from the fitting of the training effect data using equation 6.1, 6.2, and 6.3.....	124
Table 7.1: Details of sample nomenclature and configuration.....	127
Table 7.2: The fitting parameters obtained using eq. 7.1, 7.2 and 7.3.....	133
Table 7.3: Fitting parameters obtained using equations 7.4, and 7.5 of all the samples.....	137